DAMAGE MECHANISMS AND INDENTER SIZE EFFECTS IN CROSS PLIED CARBON-CARBON COMPOSITES

THESIS

Andrew Kenny
Captain, USAF

AFIT/GAE/ENY/89D-18

DEPARTMENT OF THE AIR FORCE
AIR UNIVERSITY
AIR FORCE INSTITUTE OF TECHNOLOGY

Wright-Patterson Air Force Base, Ohio

AFIT/GAE/ENY/89D-18

DAMAGE MECHANISMS AND INDENTER SIZE EFFECTS IN CROSS PLIED CARBON-CARBON COMPOSITES

THESIS

Andrew Kenny
Captain, USAF

AFIT/GAE/ENY/89D-18

AFIT/GAE/ENY/89D-18

DAMAGE MECHANISMS AND INDENTER SIZE EFFECTS IN CROSS PLIED CARBON-CARBON COMPOSITES

THESIS

Presented to the Faculty of the School of Engineering

of the Air Force Institute of Technology

Air University

In Partial Fulfillment of the

Requirements for the Degree of

Master of Science in Aeronautical Engineering

Andrew Kenny, B.S.

Captain, USAF

December 1989

Preface

Carbon-carbon is a composite material which has captured the interest of engineers because of its ability to support structural loads and maintain its stiffness at temperatures above the melting point of super alloys. In addition, it has a comparatively low specific weight and its fiber orientations can be aligned for maximum structural performance required by a specific application to further improve its weight advantage. This makes it a particularly attractive material for aircraft and missile components such as rocket nozzles, jet engines, and leading edge skins for hypersonic vehicles.

Such components must reliably incorporate joints, fasteners, and other points of contact. In carbon-carbon, failure is likely to initiate at these points. In order to develop safe reliable designs, the modes of failure which can occur must be carefully documented. Practical methods for reducing contact damage would be useful. It is hoped that this work may contribute to efforts in this area.

This research was primarily an experimental effort using the AFIT and WRDC laboratory facilities. Mr. Anderson's expertise and helpfulness with the laboratory machines, instruments, and electronics was greatly appreciated.

Major Hager from the Structural Materials Branch, of the Wright Research Development Center (WRDC), helped with his insight on the failure mechanisms, and by providing necessary assistance in his organization. Mr Fecke in the WRDC Turbine Engine Development Branch provided the material and motivation for this study. Mrs. Kanko typed the draft and final version and worked as hard as anybody.

List of Figures

Figure

Figure

Figure

Figure

List of Tables

Table of Contents

Abstract

Microscopic damage initiation and progression were examined in woven two dimensional ACC-4 carbon-carbon. Initiation was found to occur as shear cracks in the matrix between the fibers, and at higher load levels in the matrix between the tows. The three point bend test was utilized as a tool for initiating damage because it imparted several different types of stress to different areas of the beam, allowing several failure modes to be characterized with a single specimen.

A finite element model was used to compute the stresses in different regions of the three point bend specimen. The stresses thus computed could be related to the failure modes in different areas of the beam. The validity of the finite element method for modeling the local stress field caused by the indenter and support pins and the overall global stress field of the beam in bending was confirmed by comparing the linear displacements computed by the model and the linear displacements measured experimentally at the midpoint. The stresses computed for each element were input through Dendis' post processor which computed the Tsai-Wu quadratic

failure criteria. Comparison of this analytical result with experimental result confirmed that this method could predict the area and load level at which damage would initiate, regardless of the microscopic form of that damage.

Different damage mechanisms were observed when the parameters of beam thickness, beam span to depth ratio, ply layup, and load pin size and rigidity were varied. To document the effect of the parameters on the damage, several experimental methods were used. The most useful of these were optical, SEM, and X-Ray photography. By systematically observing the damage at increasing load levels, and by cross-sectioning the samples, a complete characterization of the failure modes was determined.

DAMAGE MECHANISMS AND INDENTER SIZE EFFECTS IN CROSS PLIED CARBON-CARBON COMPOSITES

I. INTRODUCTION

Goals

The goal of this thesis was to characterize the damage mechanisms in woven 2-D carbon-carbon. The specific failure modes caused by specific types of stress were sought. Particular interest was in determining the failure modes near points of contact. In practical engineering designs of carbon-carbon components, similar damage could be expected at fastener holes or joints.

Analytically it was desired to be able to predict the initiation levels and areas of damage. Dendis had shown (8) that for carbon-carbon the Tsai-Wu quadratic failure criterion could be used for this purpose.

The objective of this thesis was to perform a systematic study using the three point bend test and determine the load levels of specific failure mode initiation. A variety of test parameters were used to study their effects. The geometry and ply layup of the three point bend specimens were varied, as was the size and

rigidity of the contact indenter. Several techniques for observing the microscopic failure mechanisms were investigated. The initiation load levels and areas of the three point bend beam where damage was found was compared to the Tsai-Wu quadratic failure theory coupled with a finite element model of the beam to confirm the work of Dendis (8). This analysis was performed on beams of two thicknesses and correlated with all the failure modes documented.

Background and Purpose of the Parameter Study

In this research, the three point bend test served the useful purpose of creating damage for study in carbon-carbon. In different areas of the three point beam, different types of stress were present so that a single specimen could be used to study the effect of several stresses on several failure modes; a necessity since the amount of material for this project was limited.

The three point bend and four point bend tests are widely used to measure the interlaminar shear strength of composites (1:538, 2:55, 5:54). Fixtures for the tests are simple to design and the specimens are easy and inexpensive to make. The three point bend apparatus, standardized by ASTM D 2344 (2:59), is shown in Figure 1.

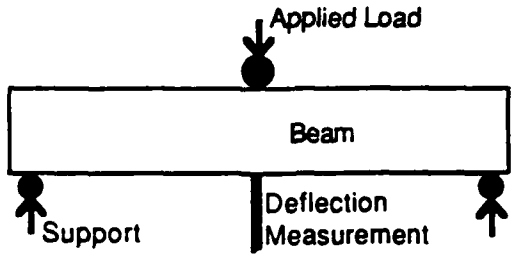

Figure 1. Three Point Bend Test Schematic (2:58)

However, as the title of ASTM D 2344 suggests, "Apparent Interlaminar Shear Strength of Parallel Fiber Composites..." (2:55), the measured shear strength is only the apparent strength, not the true shear strength. Generally, several damage mechanisms contribute to failure of the beam, including compressive failure below the indenter or all along the top surface, tensile at the bottom surface, and shear at the neutral axis. This was an advantage for this project though, since the purpose was to study all these failure modes and how they were affected by different three point bend parameters.

These parameters were chosen based upon previously published works on the distribution of stress in composite beams, and on previous experimentation in damage initiation in carbon-carbon. The four parameters were beam span to depth ratio, thickness, layup, and indenter characteristics.

The parameter which had the greatest effect on the overall stress distribution in the beam was the ratio of span to depth. By varying it, the relative importance of flexural stress at the top and bottom of the beam versus the shear stress at the neutral axis could be controlled. The rest of the parameters were tested on both four to one and fifteen to one span to depth ratio beams.

The second beam parameter was laminate thickness. Beams were cut from both twenty and thirty ply laminates with the span to depth ratios scaled in both cases to remain at four to one and fifteen to one. Increasing the thickness of the beams made them stiffer, which slightly raised the effect of flexural stress in the plies nearest the top and bottom surfaces. It also raised the maximum load that the beam could support so that the effect of a higher contact load could be seen.

Examining the damage mechanisms in cross plies allowed the effect of an in plane shear component to be observed. And in these plies, all the fibers supported an equal share of the load, not just the fibers aligned with the beam axis as in the [0/90] laminates.

To study the contact problem, several indenters were used. The standard quarter inch steel indenter, specified by ASTM 2344, was used as a baseline. An indenter with ten times that diameter was tested to find if the damage would

be increased by longer contact length (7:68) or simply spread out and reduced. To ensure that the effect of a uniformly distributed load would be studied, a short and long beam were tested with a thick rubber pad placed between the standard steel indenter and carbon-carbon surface.

Material

Carbon-carbon composites combine the lightweight strength advantage of graphite fibers with the high temperature resistance of a carbon matrix. Its strength properties are not degraded by temperatures as high as 3000° C (4:11). Its strength actually increases by a few percent at very high temperatures, as shown in Table 1.

Table 1. Type CC137E Carbon-Carbon Properties at Room and High Temperature.

PROPERTY	70° F	2000° F
Tensile Strength	310 Mpa	370 Mpa
Compressive Strength	200 Mpa	240 Mpa
Interlaminar Shear	17 Mpa	26 Mpa

In addition, carbon-carbon composites are resistant to creep deformation at temperatures as high as 2310° C (12:1). Its major weakness is its shear strength, which is only about one twelfth its compression strength. The material has found applications in rocket nozzles, re-entry heat shields, disk brake rotors, and piston heads.

Figure 2 (8:7) shows a layer of graphite cloth, several of which can be laid up to make a laminate. The process to manufacture a panel begins by soaking a stack of plies in a high char liquid such as coal tar pitch or phenolic. To bind and harden the matrix the entire assembly is heated to 900° C in an inert atmosphere. During this process, volatile gases boil out of the liquid, and some of these gases are trapped in the laminate as the liquid solidifies, to form unwanted voids in the laminate. To reduce the volume of voids, the resin soaking and pyrolizing process is repeated up to six times, and each time more of the voids are filled by carbonized matrix (12:2-4).

Figure 3 shows a polished section of a cured carbon-carbon laminate, showing ninety degree or fill tows consisting of many circular fibers. A zero degree or warp tow is also visible with its fibers appearing as long strands. The large dark regions are empty voids.

Hitco manufactured the ACC-4 carbon-carbon laminates from which the beams from this study were cut. The laminates were made from twenty and thirty ply stacks of eight harness satin weave plies of the type shown in Figure 2. The number of fibers in the zero and ninety degree direction, known as the warp and fill directions, were equal so that strength and stiffness properties were considered identical for the ply in both these directions. These

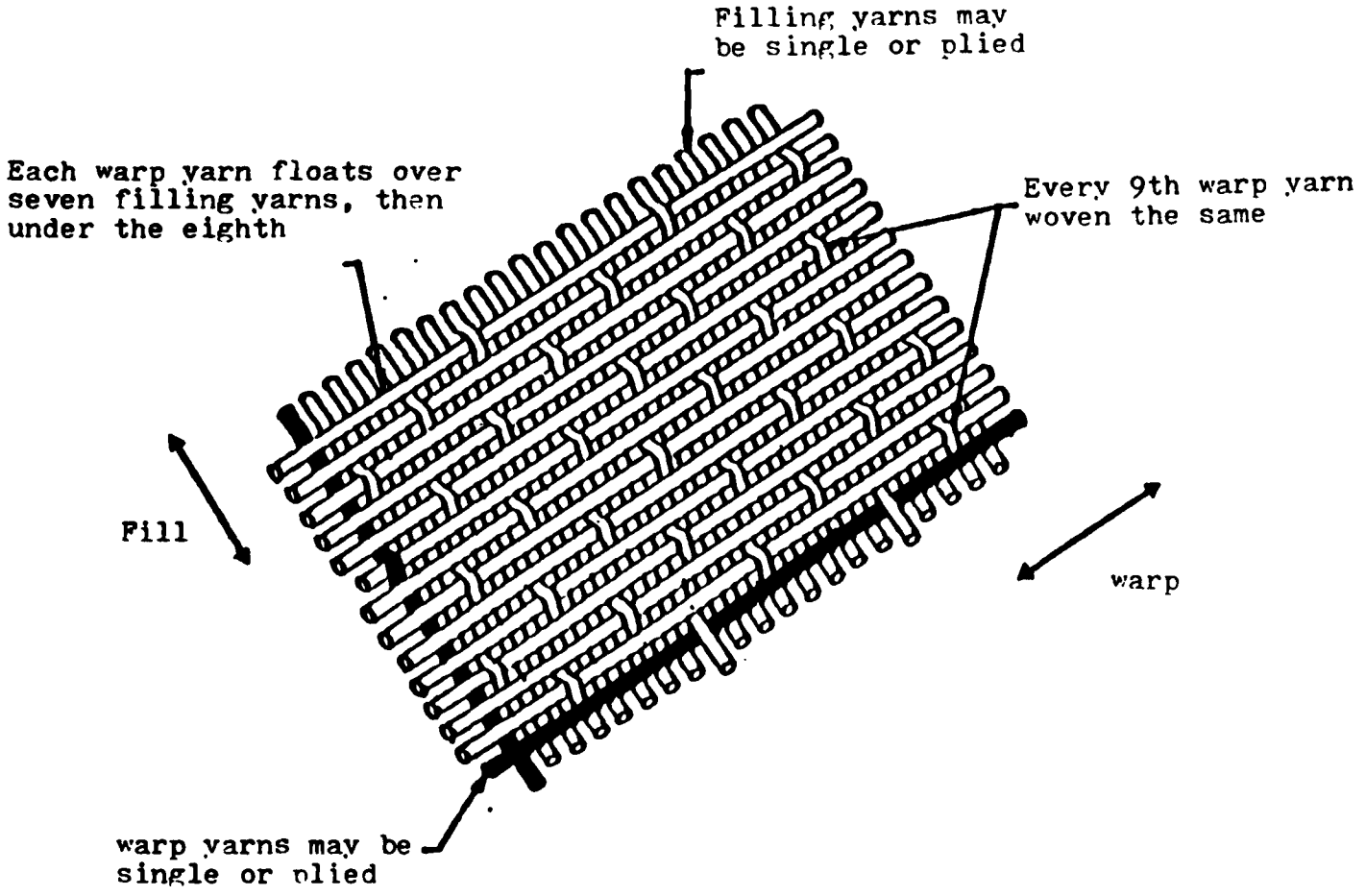

Figure 2. The 8-Harness Satin Weave Cloth (8:27)

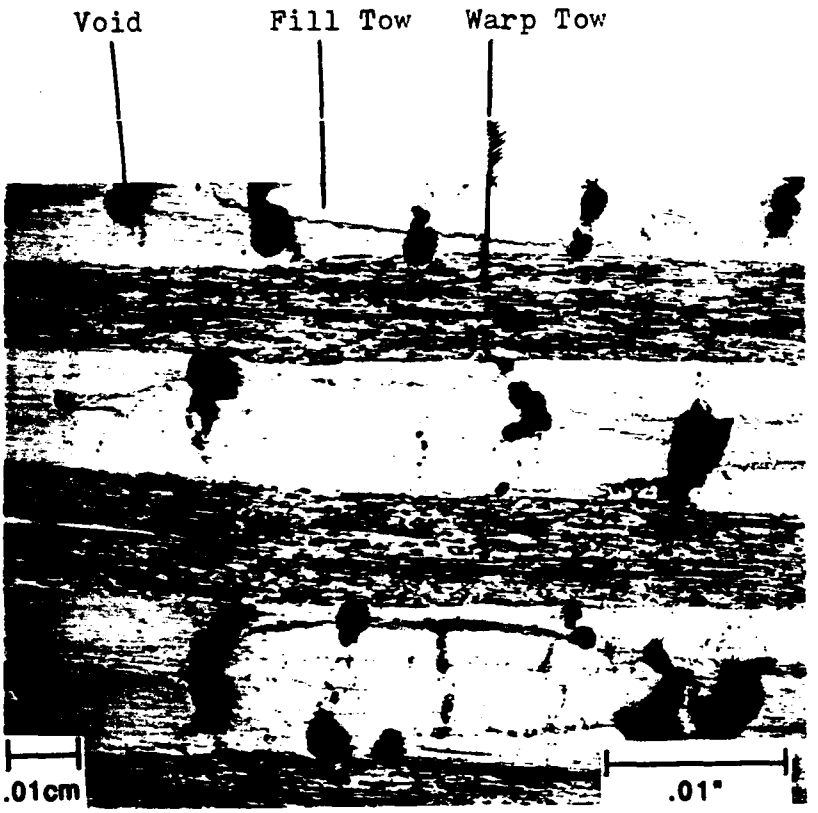

Figure 3. Cured Carbon-Carbon Laminate Microstructure 100x.

properties are given in Table 2 and Table 3. Previous finite element and failure criteria computations by Dendis (8:70) with the values in these tables produced mid-point displacements within five percent of experimental values.

Table 2. Directional Strengths of the ACC-4 Eight Harness Satin Weave Ply, MPa (psi)

Tensile		Compressive		Shear
X_T	Z_T	X_C	Z_C	S
330.9	3.79	179.3	172.4	6.89
(48,000)	(550)	(26,000)	(25,000)	(1,000)

Table 3. Directional Stiffness of the ACC-4 Eight Harness Satin Weave Ply Gpa (msi)

E_x	E_z	G_{xy}	G_{xz}	V_{xy}	V_{xz}
110.3	3.10	2.41	1.38	.05	.2
(16)	(.45)	(.35)	(.20)		

II. THEORETICAL DEVELOPMENT

Summary of Current Knowledge

In this research the three point bend test was used because it could impart several types of stress to a single specimen, and these stresses could then be related to the types of microscopic failure morphologies which appeared. Actually determining the stresses present in a given area of the beam was not nearly as straight forward as such a simple test might suggest.

Knowledge of stresses in the beam was critical in order that it be related to the damage morphologies which initiated and progressed with higher load levels. Thus the theoretical development begins with a description of the overall global stresses which would be present in an isotropic beam in bending. Then how the orthotropic properties of a composite may affect the global field are considered. Finally, the localized stress field in the region of the indenter is examined since it had a profound affect on the damage which first initiated. By using a finite element model it was possible to analyze the stresses in the beam with all these complications.

According to the classical Bernoulli-Euler beam theory, the horizontal shear stress in a beam in bending varies parabolically through the thickness being a maximum along the midplane. This maximum stress is given by the formula:

$$T(max) = \frac{\emptyset.75\ P}{bh} \qquad (1)$$

where P is the vertical load applied at failure, b is the width of the beam and h is the depth.

The flexural stress of the same beam in pure bending would, according to classical beam theory, vary linearly from top to bottom. At the top would be the highest compressive stress, at the midplane there would be no flexural stress, and at the bottom would be the highest tensile stress. Tests such as ASTM 2344, which is meant to measure a composite's apparent shear strength, utilize a span to depth ratio short enough that the material's maximum shear stress would be reached at the neutral axis before the material's maximum flexure strength is reached at the top and bottom surface. However, the experimental failure loads measured in highly orthotropic composites tested in three point bend do not accurately resemble the shear strength in Eq (1).

In order to cause the specimen to fail in shear, a short span to depth ratio is required, but one of the

assumptions of the classical Bernoulli-Euler beam theory is that the span to depth ratio is large. This is one reason that the short span to depth ratio of four to one specified by ASTM D 2344 introduces error into Eq (1).

Because the shear strength of carbon-carbon composite material is twenty times less than the flexure strength, it is not necessary to use a very short span to depth ratio to get shear dominated failures in three point bend specimens. Using the same elementary approach as for Eq (1), the maximum flexure stress is given by the formula:

$$S\ (max) = 1.5\ \frac{PL}{bh^2} \qquad (2)$$

where P is the vertical load applied at failure, b is the width of the beam, h is the depth, and L is the length between the supports. Comparing Eq (1) and Eq (2) with the compressive strength, 193 Mpa (28000 psi), and the shear strength, 3.8 Mpa (550 psi), for ACC-4 carbon-carbon a span to depth ratio as high as fourteen to one would allow the beam to fail in shear if these equations were reliable.

Paradoxically, the long span to depth ratio now introduces an error of its own because it allows so much deflection that the rotational terms, ignored in the formation of Eq (1) and Eq (2), are no longer insignificant. In addition, both Eq (1) and Eq (2) for both long and short

beams assume both an isotropic tensile and shear modulus, which is not the case for a composite like carbon-carbon. Pagano showed this introduced an error between measured and predicted displacement of an orthotropic graphite epoxy beam with span to depth ratio of ten to one as high as one hundred percent (10:330-343).

The above review indicates that calculations of stress in various regions of the beam from classical theory would be too inaccurate to relate any microstructural damage found to them. However, from the overall global stress field it is evident that beams with a shorter span to depth ratio would have a wider range above and below the neutral axis where cracks initiated due predominantly to shear stress.

In a practical three point bend test, the localized indenter stress field dominates the stresses in the region near the contact point. In a shorter beam, the localized field may be the dominant field in the specimen. For example, Whitney (14:298) tested orthotrophic graphite epoxy beams with a four to one span to depth ratio and found that the failures, though shear dominated, occurred in the upper quarter of the beam near the indenter. To categorize the failure morphology, the relative proportions of the different stresses present would have to be known accurately. A reliable and accepted method of finding these stresses is finite elements.

The local stress fields introduced by the indenter and load pins are much more significant in orthotropic composite beams than in standard metal beams (3:207-208). The indenter and pins cause severe shear local stress fields, and as Berg (3:211) showed, the actual shear stress near the indenter is more than twice as great as that predicted by the classical Bernoulli-Euler theory. Figure 4, which Berg developed from his finite element analysis, shows that the whole shear stress distribution is skewed by the indenter in the upper quarter of the beam. In addition, the indenter causes both vertical compressive stresses and horizontal and longitudinal compressive local stress fields. These stresses can result in localized failures such as matrix crushing and fiber buckling. The compressive stress may suppress material failure by shear.

This complex stress state means that test specimens which appear to fail by shear in the upper quarter of the specimen (that is, when a long horizontal interlaminar crack appears) are actually not failing just by shear. Using scanning electron microscopy, Whitney (14:300) found hackles on the supposed interlaminar shear fracture surface of a four point bend specimen. These are caused by a combination of tensile and shear stress, indicating that the failure was not entirely due to shear.

The hackles found on the fracture surface indicate that the four point bend specimen is also dominated by the indenter stress field. However, since only half the load is exerted by each roller, the local stress field caused by each roller is more moderate than in the three point test. Rosensaft and Marom compared interlaminar shear strengths of a unidirectional graphite epoxy laminate and found that the shear stress measured by four point bending was about seven percent higher than the shear strength measured by three point bending (11:14). They also found that the failure transition from shear to tensile/compressive stress did not occur at a sharp span to depth ratio as would have been predicted from comparing the maximum shear strength and maximum compressive strength with the classical shear and compressive stress equations, Eq (1) and Eq (2).

The major conclusion of this review of the three and four point bend test is that the global stress field is highly dependent on the orthotropic stiffness properties, and that the localized stress field caused by the indenter dominates the stresses near the contact point. Classical beam theory is not adequate for obtaining accurate stresses anywhere in the beam, but it helps give an estimate of the effect of varying the beam span to depth ratio on the global stress field. Shorter beams would have a larger area

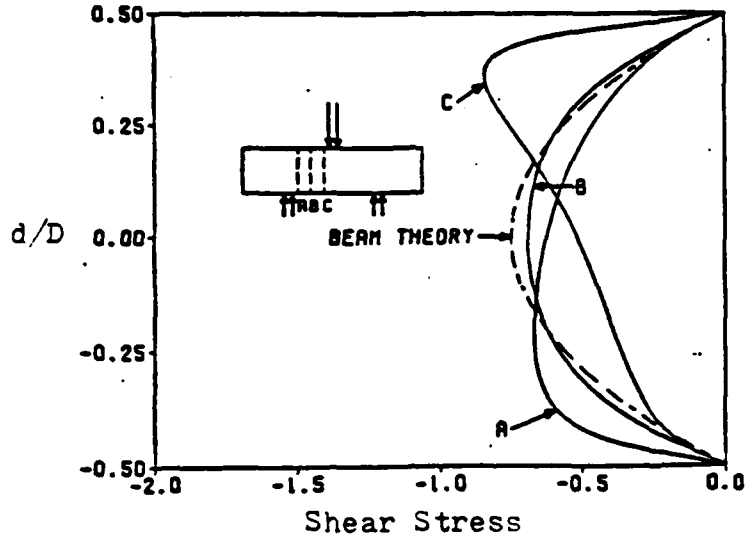

Figure 4. The Actual Shear Stress Concentration Caused by the Indenter, Compared to the Stress Distribution Predicted by Classical Beam Theory. (3:211)

above and below the neutral axis dominated by shear, whereas flexural stress at the top and bottom of longer beams would have more significance.

To categorize the microscopic damage mechanisms as they occur with increased load in the three point bend test, the relative proportions of the stresses present must be accurately known. Berg (3), Dendis (8) and DuPont (9) showed that the finite element method worked well for this purpose, accounting both for the global stress field and the localized stress field of the indenter and support pins in orthotropic graphite epoxy beams.

Finite Element Method Analysis

To obtain the stresses needed for damage characterization in carbon-carbon, a similar finite element analysis was used. An input data deck preprocessor developed by Dendis (8:30) for NASTRAN was modified for this purpose for the geometry of beams used in this research. Each element in the input data deck was matched with a property card which included the thickness of the element, which in this case was the thickness of the beam, and a pointer to a material card which contained the stiffness matrix. The elements were two dimensional allowing only a three by three stiffness matrix as shown by Eq (3).

$$[Q] = \begin{bmatrix} Q_{11} & Q_{13} & Q_{15} \\ Q_{13} & Q_{33} & Q_{35} \\ Q_{15} & Q_{35} & Q_{55} \end{bmatrix} \tag{3}$$

Since all the plies were warp aligned with the long axis of the beam, the stiffness matrix was orthotropic. In Eq (3) this meant that Q_{15} and Q_{35} were zero.

With the preceeding stiffness matrix and each element a single ply in depth, NASTRAN could then compute the stress at each element and the displacements at the nodes for an orthotropic carbon-carbon beam loaded in three point bend. The accuracy of the method could be tested by comparing the displacement computed to the displacement measured experimentally by an LVDT at the center of the bottom of the beam.

From the stresses computed at the centroid of each element, a failure criteria based on distortional energy given by the following equation

$$F_i S_i + F_{ij} S_i S_j - 1 = \emptyset \quad i = 1...6 \qquad (4)$$

known as the Tsai-Wu criteria, could be computed for each element (15:220). In Eq (4) the coefficients F_i and F_{ij} are computed from the material strengths of the laminate, and the S_i terms are the element stresses.

Dendis (8:93) developed a FORTRAN program which would compute the failure criteria number based upon Eq (4) and generate an output file of the centroid of each element and the failure criteria which could then be plotted as failure contours. Regions of failure, that is where the failure criteria exceeded 0.0, could be compared to microscopic observation of the polished face of the beam. The agreement between the NASTRAN analysis and what was experimentally observed was within five percent for the [0/90] beams which he tested.

III. EXPERIMENTATION

Objective

With a good finite element analysis method established for determining the stresses in the beam, an experimental method was needed for examining the damage they caused. A method for determining the initial load at which damage appeared, be it matrix cracking or fiber breakage, was needed. Then, how the damage progressed after it initiated had to be observable. And finally, the failure modes due to different types of stress were of great interest if they had the most significant effect on the final integrity of the material before it completely broke.

A fast non-destructive method which could be used to map the damage as it initiated and progressed would have been very useful. Several x-ray and penetrant methods were investigated, but the microscopic size of the cracks which initiated and the omnipresence of voids in the matrix prevented those methods from being effective. This left microscopic examination of the surface as the only good way to track damage as it occurred with increasing load level.

Approach

The parameters of the three point bend test were varied to affect the different types of failure modes. Specifically, the beam span to depth ratio, thickness, and ply layup were varied as parameters, and the size and rigidity of the load indenter was varied so the failure modes which occurred at a point of contact could be studied in detail. Table 4 shows the number of specimens tested under each combination of parameters utilized. L/d denotes span to depth ratio.

Table 4. Number of Specimens Tested According to Each Combination of Parameters

	Test Parameters			Number
Span/Depth	Thickness	Layup	Indenter	Tested
4	20 Ply	[0/90]	Standard	2
4	30 Ply	[0/90]	Standard	3
4	30 Ply	[0/90]	Large	2
4	30 Ply	[0/90]	Cushioned	2
15	30 Ply	[0/90]	Standard	2
15	30 Ply	[0/90]	Large	2
15	30 Ply	[0/90]	Cushioned	2
4	20 Ply	[0/45]	Standard	2
4	30 Ply	[0/45]	Standard	1
15	20 Ply	[0/45]	Standard	1
15	30 Ply	[0/45]	Standard	1

Specimen Preparation

The panels used for this study were made from ACC-4 2-D carbon-carbon manufactured by Hitco by the multiple compaction method described earlier. Two of the parameters of this damage characterization study were thickness and ply layup and so specimen beams were cut from four different panels. Two of the panels had a [Ø/9Ø]s layup, but one was twenty plies thick and one was thirty. The other two had a [Ø/45/Ø/-45]s layup and the same twenty and thirty ply thicknesses. All the panels were made from eight harness satin weave plies, none of them had any type of oxidation protection coating.

The panels were cut into the beam specimens with a submerged diamond blade. Patterns designed to obtain the maximum number of beam specimens possible from each panel were used since the material was scarce. These are shown in Figures 5 and 6. The warp direction served as the zero degree axis. Beams with the two span to depth ratios, four to one and fifteen to one, were cut from each panel. Hereafter, the beams with four to one span to depth ratio will be referred to as "short", and the beams with fifteen to one span to depth ratio as "long".

To observe the microscopic damage on these beams, their edges had to be given a very fine polish. Preliminary work showed the apparent microstructure to be exceptionally

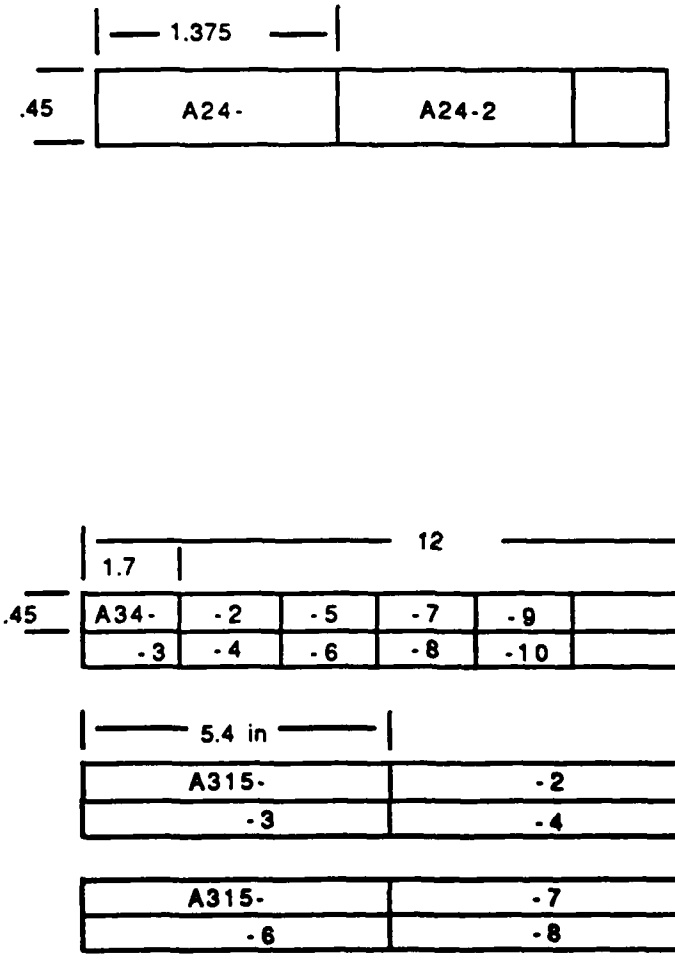

Figure 5. Sample Beams Cut From the Twenty Ply [0/90] Laminate, Top and Thirty Ply Laminate, Bottom.

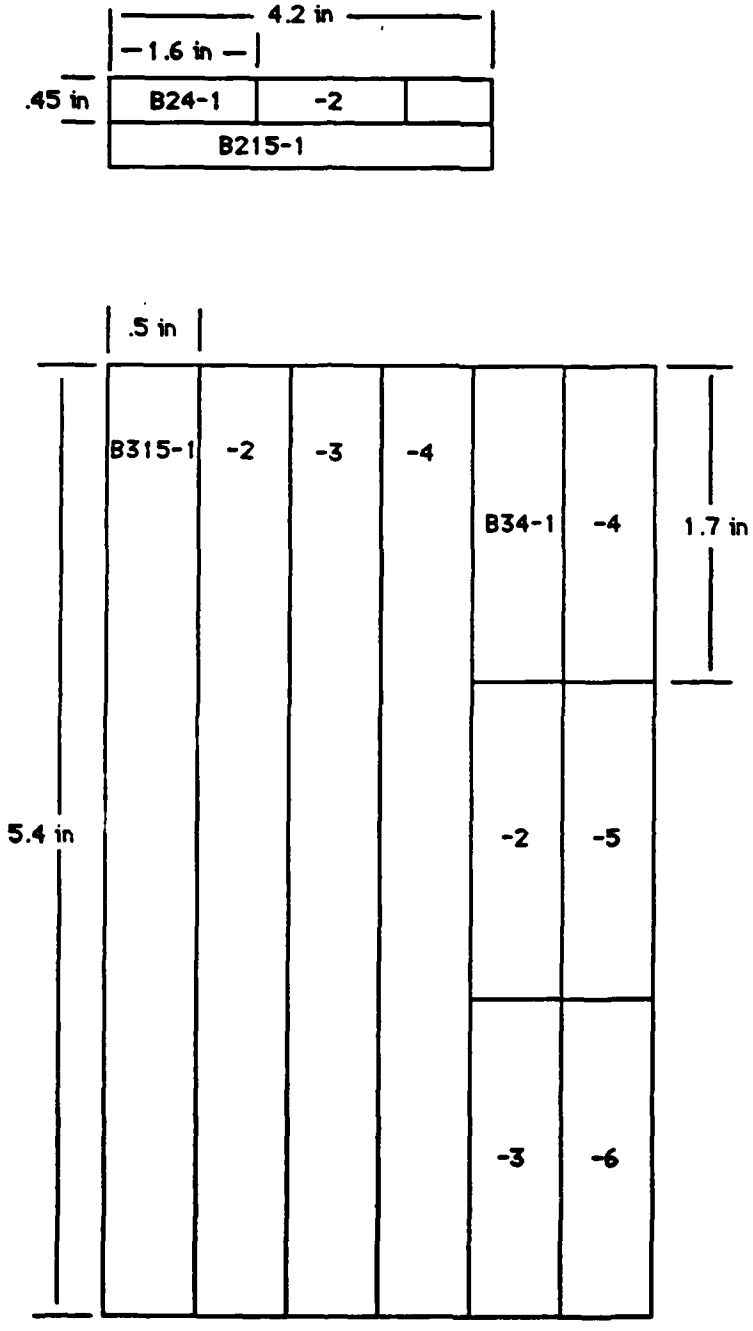

Figure 6. Sample Beams Cut From the Twenty Ply [Ø/45]s Laminate, Top and Thirty Ply Laminate, Bottom.

sensitive to the polishing method used. Figure 7 shows the carbon-carbon microstructure after polishing with 4000 grit sandpaper. The microstructure appears to contain fewer voids and fissures than the same material polished with a diamond slurry, Figure 8. The diamond abrasive appears to crush and pull out some of the matrix between the fibers, making the carbon-carbon look more porous than it may actually be, while the sanding method appears to smear the matrix into some of the voids. For this project, the sanding method was used because it was difficult to observe microcracks which initiated between the fibers of the diamond polished samples since the matrix was often crushed out of these spaces by the gritty diamonds. The sanding method had the additional advantage that it was used by most other researchers, making the results of this work more easily comparable. The dimensions of the samples referred to in the appendix were found by measuring the sample after the final polish but before it was loaded.

Test Equipment

The mechanical apparatus used to apply a three point bending load to the beam specimen is shown schematically in Figure 9. The loading ram applied the force to the beam through the steel semicircle and load pin as shown. Figure 9 shows the configuration used to load the beam with the

Figure 7. Carbon-Carbon Microstructure After Polishing with 4000 Grit Sandpaper, 50x.

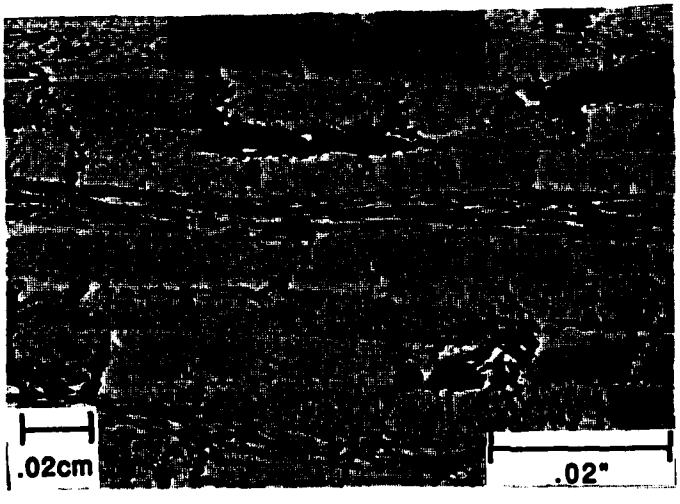

Figure 8. Carbon-Carbon Microstructure After Polishing with Diamond Slurry, 50x.

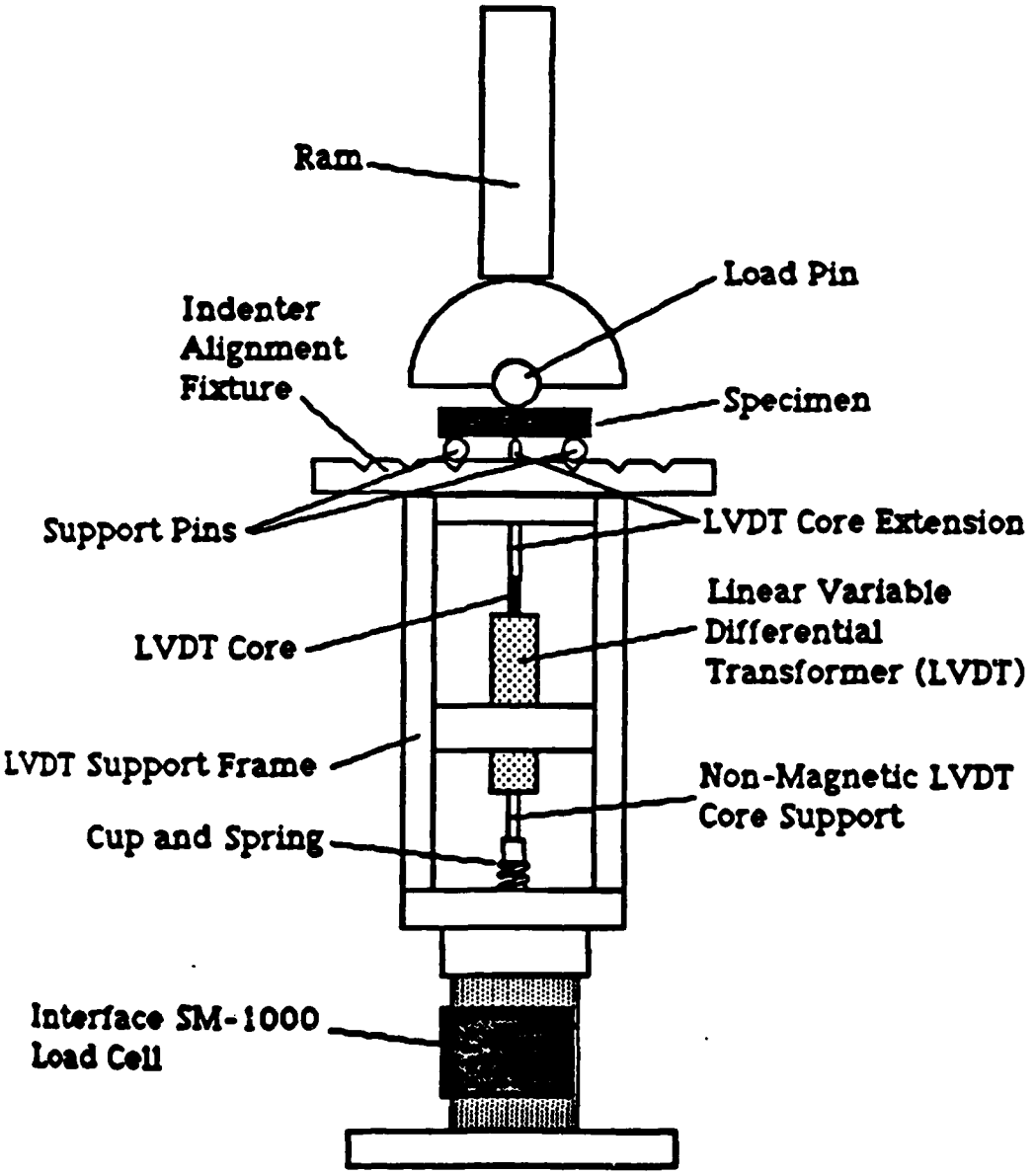

Figure 9. Three Point Bend Experiment Apparatus (8:47)

quarter inch diameter steel load pin. To load the beam with the two and one-half inch diameter indenter, the positions of the load pin and semicircle were interchanged. The diameter of the semicircle was ten times the diameter of the quarter inch load pin. In this thesis, the load pin is often referred to as the indenter. The beam was supported by eighth-inch diameter steel pins which fitted into the slots spaced so that both the short and long beams could be tested on the same plate.

The LVDT support frame was approximately ten inches long, made from aluminum, and bolted to the support plate. The assembly below the beam specimen settled about four thousandths of an inch as the first thirty pound load was applied. This amounted to less than ten percent of the measured displacement of the short carbon-carbon beams and less than two percent of the maximum displacement of the long beam. It contributed to the repeatability of the displacement measurements as determined from the load displacement curves, being limited to plus or minus six percent.

The displacement was actually measured at the midpoint of the bottom of the beam from the deflection of the LVDT core extension shown in Figure 9. The advantage of this method was that displacement was measured directly beneath the load point, and the fixture settling could be determined by calibration.

The electronic device used to convert the displacement into a measurable signal was a standard linear variable differential transformer or LVDT. The circuit schematic is shown in Figure 10. The conditioner sent the incoming frequency and voltage to the primary coils at the transformer, and movement of the LVDT core changed the permeability of the transformer and thus, the output voltage from the secondary coils. This output voltage was directly proportional to the displacement of the core. This was calibrated as shown in Figure 11. The relation of Figure 11 was determined by least squares to be:

$$X\ (mm) = (3.023\ (millivolts) - 13.44)/10,000 \qquad (17)$$

where X is the displacement. The accuracy of the LVDT was within 0.051 mm (0.002 inches).

A one thousand pound capacity load cell was used to measure the weight which the ram applied to the beam. As shown in Figure 10, the Endevco power supply input a voltage to the load cell, which was simply a group of three strain gages, and received the resulting output voltage which was proportional to the applied load. The load cell output voltage was routed to a Hewlett Packard 3466A digital voltmeter so that it could be monitored during testing. A special circuit designed by Mr. Jay Anderson of the AFIT Aeronautical Engineering Laboratory automatically would stop

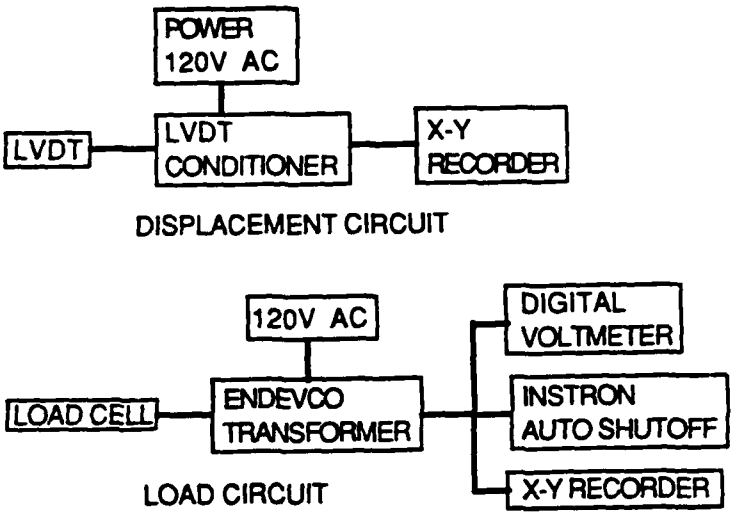

Figure 10. Curcuit Schematics for Measuring Load and Displacement

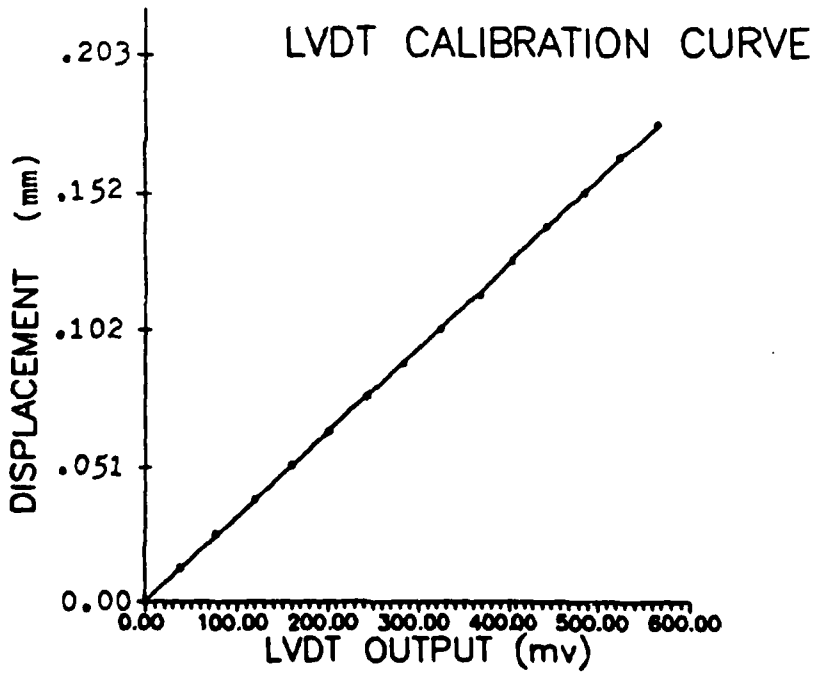

Figure 11. LVDT Calibration Line.

the ram before the compressive limit of the load cell was reached. The accuracy and repeatability of the load measurements were within plus or minus one percent. The calibrated slope of load versus voltage output was linear according to the relation

$$P\ (N) = 2.8013\ (\text{millivolts}) \qquad (18)$$

where P is the load exerted through the indenter.

Test Procedure

The test procedure was designed entirely with the purpose of categorizing damage in carbon-carbon under varying stresses. This was accomplished with optical microscopy by examining the polished face of the beam. The damage generated was recorded at planned load increments applied through three point bend. The first increment was as low as five percent of the theoretical failure load, then generally the load was increased in steps of ten percent. Between each step, the beam was removed from the test fixture and examined along the edge, and microscopic damage was sketched and photographed. This method allowed observation of failure initiation and progression as the stress increased.

Several procedural details needed to be followed in order to obtain consistent results. The strain gages in the load cell needed to be warmed up for three hours and then

the fixture needed to be loaded several times above the load expected for the current test to minimize the fixture settling during the test. Once those steps were completed, the carbon-carbon sample was placed in the fixture, the load cell output voltage electronically zeroed, and the x-y plotter pen adjusted to the desired origin of the load displacement curve.

The optical photographs taken between each load increment were made with simple light, except a green filter was used to narrow the band of wavelengths for sharper focused pictures. The photographs taken were Polaroid Type 55 film which simultaneously produced an instant print and negative. The photographs in this report were reproduced from these negatives, except for a few which are reproduced half-tones. The resolution of damage which could be found by this method was about .ØØ1 mm (.Ø3 mils) or, in terms of the microstructure, about five fiber diameters.

A few samples of both the short four to one and longer fifteen to one span to depth ratio were cut into halves after they were broken, for examination of the cross sections. Since most of the analytical models of the three point bend test method have only been two dimensional, cross sections through damaged areas were used to give insight on how the three dimensional stresses, acting in concert, affect failure. The shapes and orientations of the damage

in the form of matrix cracking, interply cracking, and fiber/matrix separation along the beam edge and through cross sections told much about the type and severity of the stresses. Figure 12 shows a cracked carbon-carbon laminate soaked with epoxy which hardened in the voids and cracks before it was sanded with 4000 grit paper. This epoxy impregnation method was necessary with the cross sections to prevent polishing from smearing over cracks that were already present.

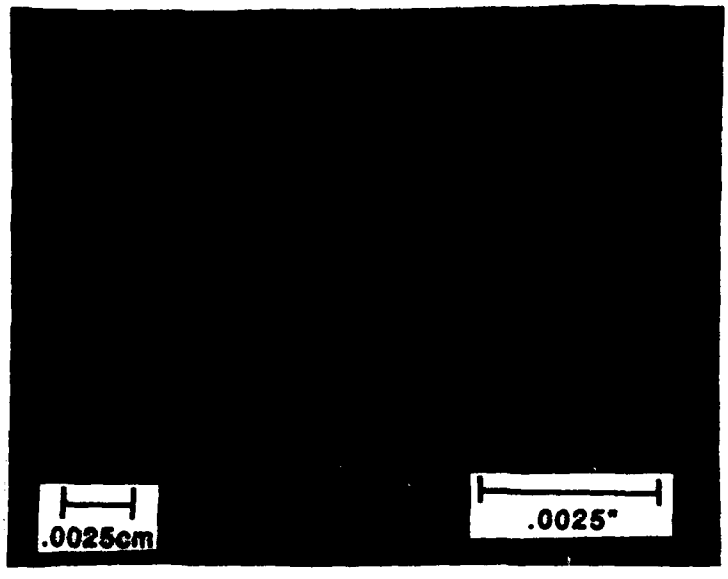

Figure 12. Cracked Carbon-Carbon Laminate Soaked with Epoxy to Fill Voids Before Sanding Polished Surface with 4000 Grit Paper, 400x.

For examining the actual fracture surface, scanning electron microscopy had to be used since the depth of field of optical microscopy was insufficient for this purpose. To prevent the nonconductive carbon-carbon from becoming polarized under the electron beam, the fracture surface was coated with seven microns of conductive gold-palladium by sputtering in an inert atmosphere. It was found that SEM fracture surface morphologies caused by particular stresses such as matrix shear, interlaminar shear, matrix tensile overstress, fiber overstress and so on were not well documented. Scanning electron micrographs taken at the fracture surfaces at cracks found in various regions of the beam therefore had to be primarily compared to each other to determine if the factors which caused the cracks were essentially different.

One nondestructive inspection technique, radio-opaque x-ray photography, did have limited utility because it made the overall pattern of damage immediately visible in the three point bend beams after they were loaded to failure. In order to determine the same pattern by microscopic observation of the polished beam face, a painstaking hours long process was required, whereas the x-ray technique took minutes.

The radio-opaque x-ray procedure began with brushing a very dense, low viscosity liquid on the polished surface of the beam. The liquid then seeped into any cracks, and unfortunately in this case, the capillary-like voids. When subsequently an x-ray was taken of the beam, the dense liquid in the cracks and voids blocked the x-rays from exposing the film, and a pattern of the internal liquid could be seen.

IV. RESULTS AND DISCUSSION

Eighteen ACC-4 carbon-carbon samples were tested with a three point bend fixture. Several of the test parameters were selectively altered, specifically the central indenter size and hardness, and also the sample's thickness, span to depth ratio, and ply layup orientation.

Results with the Standard Quarter Inch Steel Indenter

Baseline tests to confirm previous results by Dendis (8:53) and to validate the experimental procedures and equipment were performed. Two twenty ply samples with a [Ø/9Ø] woven layup were loaded incrementally. No indication of damage could be seen on the load-displacement curve except that it gradually began to level off above approximately ninety percent of the ultimate load. Figure 51 in the Appendix shows a typical such load displacement curve.

The microscopic damage, as it spread with each additional load increment, is shown in Figure 13. The first load increment was to just four percent of ultimate load, but no damage was observed until after incrementing to thirty-six percent. The initial damage is shown in Figure 14, tow separation can be seen along the first warp and fill

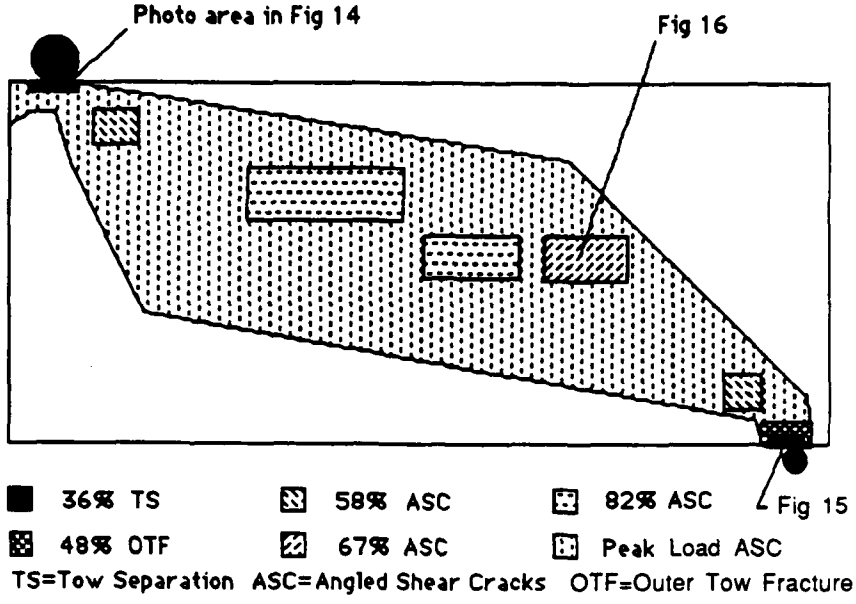

Figure 13. Areas and Load Levels Where Microscopic Damage was First Observed on the Polished Face of the Beam, 20 Ply, L/d=4.

Figure 14. Tow Separation Begins in the Top Fill Layer, 20 Ply, L/d=4, R=36%, 200x.

interface directly below the indenter. At the next load increment, to forty-eight percent ultimate, split fibers were observed directly under a support pin. This is shown in Figure 15 where in addition to the split top tow, there is a horizontal crack separating the top warp tow and the fill tow below it. In the area nearer the neutral axis, a crack was observed in an area of high matrix concentration. Such areas of matrix concentration are common near the borders of voids. Angled shear cracks in the matrix were not observed until after the increment to sixty-seven percent load. Such a crack is shown in Figure 16, which was found at the neutral axis halfway between the indenter and support pin. To summarize the order of occurrence of the failure modes, intertow matrix cracks below the indenter occurred first at the thirty-six percent load level. This was followed by outer ply fiber fracture at forty-eight percent of the ultimate load, and then angled shear cracks at the sixty-seven percent ultimate load level.

Comparison of these damage initiation results to those reported by Dendis (8:53) are in good agreement, see Table 5. Both cases report outer ply fractures at a support pin for load levels within two percent of each other, i.e. forty-six versus forty-eight percent of ultimate load. The angled shear cracks in the matrix at the neutral axis were not observed until sixty-seven percent, even though an

effort was made to find them closer to the fifty-four percent reported by Dendis. However, comparison of the thirty fiber diameter long crack shown in Figure 16, to a similar crack Dendis found at the fifty-four percent level revealed that the one he found was only five fiber diameters long. This suggests that the crack of Figure 16 initiated at a load below sixty-seven percent. Determining the exact load level where such a crack first occurred in the nearly twenty samples tested for this thesis would not have been practical.

Table 5. Baseline Tests, [0/90], 20 Ply, L/d=4, Damage Initiation.

Damage	Dendis	Kenny
Tow Separation at Load Pin	---	36%
Outer Ply Failure at Load Pin	46%	48%
Angled Shear Cracks at Neutral Axis	54%	67%

The NASTRAN finite element analysis and Dendis' (8:30) Tsai-Wu failure criteria subroutine post processor were used to produce a stress contour plot for sixty-seven percent of the ultimate load, shown in Figure 17. This plot for the lowest load level at which angled shear cracks were observed shows the dominance of the local stress field near the indenter. Any failure contour greater than zero indicates a failure site. Examination of the plot reveals there should

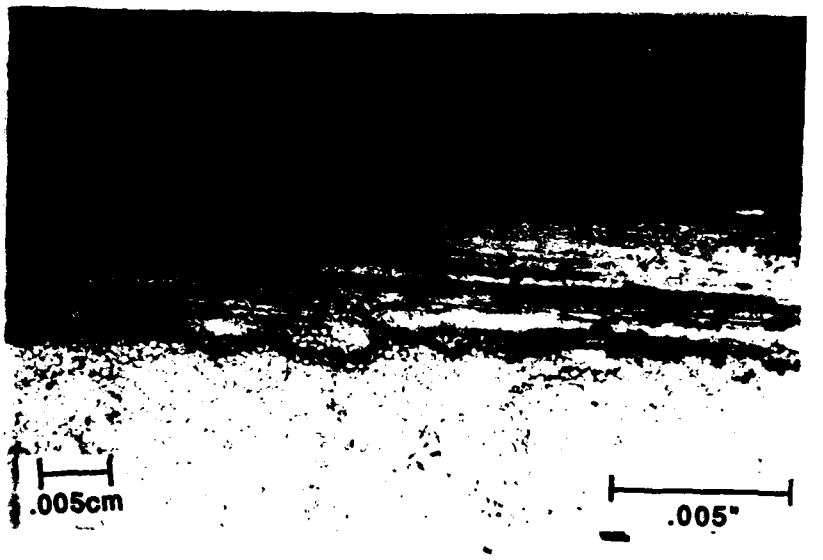

Figure 15. First Observed Fiber Damage Occurred Below a Support Pin, 20 Ply, L/d=4, R=48%, 200x.

Figure 16. Initial Cracks at N.A., Halfway Between Center and Support, 20 Ply, L/d=4, R=67%, 1000x.

be damage along the neutral axis and at the indenter. These results are in reasonable agreement with the observation of microscopic angled shear cracks near the neutral axis which initiated at this level. Although the analysis predicts a larger damage zone than was observed.

The disparity between the damage zone observed and calculated is due to the higher displacement computed from the finite element model than was actually measured experimentally. From all the random voids and matrix agglomerations, it seems natural that the properties between any two panels would vary. If a ten percent higher stiffness matrix had been used in the finite element calculation, then the calculated and measured displacements would have matched. As it was, the displacement predicted at ultimate load, .132 mm (.0052 inches), was thirteen percent above the experimentally measured displacement.

Three thirty ply [0/90] samples were incrementally tested to failure to determine if the increased thickness would increase the severity of the load pin local stress field as was predicted by Whitney (13:180) for graphite epoxy. In addition, the results from testing the thicker samples were used to evaluate the global finite element model. Figure 18 shows the levels at which damage initiated in different areas of the sample due to incremental loading. The pattern and shape of the damage is

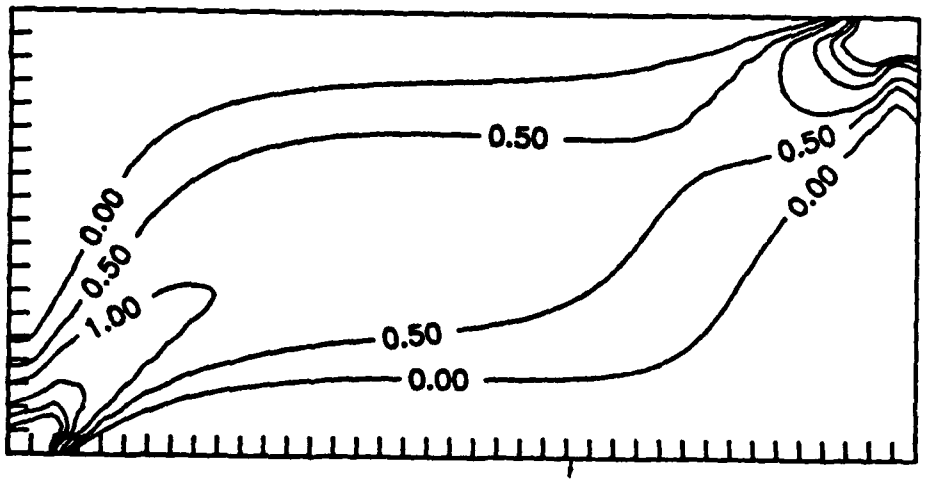

Figure 17. Tsai-Wu Failure Criteria, L/d=4, 20 Ply, R=67%.

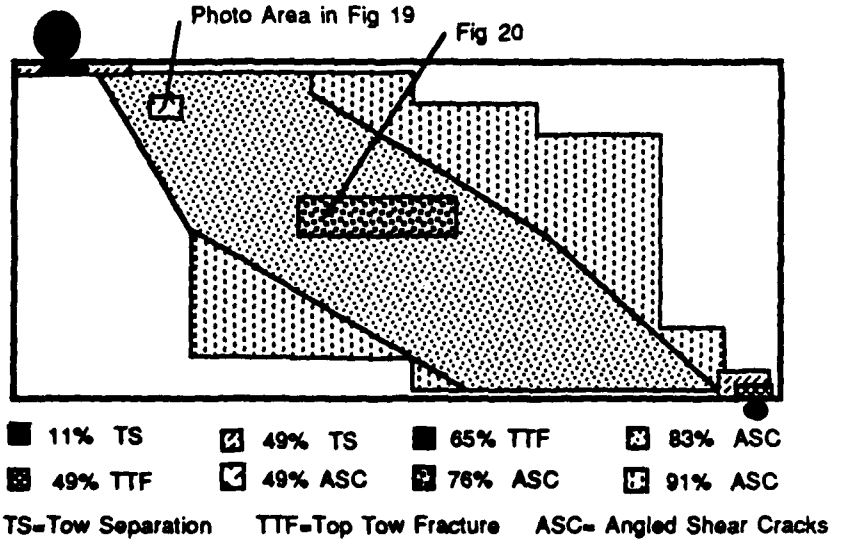

Figure 18. Areas and Load Levels Where Microscopic Damage was First Observed on the Polished Face of the Beam, 30 Ply, L/d=4.

similar to what was observed in the twenty ply samples. Again the first observed damage was matrix cracks at the top of the first fill tow directly below the indenter of the type shown in Figure 14. In the thirty ply samples it occurred as low as eleven percent of the ultimate load, down from thirty-six percent for the twenty ply samples, confirming the expected increased stress near the indenter in the thicker beams. However, the thin boundary of matrix which separated the tows could, as shown earlier, have been slightly distorted on the matrix surface by polishing. This may have lead to minor surface separation between the tow boundaries and matrix which was subsequently enhanced by the compression and relaxation beginning at low load levels. Since polishing was done by hand, this effect may have varied from sample to sample.

Split outer ply fibers were not observed directly under a support pin until forty-nine percent of ultimate. This was within three percent of the load level where the same type of damage was observed previously in the thinner twenty ply beams. Outer ply fracture was not observed beneath the quarter inch diameter indenter until sixty-five percent of the peak load. Also, a single angled shear crack which is shown in Figure 19 was observed, but it was discounted as being an anomaly at this low load level since it may somehow have been related to matrix differences near the void by

which it was situated. No other angled shear cracks were observed until seventy-six percent load. At that load level, several angled shear cracks were observed very close to the neutral axis, which are shown in Figure 20. This was nine percent higher than the load level at which the same type of cracks were observed in twenty ply samples. Table 6 summarizes the different load levels required to produce specific types of damage for the twenty and thirty ply beams.

Table 6. Thickness Comparison [0/90], 20 and 30 Ply, L/d=4

Thickness	Tow Separation at Indenter	Outer Ply Failure at Support Pin	Angled Shear Cracks at N.A.
20 Plies	36%	47%	67%
30 Plies	11%	49%	76%

The same order of failure modes was observed for both thicknesses of the short beam. Tow separation, a matrix cracking mode between the tows of the top ply beneath the indenter, was the first mode. This was followed by outer ply failure beneath the indenter. Finally, angled shear cracks occurred near the neutral axis.

From Table 6 it appears that outer ply failure occurred at the same load level for both thicknesses, and that angled shear cracks occurred at a higher load level in the thicker beam. Actually, the thicker beam sustained about a ten percent lower ultimate load, when normalized by the increase

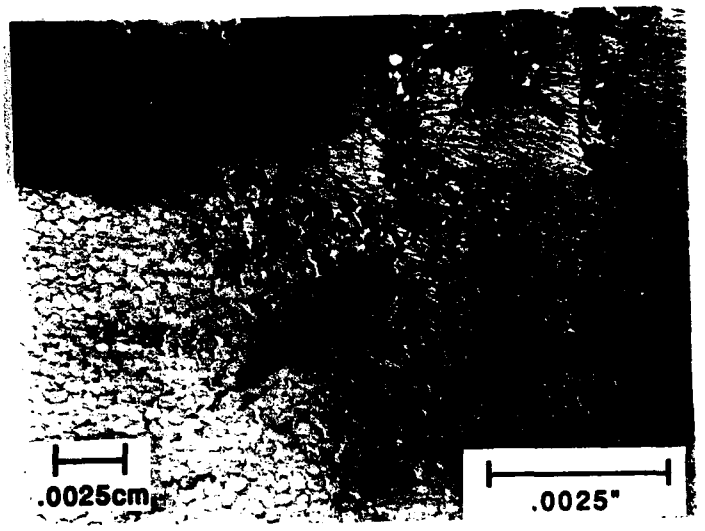

Figure 19. Matrix Crack Associated with Void at N.A., L/d=4, 30 Ply, R=49%, 400x.

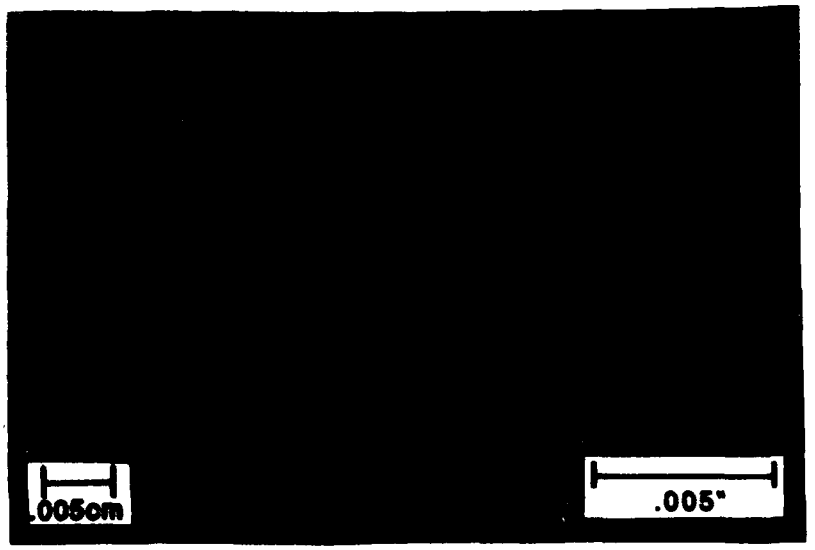

Figure 20. Matrix Shear Cracks at N.A., 30 Ply, L/d=4, R=76%, 200x.

in area, which had the effect of raising the ratio of load at which cracking was observed to the ultimate load of the thicker beams. In this light, outer ply failure occurred at about a seven percent lower load in the thicker beams. This is consistent with the fact that the thicker beams flexed less, which enlarged the contact area of the indenter, thereby increasing the local stress field. By similar calculation, the load at which angled shear cracks were first observed at the neutral axis when normalized to pounds per square inch differed by less than three percent between the thicknesses. This is consistent with the expectation that angled shear cracks would appear at the same global stress level at the neutral axis, and is further supported by tabulated data in the Appendix.

Only matrix cracking was observed, the fibers never broke or showed any damage except directly below the indenter. Generally, cracks were only visible in the matrix dominated fill layers, while in the fiber dominated warp tows there was relatively little matrix, and therefore cracking could not be seen.

Again, a finite element Tsai-Wu failure contour plot was generated, but this time for the thirty ply sample at seventy-six percent of ultimate load. In the plot which is shown in Figure 21, all areas surrounded by a contour greater than zero indicate failure. Very high values of the

contour are indicated at the load pin and indenter. There would be no point in showing the contours any nearer the indenter since the finite element model is calculated from two simple point loads, and the mesh is too coarse. A small region greater than zero is evident near the neutral axis. This corresponds to what was actually observed microscopically at this load level as angled shear cracks. The Tsai-Wu failure criteria at seventy-six percent of ultimate load is shown for the thinner twenty ply beam in Figure 22 for comparison. A wider area of damage is predicted for the thinner beam as was observed experimentally.

When the incremental loading technique was utilized, it was only possible to photograph and record any damage which might occur on the polished beam edge. To find if any different damage mechanisms were occurring inside the beam where they could not have been seen, a short thirty ply beam was cross sectioned after it had been broken. The face of the cross section was then studied microscopically. To prevent the carbon matrix from smearing and filling in any possible cracks during sanding, the cross sectioned face was soaked in epoxy which hardened in the cracks and voids.

Figure 23.a shows how the sample was cross sectioned and Figure 23.b shows a micrograph of the damage typical of the region. This is very similar to the damage observed before on the beam's front surface. Since the positions of

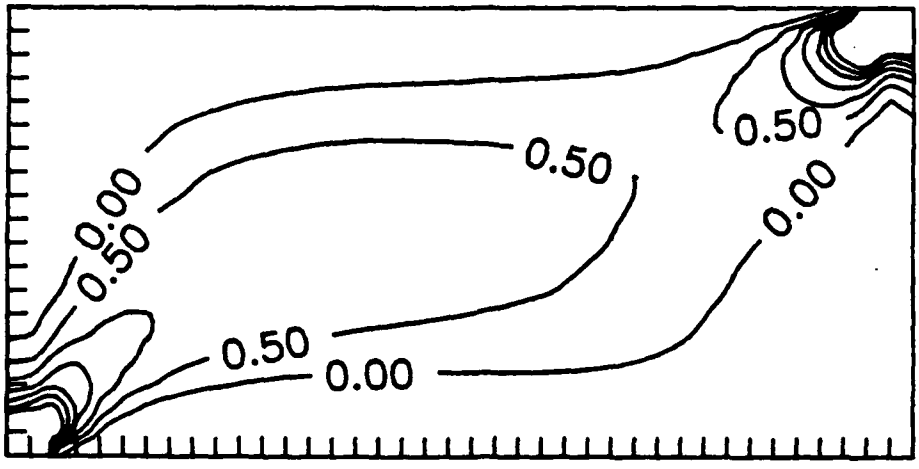

Figure 21. Tsai-Wu Failure Criteria, L/d=4, 30 Ply, R=76%

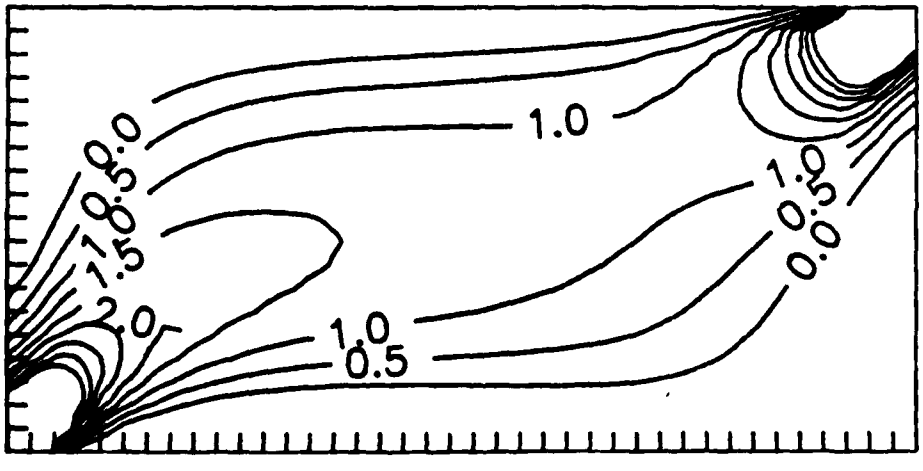

Figure 22. Tsai-Wu Failure Criteria, L/d=4, 20 Ply, R=76%

the fill and warp tows are now reversed, Figure 23 shows that the matrix cracks actually occur in all the tows. The cracks that appeared as angled shear cracks in the fill tows before are seen as horizontal or slightly slanted cracks between the warp tows. Tow separation cracks are also evident because this photograph was taken after the short beam was loaded past peak load. One type of crack that was not seen before on the polished edge is the vertical cracks seen in Figure 23 in the fill tow.

The incremental three point bend tests were performed on samples with a span to depth ratio of fifteen to one. Testing samples with the considerably longer span to depth ratio allowed observation of damage produced outside the range of the influence of local indenter and loading pin stress fields. In a unidirectional graphite/epoxy sample, such a high span to depth ratio results in failure by tensile stresses in the bottom ply due to flexural overload, but the shear stress of carbon-carbon is low enough to still exhibit shear related failures along the neutral axis. Experimentally, the longer span to depth ratio beam provided a means to examine the onset of failure at the neutral axis which was truly caused by shear stress, and analytically, they provided a second test for the global finite element model.

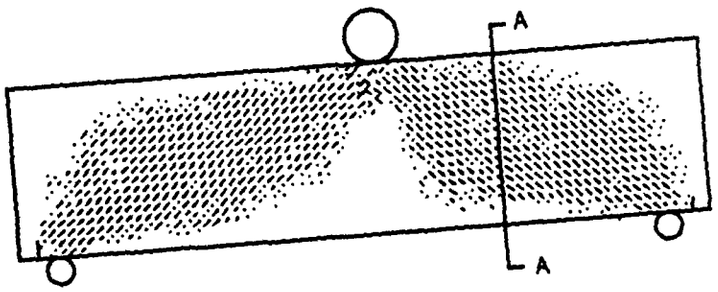

Figure 23.a. Cross Section Location

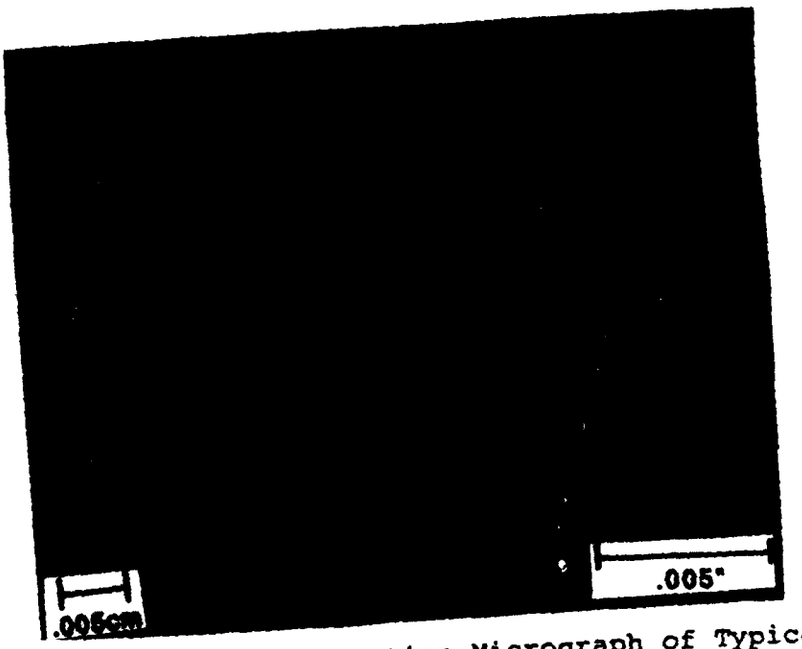

Figure 23.b. Cross-Section Micrograph of Typical Damage Observed, 20 Ply, L/d=4, R=100%, 400x.

Two long twenty ply samples with a [Ø/9Ø] ply layup were tested by Dendis. The approximate ultimate strength of these samples was thirty percent below that of the twenty ply beams with a four to one span to depth ratio. Figure 24 (6:271) shows the progression of damage with each increase in load. The outer ply in direct contact with the support pins was observed to be cracked at the sixty-three percent load level. Angled shear cracking began at seventy-four percent ultimate along the neutral axis. The load displacement curve for these samples, as for all samples with a fifteen to one span to depth ratio, was linear throughout incremental load tests up to ultimate. Then a catastrophic crack formed at the neutral axis from the middle of the sample out to the end, and the load-displacement curve dropped forty-seven percent to a plateau. A typical load displacement curve is shown in Figure 69 of the Appendix. Microscopic examination showed the crack at the neutral axis to be made from a series of angled shear cracks.

Two thirty ply long beams were tested with the standard quarter inch indenter. Both samples were within a percent of the same average ultimate load, which was approximately eleven percent lower than the apparent strength of the twenty ply samples. It is the same trend of increased thickness having lower strength found in the samples with a

four to one span to depth ratio. All samples were incremented to the ultimate load, but only the long beam samples exhibited the catastrophic split.

Figure 25 shows the pattern of internal damage caused by incremental loading in the thirty ply thick beams. The most striking difference between this and the damage pattern observed in the shorter beams of four to one span to depth ratio is that no angled shear cracks were observed near the neutral axis before ultimate load. First damage occurred at the fifty-one percent load level as tow separation in the first fill tows below the indenter. This matrix cracking grew longer horizontally between the topmost warp and fill tows as the load increased. Outer ply fracture began at the sixty-seven percent load level, worsening with increasing load. The outer ply fracture initiation load level differed by only four percent between the twenty and thirty ply long beams.

At eighty-six percent ultimate, a longer wavy horizontal crack in the matrix of a fill tow in the first ply, as shown in Figure 26, was observed 8.89 mm (Ø.35 inches to the right of the steel indenter. It was a significant crack because it was the first one observed in the top ply not directly beneath the indenter. Also, it was longer than any observed before at this load level, and not slanted as the typical shear cracks seen in the matrix at

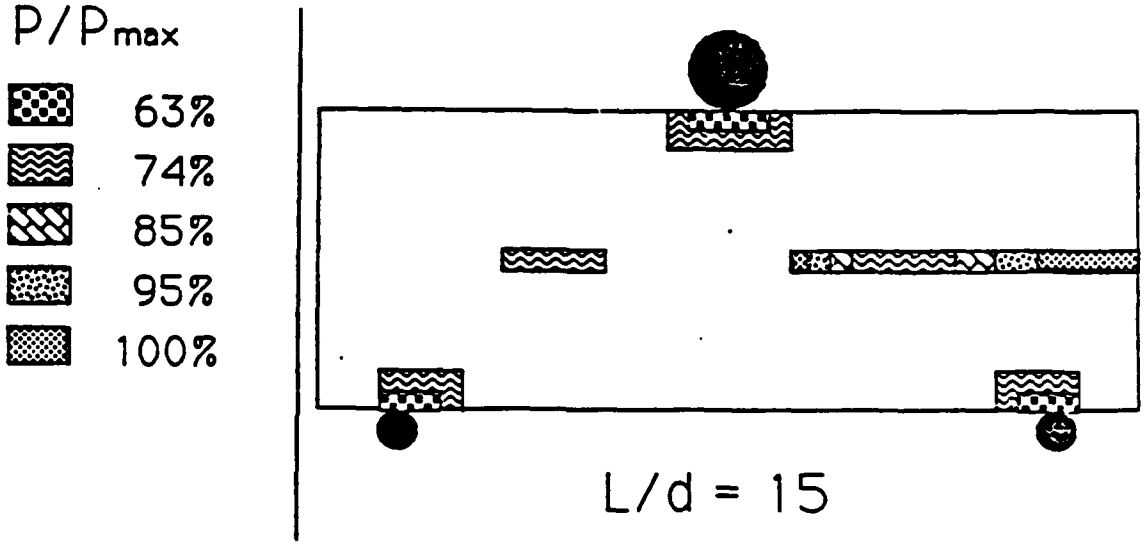

Figure 24. Areas and Load Levels Where Microscopic Damage was First Observed on the Polished Face of the Beam, 20 Ply, L/d=15, [0/90] (6:271).

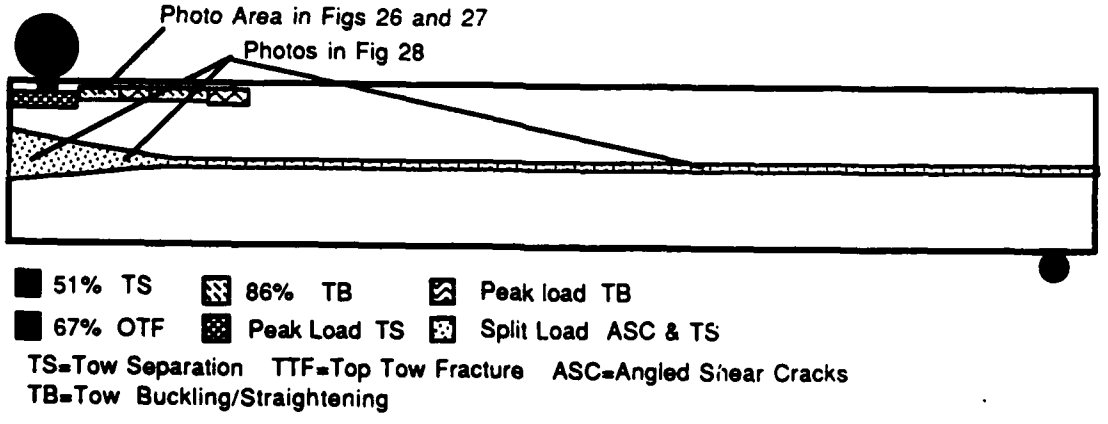

Figure 25. Areas and Load Levels Where Microscopic Damage was First Observed on the Polished Face of the Beam, 30 Ply, L/d=15, [0/90].

the neutral axis of the beams of the four to one beams. This type horizontal matrix crack in the top ply, it shall be shown, was a unique phenomena to all the thirty ply thick beams with the fifteen to one span to depth ratio. At peak load, the long horizontal cracks had grown much larger, as shown in Figure 27.

In the long beam near the top surface the global stress is almost entirely compression. On the microstructural scale, compression is supported mainly by the longitudinal fibers which undulate above and below one another in the weave. This effectively builds an eccentricity into the fibers which begin to buckle near the top surface. In Figures 26 and 27, this manifests itself as cracks where the matrix between the tows is pulled apart in tension. For this reason, this type of crack was never observed directly beneath the indenter where there was a large downward compressive stress field. This microbuckling behavior actually limits the ultimate load supported by the beam.

After the load dropped from its peak, further displacement caused the sample to split. Figure 25 shows the locations from left to right of the three photographs shown in Figure 28 from top to bottom. Figure 28 shows how the long split began as a collection of shear cracks in four or five plies above and below the neutral axis at the middle, but as the split progressed toward the end, it took

Figure 26. Matrix Crack in Top Ply 8.89 mm (Ø.35 Inches) to the Right of the Indenter, 30 Ply, L/d=15, R=86%.

Figure 27. Matrix Crack in Top Ply 5.5 mm (.2 Inches) to Right of the Indenter, 30 Ply, L/d=15, R=100%.

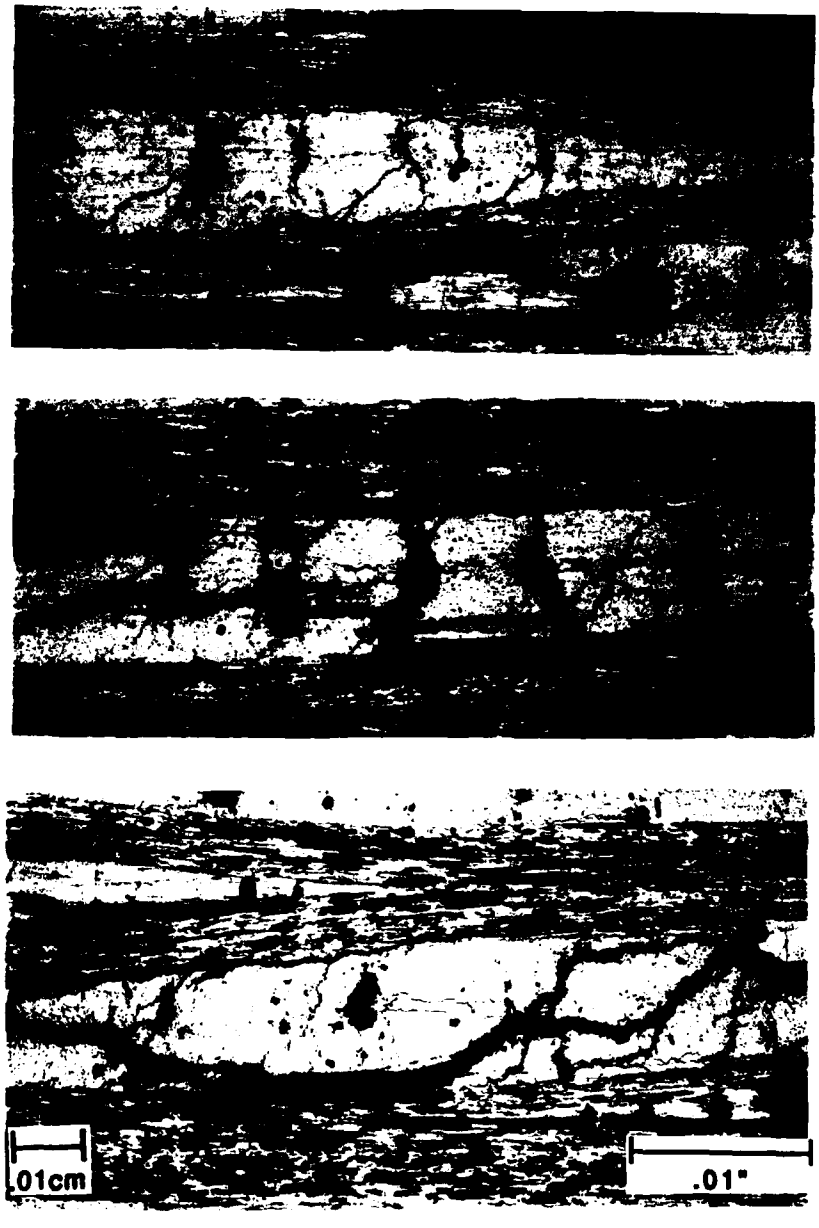

Figure 28. The Main Crack at the Neutral Axis Showing it Becomes More Severe Near the End, 30 Ply, L/d=15, R=100%, Cushioned Indenter, 100x.

on more of the shape of a long, very thick wavy crack in a single ply which frequently ran along a tow boundary. Table 7 compares the different failure mode initiation levels between the twenty and thirty ply long beams.

Table 7. Thickness Comparison [Ø/9Ø], 2Ø and 3Ø Ply, L/d = 15.

Thickness	Outer Ply Failure at Load Pin	Angled Shear Cracks at N.A.	Top Ply Buckling
2Ø Plies	63%	74%	---
3Ø Plies	67%	Peak	86%

The basic mode of failure was different between the twenty and thirty ply long beams. Copp, Dendis, and Mall (6) reported angled shear cracks combined at the neutral axis of the twenty ply beam to cause failure. In the thirty ply beam, the peak load was limited by a buckling of tows at the top, which caused tensile overstress of the matrix between them. A similar mode was observed near the center of the bottom of the beam, as it will be shown in the beams tested with the other indenters. The increase in thickness must have increased the stiffness of the beam enough to raise the effect of the flexural stress.

The areas where damage was predicted by the Tsai-Wu quadratic failure criteria was mostly accurate for the two thicknesses. The failure contour for the twenty ply beam (8:75) is shown in Figure 29. It shows that there should be damage along the neutral axis as was observed. But it also

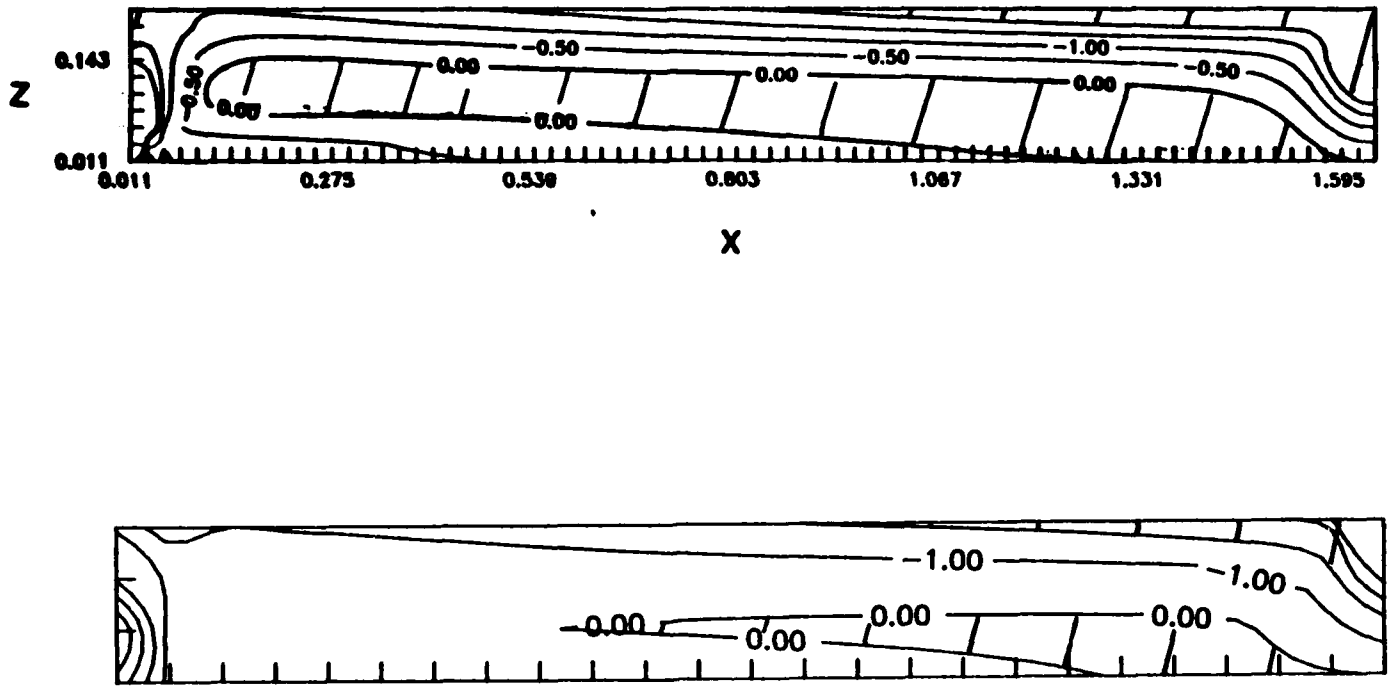

Figure 29. Tsai-Wu Failure Criteria, 2Ø Ply Top (8:75) and 3Ø Ply Bottom, L/d=15, R=85%

shows there should be damage at the top and bottom of the beam center where there was none reported. Conversely, damage caused by flexural compression buckling at the top and tensile stress near the bottom center was observed in the thirty ply beams, but there was none to be seen near the neutral axis. In the case of the thirty ply beam, the predicted displacement coincided with the experimentally measured displacement within five percent. It could be that the cracks which initiated at eighty-six percent of peak load in the top and bottom ply precluded further damage from occurring near the neutral axis. Also, the microstresses in the actual woven tows are not modeled by the finite elements, so a perfect match between experimentation and theory should not be expected.

To gain a different perspective on the crack propagation mechanism, scanning electron microscopy was utilized. The first crack surface observed was that of the long split in the fifteen to one beam after final failure was reached. In Figure 30, the location of the examined fracture surface is shown in a sketch. The photograph below it shows how the crack at the beam edge looks when viewed with an electron microscope. Here the crack can be seen between the tows of a single ply. In addition, there is an

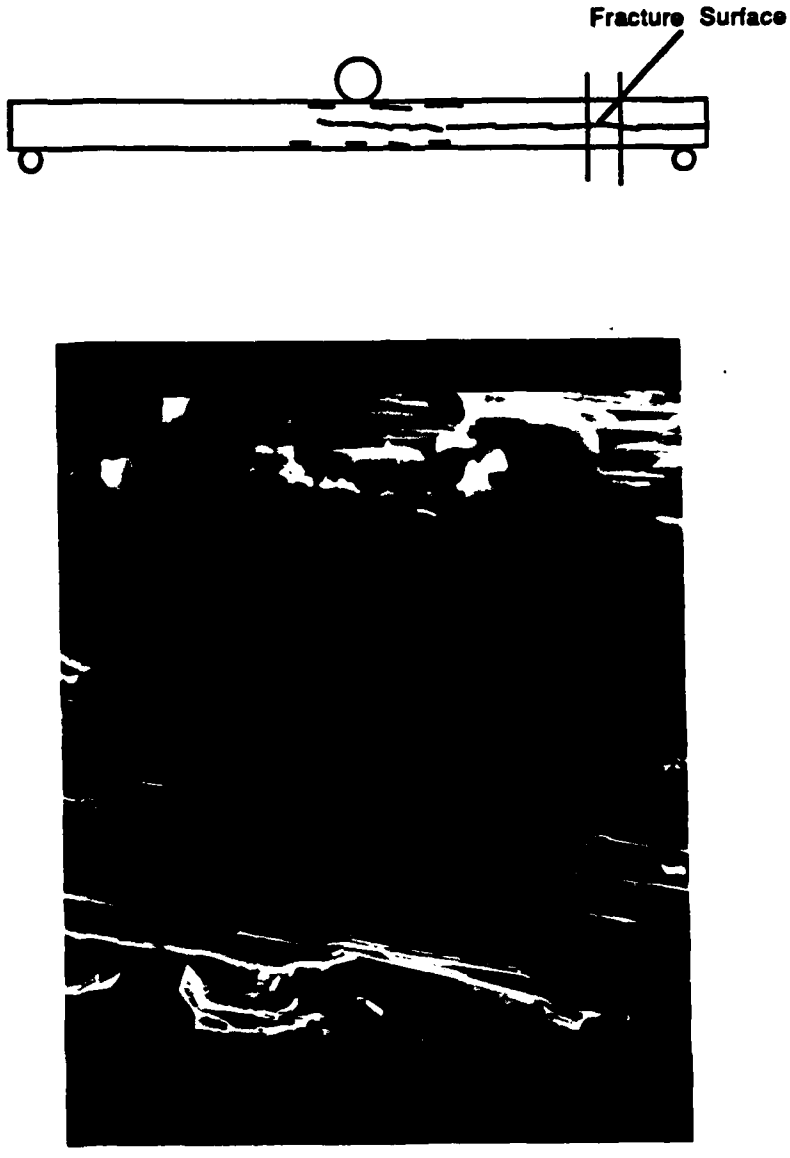

Figure 30. Schematic at Crack Location and Electron Micrograph of Same Crack at the Edge of the Beam.

angled shear crack through the middle of a fill tow, that is, a tow perpendicular to the crack front propagation.

A second surface was examined with the electron microscope. This was one of the buckling induced cracks which formed about a tenth of an inch to the side of the indenter in the topmost ply. Figure 31 shows the location of this particular crack and a photograph of what it looked like at the polished edge before it was cut out for electron microscope examination of the fracture surface. The fracture surface was exposed by cutting the sides of the top bit of cracked ply and then gently pulling it out. Not much force was required, but the piece did not fall out, even though it had been cut all the way around so that no fibers connected it at the top to the surrounding fibers. The fracture surface was not interlaminar because, as can be seen in Figure 32, there are perpendicular fibers visible both on top and bottom of a single tow.

From electron microscope photographs, it may be possible to characterize the failure based on the fracture surface since a tensile failure in the fiber direction would show broken fibers, and a tensile stress perpendicular to the laminate plane may look more interlaminar. However, the crack at the top was heavily induced by fiber buckling and virtually no distinction could be made between it and the long split crack at the neutral axis, which was induced

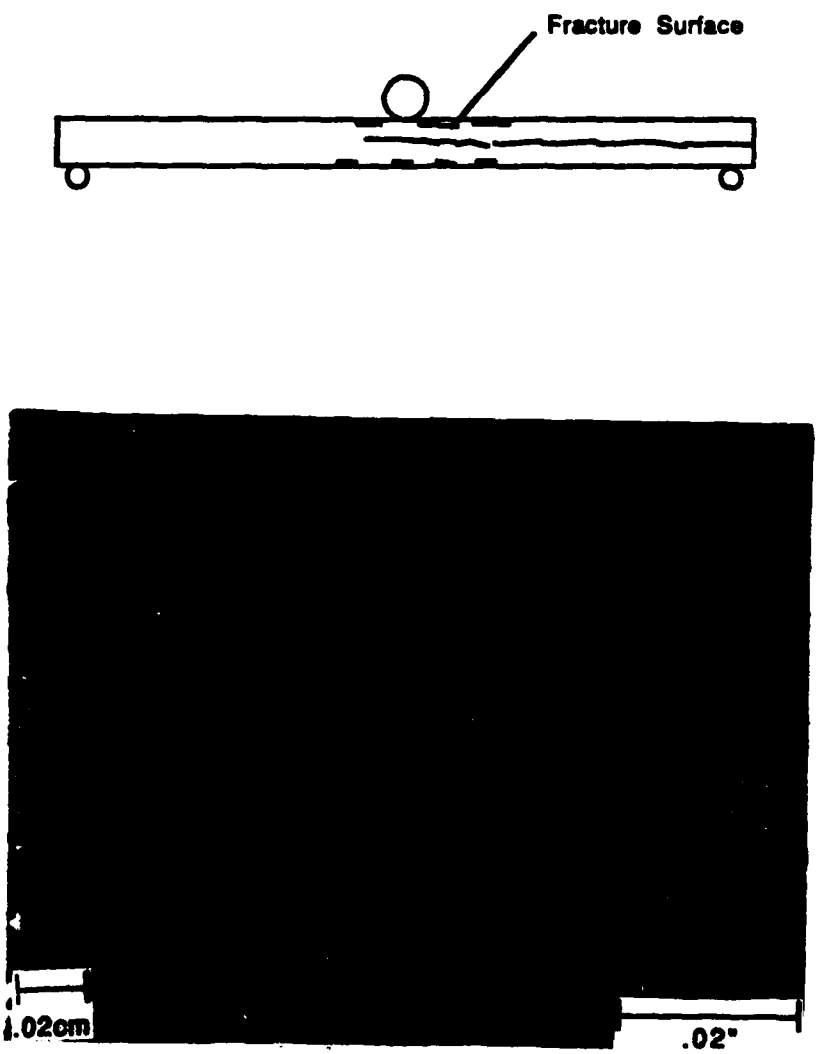

Figure 31. Schematic Showing Location at Matrix Crack and Optical Micrograph of the Crack at the Beam Edge, 50x.

mainly by transverse shear stress. One can conclude that the fracture cracks always travel through the matrix, both within and between lamina.

Radio-opaque nondestructive inspection of the long split after failure revealed that it was continuous through the thickness because the penetrant went clear through the beam from face to face. This is shown in Figure 33 where the areas which were cracked absorbed the radio-opaque dye. The x-rays could not expose the film beneath these areas, leaving them dark. In the plan view shown at the top of Figure 33, the entire edge where the radio-opaque dye was applied is dark due to porosity, though the side view shows that one side was not split.

Results with the Two and One Half Inch Steel Indenter

The previous beams were tested in accordance with ASTM 2344. The specification required that the center load pin have a diameter of one quarter inch, while the two support pins have an eighth inch diameter. By increasing the diameter of the indenter, it was supposed that the contact area would be lengthened so that more contact damage could be studied. The four to one span to depth ratio beams tested with the quarter inch indenter had proven that ultimate failure was dominated by the indenter and load pin

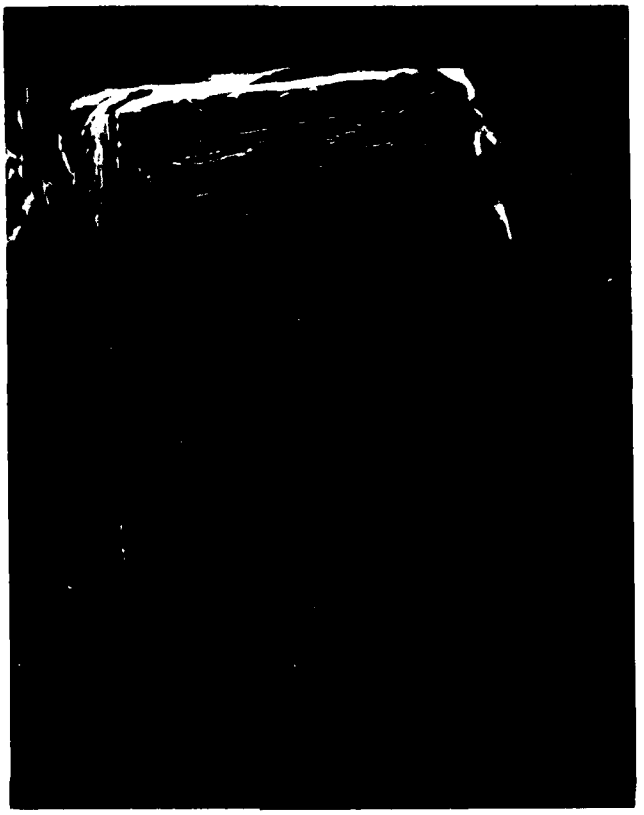

Figure 32. Electron Micrograph of the Fracture Surface of the Horizontal Matrix Crack

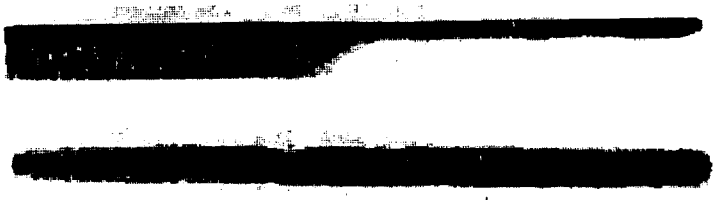

Figure 33. X-Ray of the Long Beam Plan View (Top) and Side View (Bottom), 30 Ply, L/d=15, R=100%.

stress fields. Dense microcracking was heaviest near the points of contact. Next, an indenter with a two and one half inch diameter was employed.

Below this two and one half inch diameter indenter, a tow separation crack between the warp and fill tows of the top ply was first observed at thirteen percent ultimate load. A typical micrograph was shown in Figure 14, and at a higher load in Figure 34. Thirteen percent was almost the same level such damage was observed when the one quarter inch indenter was used, but because polishing strained the carbon matrix on the surface, a better comparison between the two indenters is the load level at which fiber fracture first occurred below the indenter. The two and one half inch diameter indenter suppressed fiber fracture at the contact point until eighty-five percent, an increase of twenty percent, compared to the load level at which the same type of cracking occurred under the one quarter inch indenter. For comparison, the load levels at which matrix and fiber damage occurred below the one quarter inch indenter and the two and one half inch indenter are shown in Table 8.

Table 8. Indenter Size Comparison, 30 Ply, L/d=4

Indenter	Span Depth	Tow Separation at Indenter	Outer Ply Failure at Indenter	Angled Shear Cracks at Neutral Axis
1/4" dia	4:1	11%	65%	76%
2 1/2" dia	4:1	13%	85%	71%

The difference between the load level that cracks first appeared at the neutral axis in the beams tested with the quarter inch and two and one half inch indenter was just five percent, which was within the experimental scatter. The final pattern of damage, shown for the beam tested with the two and one half inch indenter in Figure 35, was practically the same as the final pattern of damage in the beam tested with the quarter inch indenter shown back in Figure 18. Neither was the ultimate load withstood by the beam affected by the indenter size. It did not vary by more than two percent.

When the one quarter inch indenter was used, the final failure mode of the long beams with the fifteen to one span to depth ratio was a long shear split along the neutral axis. The large indenter could not be expected to change this damage pattern. At maximum load, no microcracks were evident at the neutral axis. Rather, the growth of buckling induced cracks in the top ply out from the indenter caused the release of maximum load. The purpose of testing the

Figure 34. Matrix Crack Between Top Two Tows, 30 Ply, L/d=4, R=56%, 100x, Large Indenter.

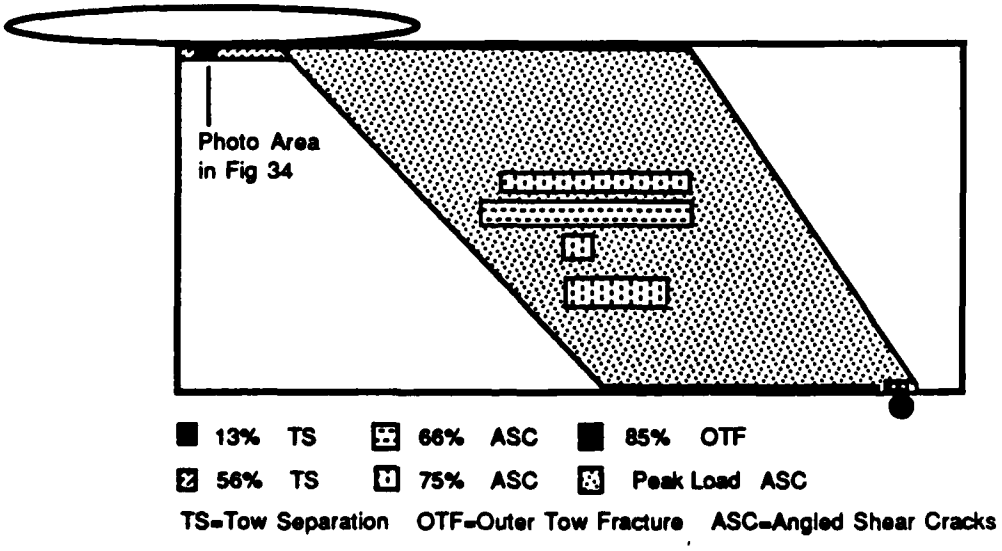

Figure 35. Areas and Load Levels Where Microscopic Damage was First Observed on the Polished Face of the Beam, 30 Ply, L/d=4, Large Indenter

beams with the fifteen to one span to depth ratio with the larger indenter was to further study the damage to the top ply.

First damage was seen at a support pin at sixty-one percent as tow separation between the topmost warp and fill tows. With the large indenter there was no fiber fracture directly under the indenter until eighty-nine percent ultimate load, whereas it had appeared at sixty-seven percent in the beam with the standard indenter. The first damage near the large indenter did not occur directly below it, but in the first ply, about two tenths of an inch to the right at eighty percent of maximum load. It was a fiber buckling induced matrix crack in a fill tow just like what was seen in the beam tested with the standard indenter, shown in Figure 36. For comparison, the levels at which matrix and fiber cracks initiated in the region of the quarter inch and two and one half inch indenter are shown in Table 9.

Table 9. Indenter Size Comparison, 30 Ply, L/d=15

Indenter	Span Depth	Tow Separation Below Indenter	Outer Ply Failure Below Indenter	Top Ply Buckling Cracks
1/4" dia	15:1	51%*	67%	86%
2 1/2" dia	15:1	61%	89%	80%

*lowest load level tested

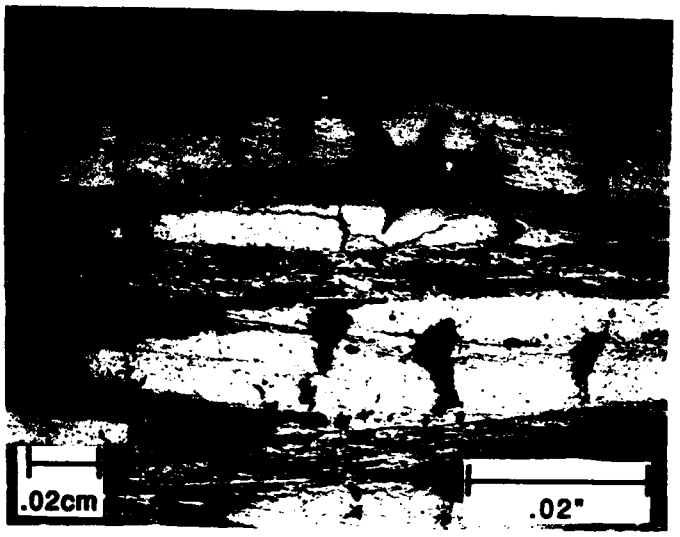

Figure 36. Fiber Buckling Induced Crack, 30 Ply, L/d=15, R=80%, Large Indenter, 50x.

A crack occurred at the bottom of the beam after eighty percent ultimate load. It was also in the form of a long 1.27 mm (0.05 inches) wavy horizontal crack and, as shown in Figure 37, it looked very much like the horizontal crack seen at the top at this load level. This is because on the microstructural level, the stress which caused both cracks at the top and bottom in the matrix was the same type, i.e., tensile stress. Except at the bottom, the undulating tows supported the flexural tensile stress and began to straighten, which pulled the matrix apart. Cracks at the bottom were not observed with the beams tested with the standard indenter. Because the indenter size could not be

not be expected to have much effect at the bottom of the beam, this shows how the density of the cracks in each beam varies slightly due to porosity, polishing pressure, and random chance.

The effect of the two and one half inch diameter indenter in the beams with the fifteen to one span to depth ratio was to raise the level at which fiber fracture was observed beneath the indenter by twenty-two percent to eighty-nine percent of ultimate load. The ultimate load that the beam could sustain was unchanged by the larger indenter. As can be seen from Figures 28 and 38, the pattern of microscopic damage was nearly identical for the beams tested with either indenter.

In both the case of the long and short beams, the two and one half inch indenter raised the load level at which fiber fracture occurred below the indenter by nearly twenty percent. This is because the larger indenter's contact was longer, which reduced the contact compression load and shifted the maximum local shear further out from the indenter. But it did not affect the pattern of microscopic damage in either case, nor did it affect the the ultimate load the beam could sustain.

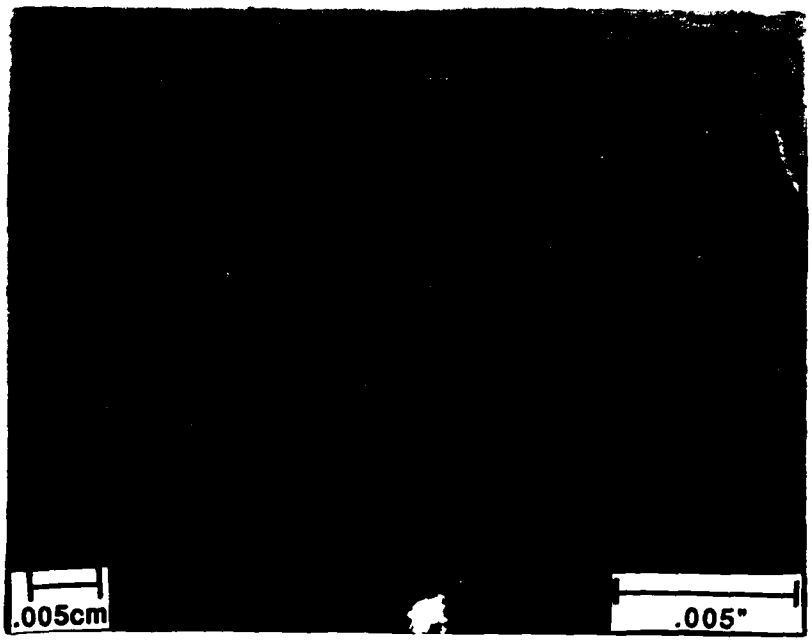

Figure 37. Matrix Crack in Bottom Ply, 7.5 mm (.3 Inches) to Right of Center, 3Ø Ply, L/d=15, R=80%.

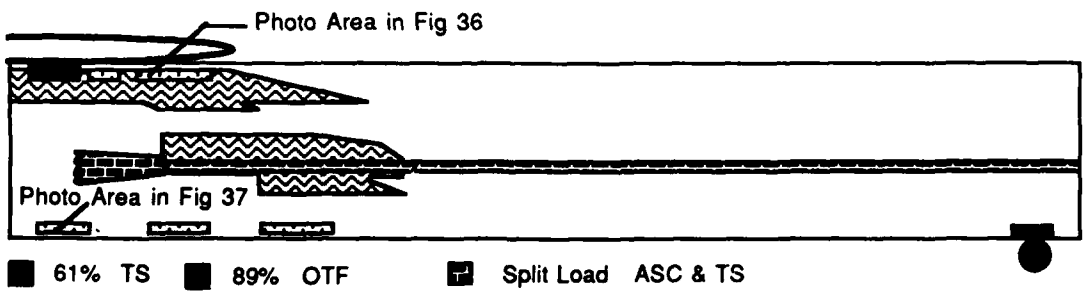

Figure 38. Area and Load Levels Where Microscopic Damage was First Observed on the Polished Face of the Beam, 3Ø Ply, L/d=15, Large Indenter.

Results with the Rubber Cushioned Indenter

With the steel indenters, the most severe damage in the beam at maximum load was directly below the contact point. It appeared that to raise the load bearing capacity of the beam, a method of applying the load was needed which changed the overall pattern of damage to shear. Otherwise the apparent ultimate load of the beam which could be measured by the test would be significantly reduced. To confirm this, a three point bend test was needed which would not crush the material directly below the indenter.

Two thirty ply [Ø/9Ø] samples were tested with the central indenter and support pins cushioned by one tenth inch thick pads made from vulcanized rubber tubing. Before using the rubber on the carbon-carbon, it was tested between a flat steel platen and the standard one quarter inch ASTM 2344 steel indenter. As can be seen in Figure 71 of the Appendix, the load-displacement curve was nonlinear, becoming exponentially harder with increasing load.

In testing the carbon-carbon samples with the rubber support pads, the load-displacement curve was similarly nonlinear. Also, because of the rubber load relaxation effect, the point at which the four to one beam's load-displacement curve began to bend over to the ultimate load is more clearly delineated and the peak of the ultimate load was much sharper. As with the samples tested with the

steel indenter, this was between eighty-eight and ninety-two percent of the ultimate load.

The ultimate loads of the two beams with four to one span to depth ratio tested using the rubber cushions were within 2.3 percent of each other. Their average was 7.7 percent higher than the average ultimate load of the samples tested with the steel indenters, large or small. The areas and load levels where microscopic damage was first observed on the polished face of the beam are sketched in Figure 39.

Microscopic examination for damage showed that the rubber cushions were effective in preventing damage at the indenter and load pins. In the first sample, a minor crack in a matrix fissure beneath the indenter was seen after forty percent of ultimate load, but it did not spread as the load increments were increased, and matrix cracking did not occur. In the second sample, just below the cushioned indenter the top ply bridged a long void. This bridge immediately collapsed with the first load increment to sixty-nine percent. But again this damage did not spread with further load increments. For comparison, Figures 40 and 41 show the damage beneath the cushioned indenter and the standard steel indenter, both at about ninety percent of the ultimate load. Below the uncushioned indenter there is

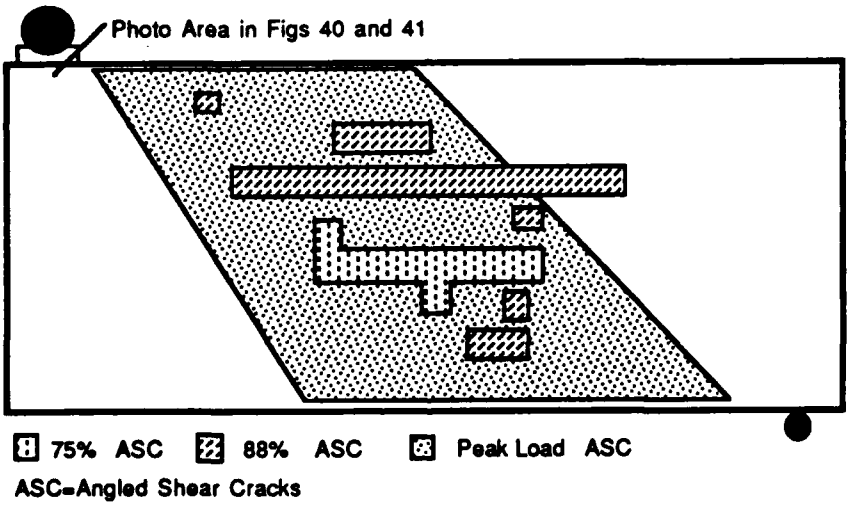

Figure 39. Areas and Load Levels Where Microscopic Damage was First Observed on the Polished Face of the Beam, 30 Ply, L/d=4, Cushioned Indenter.

Figure 40. Damage Directly Below Indenter, 30 Ply, L/d=4, R=87%, Cushioned Indenter, 100x.

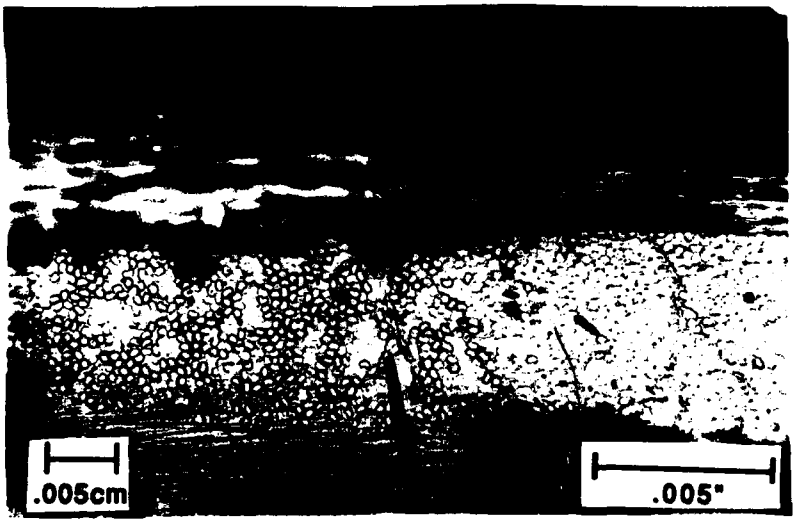

Figure 41. Damage Directly Below Indenter, 30 Ply, L/d=4, R=89%, Standard Steel Indenter, 200x.

extensive matrix cracking in the first fill layer, and outer ply failure has occurred. Below the cushioned indenter, little change is evident.

When the cushioned indenter was used, the first angled shear cracks occurred in the sample interior after it was loaded to the seventy-five percent level, which was practically the same load that they were first observed in the tests with the uncushioned indenter. This is another confirmation that the initiation level of angled shear cracks at the neutral axis is relatively independent of the local indenter stress field. These cracks grew more common when the load was increased to eighty-eight percent of ultimate load, visible throughout the region shown in Figure 39.

Rubber pads cushioned the support pins and indenter for a test of a beam with span to depth ratio of fifteen to one. It supported an ultimate load which was nearly twelve percent higher than the average of the samples tested with the quarter inch steel indenter.

Figure 42 shows the diagram of the internal damage caused by the increasing load increments. No damage occurred below the cushioned indenter, other than enhancement of some polishing disturbances of the smeared matrix.

At peak load there was minor outer ply fracture and tow separation in the ply directly beneath the cushioned indenter as shown in Figure 43. There were buckling induced wavy cracks in the top ply, but they began out 2.5 mm (Ø.1 inches) from either side of the indenter and went a third of the distance toward the support pins. In this sample, these buckling cracks extended out twice as far in the top ply compared to beams tested with the steel indenters. Even some tows buckled as shown in Figure 44. Deeper into the thickness there were the tiny angled shear cracks near the neutral axis in the area shown by Figure 42, but they were uncommon, and hard to find. At the bottom, flatwise tensile cracks up to 2.5 mm (Ø.1 inches) long went out on both sides of center to half an inch. These were like those observed in the sample tested with the large steel indenter and shown in Figure 37.

The tests on the beams with both the four to one and fifteen to one span to depth ratio showed that cushioning the indenters and supports changed the pattern of microscopic damage. Matrix cracking and fiber breakage under the cushioned indenter were eliminated. Table 1Ø shows the difference in initiation levels for the beams tested with the quarter inch steel indenter and the rubber cushioned indenters.

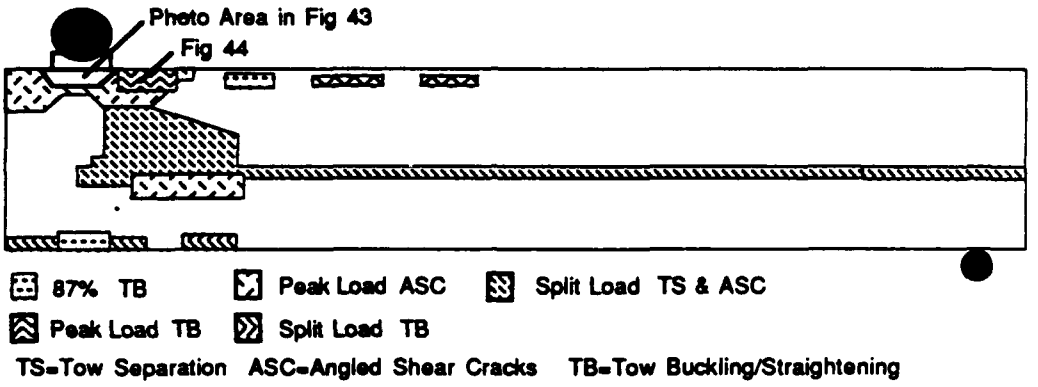

Figure 42. Area and Load Levels Where Microscopic Damage was First Observed on the Polished Face of the Beam, 30 Ply, L/d=15, Cushioned Indenter.

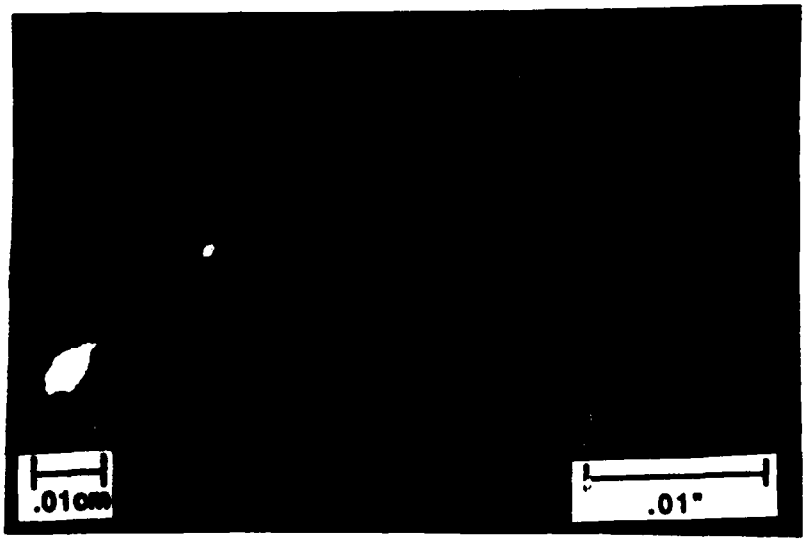

Figure 43. Very Little Matrix Damage Below the Cushioned Indenter, 30 Ply, L/d=15, R=100%.

Table 10. Rubber Cushioned Indenter Comparison, 30 Ply

Indenter	Span/ Depth	Tow Separation Below Indenter	Outer Ply Failure Below Indenter	Angled Shear Cracks at N. A.
1/4"	4:1	11%	65%	76%
Rubber	4:1	None	None	75%
1/4"	15:1	51%	67%	100%
Rubber	15:1	None	None	100%

The apparent strength of the beam when the loads were cushioned was raised by eight percent when the span to depth ratio was four to one and by twelve percent when the span to depth ratio was fifteen to one. This proved that damage caused by the steel indenters reduced the strength which was measured.

Results of Beams with Cross Ply Laminates

Because the fibers support the load in this composite, the failure made initiation load levels and areas were expected to depend on ply orientation. A second laminate layup was tested with the orientation [0/45]. In the woven plies oriented at forty-five degrees, all the tows supported the load equally. The same incremental three point bend test and examination procedure was employed as before to find out if any new failure modes would occur or if the order of appearance of the already known failure modes would change.

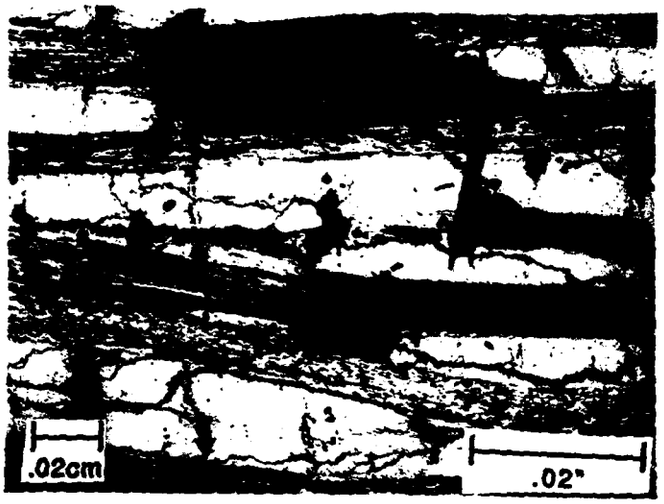

Figure 44. Buckled Tows, L/d=15, Peak Load, Cushioned Indenter, 50x.

The load displacement curve of the thirty ply short beam was very similar to the load displacement curve of the same geometry but [0/90] layup. Tow separation which occurred at eleven percent load and thirteen percent load respectively in the [0/90] and [0/45] beams was hardly affected by the change in layup. Neither was outer ply failure which occurred at just a nine percent lower load level in th. short beam with [0/90] layup. The big difference in the damage pattern between beams of the two layups manifested itself in the angled shear crack failure mode.

At the forty-five percent load level, angled shear cracks were observed in the short beam in the top ply forty-five degree ply, in the forty-five degree plies at the neutral axis, and in the forty-five degree plies at the bottom of the beam. In the long beam with the [Ø/45] layup, the same pattern of damage began in the forty-five degree plies at just forty-three percent of ultimate load. Except for directly below the indenter, all of the damage sketched in Figures 45 and 46 is for angled shear cracks in forty-five degree plies. Figure 47 shows a typical angled shear crack in a forty-five degree ply. As can be inferred from the magnification of this photograph, the cracks in the forty-five degree plies were very tiny.

In the long thirty ply beams with the [Ø/45] layup, the buckling mode was not observed. This failure mode, which played a cr tical role in the peak load of the [Ø/9Ø] beams, was instead replaced by complete tow separation of the forty-five ply at the top and bottom of the beam, as shown in Figure 48.

Comparing the failure modes observed in the [Ø/9Ø] and [Ø/45] laminate layups, no new failure modes were observed, but the pattern of the damage was significantly affected. Very small angled shear cracks initiated in the forty-five degree plies of both the short and long beams between forty and fifty percent of the ultimate load. This might be due

to the shear component introduced to the forty-five degree plies by rotation which works against the very low shear strength of this material. By comparison, angled shear cracks did not initiate in the short [Ø/9Ø] beams until seventy-six percent of the ultimate load, and not until peak load in the long [Ø/9Ø] beams.

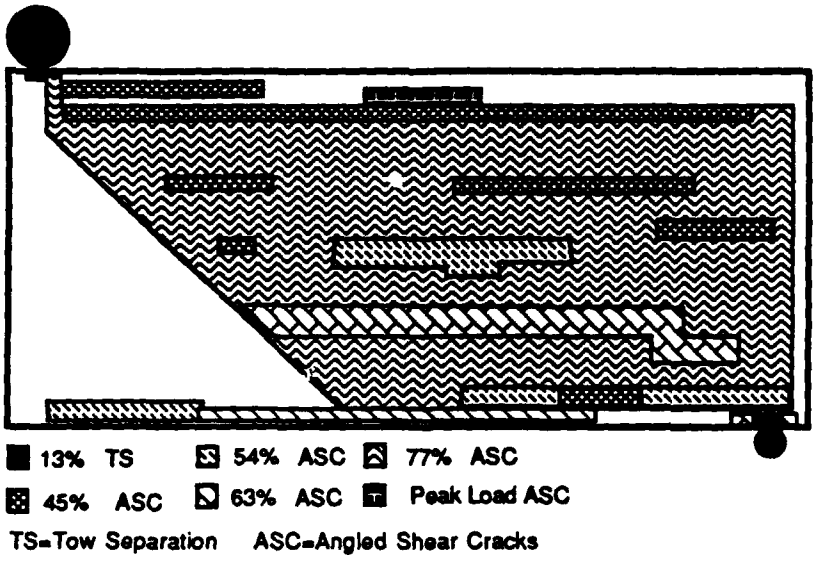

Figure 45. Areas and Load Levels Where Microscopic Damage was First Observed on the Polished Face of the Beam, 30 Ply, L/d=4, [0/45].

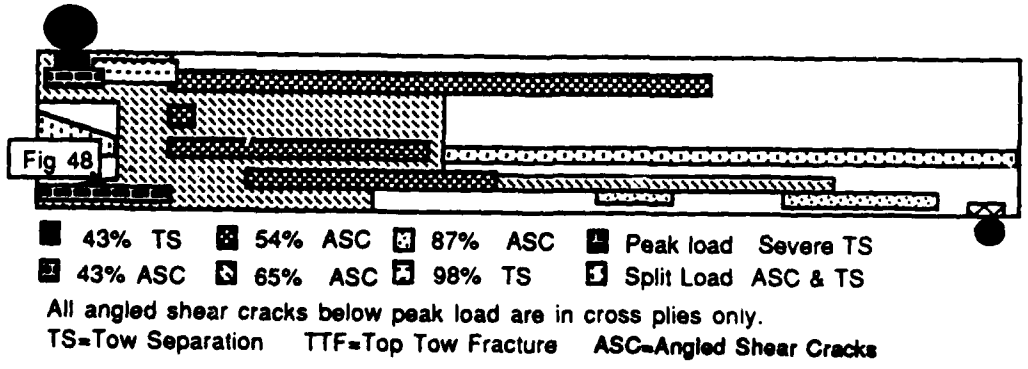

Figure 46. Areas and Load Levels Where Microscopic Damage was First Observed on the Polished Face of the Beam, 30 Ply, L/d=15, [0/45].

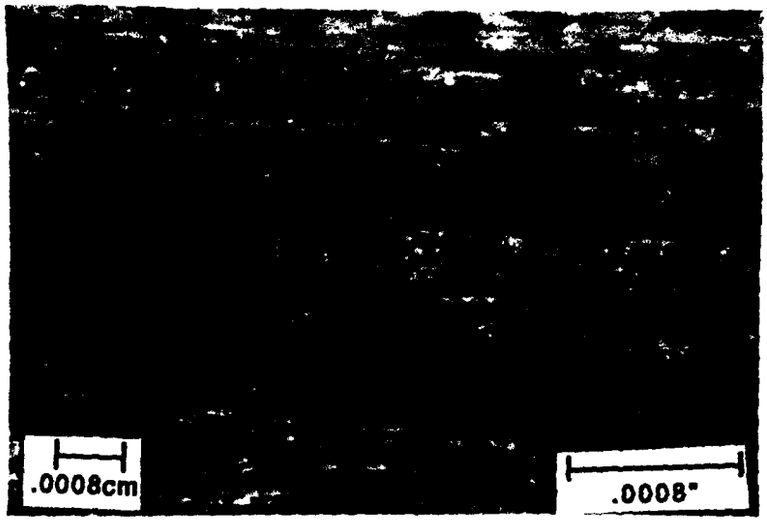

Figure 47. Typical Matrix Crack in a Forty-Five Degree Ply, 1200x.

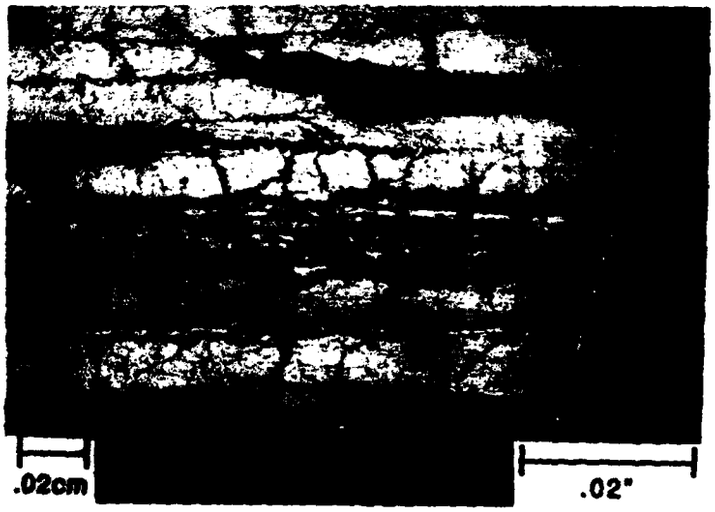

Figure 48. Tow Separation in the Bottom Forty-Five Degree Ply at Peak Load, L/d=15, 50x .

V. CONCLUSIONS

Most of the goals of this thesis were completed through the experimental and analytical work performed. Damage in woven carbon-carbon was thoroughly characterized by varying the parameters related to the test geometry and material layup. Experimentally, the damage on the polished beam edge was shown to be representative of the damage occurring through the thickness. The accuracy of the finite element method in combination with the Dendis post processor was confirmed on beams thirty plies thick.

Four distinct failure modes were observed. They did not all occur under all conditions, but in general, tow separation below the indenter was followed by outer ply fracture, which was followed by angled shear cracks at the neutral axis. In the long thick beams, tow buckling was the final failure mode before peak load occurred. The first two failure modes, tow separation and outer ply fracture, were both caused by the very high compression and shear stress due to indenter contact. The angled shear crack mode occurred in the matrix between fibers, and at peak load it could be seen in the short beams practically everywhere between the central indenter and support pins. The fiber

buckling mode which occurred at the top of the thick, long beams was due to the geometry of the microstructure which transformed the global compressive stress through buckling of the fibers to localized tensile stress in the adjoining matrix. A similar failure mode occurred at the bottom of the long thick beams where the global tensile stress pulled the undulated fibers straight, resulting in a local tensile stress in the matrix adjacent to the fibers. Table 11 shows the order of occurrence of each failure mode for each combination of three point bend parameters.

To observe the effect of beam thickness on the damage initiated in three point bend, beams of twenty and thirty plies were tested. The thicker beam supported a higher ultimate load so that the effect of higher contact load could be studied. These beams were also stiffer so that the global stress field changed slightly.

The effect of thickness on the first failure mode, tow separation, was to lower the load level at which it was first observed from thirty-six to eleven percent, but the initiation of tow separation was always faint cracking on the surface. In light of the fact that the matrix on the surface was affected by polishing, outer ply fracture was a better gage of the effect that the thicker beam had on indenter contact damage. The load percentage at which outer ply fracture occurred differed by less than four percent

Table 11. Order of Failure Mode Appearance

		Short Beam					Long Beam				
	Indenter	1/4	1/4	2.5	C	1/4	1/4	1/4	2.5	C	1.4
	Thickness	20	30	30	30	30	20	30	30	30	30
	Layup	0/90	0/90	0/90	0/90	0/45	0/90	0/90	0/90	0/90	0/45
Failure Mode	Tow Separation	1	1	1	--	1	1	1	1	--	1
	Top Tow Fracture	2	2	2	--	2	2	2	3	--	2
	Angled Shear Cracks	3	3	3	1	1	3	--	--	--	1
	Buckling	--	--	--	--	--	--	3	2	1	--
	Cross Ply Separation	--	--	--	--	--	--	--	--	--	3

between the thicknesses for both the short and long beams. The level at which angled shear cracks occurred was raised from sixty-seven to seventy-six percent for the short beams and from sixty-three percent to peak load for the long beams when the thickness was increased. The dramatic rise in the level where angled shear cracks were observed in the long thick beam may be related to the appearance of another failure mode. In this beam, a buckling phenomena was observed on the microstructural level of the tows. It appeared at eighty-six percent of peak load and had the effect of causing tensile cracks in the matrix adjacent to the buckling tows.

Two of the failure modes occurred within the radius of the local indenter stress field: tow separation and outer ply failure. In addition, matrix tensile cracks, which were the by-product of the top ply buckling mode, were suppressed by the high amount of compression in the local indenter stress field. By varying the indenter size and rigidity as test parameters, it was possible to learn more about these failure modes.

Two indenter types were employed to compare to the standard quarter inch diameter steel indenter. The first was a steel indenter with ten times the radius, and the second was a rubber cushioned indenter. In combination with

the two span to depth ratios and four failure modes, this produced twenty-two different combinations of test results.

Under the large steel indenter, the outer ply failure mode initiation level was raised by twenty percent in the short beams and by twenty-two percent in the long beams. However, this is misleading since at peak load the damage under both the large and standard indenters was clearly equally severe with drastic tow separation and outer ply fracture present. This change in indenter produced no change in the amount of load either the short or long beam could sustain, neither did it produce any significant change in the initiation level of either angled shear cracks in the short beams or the buckling mode in the long thick beams.

Cushioning the indenter had a significant effect on three of the failure modes. For both the short and long beams, cushioning the indenter suppressed tow separation and outer ply fracture until peak load. The failure mode which was not affected was the initiation of angled shear cracks which differed by only one percent in initiation load level between the beams tested with the quarter inch steel indenter and the cushioned indenter.

The buckling mode was initially suppressed by use of the cushioned indenter, but when it did appear at peak load it was more severe than in the tests using a steel indenter.

The matrix tensile cracks caused by this mode extended out from the indenter halfway to the end of the beam and some fiber buckling was even observed.

Changing the layup of the beams to [Ø/45]s had a dramatic effect on the stresses present in the tows in a microstructural level, at least in the forty-five degree plies. In these plies, the stresses were carried equally by all the tows in the weave. In the short beam, the result was angled shear crack initiation in the forty-five degree tows at the top, neutral axis, and bottom at just the forty-five percent load level. With increasing load, the forty-five degree plies in between them also initiated angled shear cracks so that by the seventy-seven percent load level, all the forty-five degree plies contained angled shear cracks. In the long beams, angled shear cracks initiated in the top and bottom forty-five degree plies at forty-three percent and at the neutral axis at fifty-four percent ultimate load. The buckling phenomena observed in the long thick [Ø/9Ø]s beams was not seen in the [Ø/45]s beams.

The finite element model of the three point bend carbon-carbon specimen did a good job of combining the local indenter field with the overall stress field of the beam to produce an accurate global stress field. It was, however, based on a manageable approximation of the actual beam.

Very near the indenter contact point and on a microstructural level, the model broke down. It was still very useful for showing how the global tension, compression, and shear stresses varied throughout the beam. And Dendis' Tsai-Wu post processor computed the initiation levels of angled shear cracks within ten percent. If the actual stiffness matrix was ten percent higher due to better cure and compaction than the average properties used in the model, then the model displacements agreed with the measured displacements within experimental accuracy.

Bibliography

1. American Society for Testing and Materials. 1985 Annual Book of ASTM Standards, Section 4, Volume Ø4.Ø9. Philadelphia PA (538-543).

2. American Society for Testing and Materials. 1985 Annual Book of ASTM Standards, Section 15, Volume 15.Ø3. Philadelphia PA (55-58).

3. Berg, C. A., J. Tirosh, and M. Israili. "Analysis of Short Beam Bending of Fiber Reinforced Composites," Composite Materials: Testing and Design (Second Conference), ASTM STP 497, 2Ø6-218. American Society for Testing and Materials, 1972.

4. Brahney, James H. "Carbon-Carbon, Heat Means Strength," Aerospace Engineering, 11-14 (June 1987).

5. Browning, C. E., F. L. Abrams, and J. M. Whitney. "A Four-Point Shear Test for Graphite/Epoxy Composites," Composite Materials: Quality Assurance and Processing, ASTM STP 797, 54-74, edited by C. E. Browning, American Society for Testing and Materials, 1983.

6. Copp, P. D., J.C. Dendis, and S. Mall. "Characterization of Damage Initiation in Three Point Bend Specimens of Advanced Woven Carbon-Carbon Composite Materials," Proceedings from the American Society of Composites Symposium on High Temperature Materials. 262-272. Dayton: Technomic, Lancaster PA, 1989.

7. Copp, Paul D. Smooth Contact of a Rigid Indenter and a Beam of Two Orthotropic Layers. Ph.D. dissertation, Northwestern University, Evanston IL. December 1986.

8. Dendis, Capt. James C. Damage Initiation in Two-Dimensional, Woven, Carbon-Carbon Composites. MS Thesis AFIT/GAE/AA/88D-7. School of Engineering, Air Force Institute of Technology (AU), Wright-Patterson AFB OH December 1987.

9. Dupont, Capt. Deon T. Damage Initiation in the Short Beam Shear Test of Composite Materials. MS Thesis, AFIT/GAE/AA/87D-5. School of Engineering, Air Force Institute of Technology (AU), Wright-Patterson AFB OH, December 1987 (AD-A194880).

10. Pagano, N. J. "Exact Solutions for Composite Laminates in Cylindrical Bending," Journal of Composite Materials, 4: 330-343 July 1970.

11. Rosensaft, M. and G. Marom. "Evaluation of Bending Test Methods for Composite Materials," Journal of Composite Technology and Research, 7/1:12-16 (Spring 1985).

12. Sines, George, Zheng Yang, and Brian D. Vickers. "Effect of the Matrix on the Creep Behavior of Carbon-Carbon Composites," Technical Report UCLA-ENG-87-44. School of Engineering and Applied Science, University of California, Los Angeles, November 1987 (AD-A193211).

13. Whitney, J. M. "Elasticity Analysis of Orthotropic Beams Under Concentrated Loads," Composites Science and Technology, 22: 167-184 (1985).

14. Whitney, J. M. and C. E. Browning, "On Short Beam Shear Tests for Composite Materials," Experimental Mechanics, 25: 294-300 (1985).

Appendix: Data Discussion and Load Displacement Curves

Table 12. Specimen Details

Specimen*	Width x Height (mm)	Indenter**	Ultimate Load (N)
A24-1	7.038 x 6.038	S	896
A24-2	10.693 x 5.791	S	1213
A34-1	11.430 x 8.448	S	1709
A34-2	11.463 x 8.448	S	1717
A34-3	9.975 x 8.451	S	1521
A34-4	10.963 x 8.448	C	1745
A34-5	10.122 x 8.448	C	1650
A34-6	10.165 x 8.448	B	---
A34-7	9.665 x 8.448	B	1459
A315-1	11.316 x 8.364	S	1036
A315-2	11.057 x 8.364	S	1025
A315-3	10.866 x 8.364	C	1121
A315-4	10.851 x 8.364	B	1011
A315-5	10.510 x 8.364	C	983
B24-1	10.424 x 5.476	S	1434
B34-1	10.810 x 8.656	S	1880
B215-1	12.276 x 5.580	S	756
B315-1	10.704 x 8.501	S	885

*A = [0/90] Layup
B = [0/45] Layup
**S = 1/4" Steel
B = 2 1/2" Steel
C = Cushion

Angled Initiation Levels of Angled Shear Cracks

The level at which angled shear cracks appeared near the neutral axis is shown in terms of the maximum shear stress according to Eq (1) times the initiation load level percentage. Shear stresses reported are the average of the two or three samples tested.

Table 13. Angled Shear Crack Initiation Levels in Terms of Shear Stress.

Thickness	Indenter	Initiation Level (%)	Maximum Shear (Mpa)	Initiation Shear (Mpa)	L/d
30 Ply	S	100%	8.3	8.3	15
30 Ply	S	76%	13.3	10.1	4
30 Ply	B	71%	13.4	9.5	4
30 Ply	C	75%	14.1	10.6	4

S = 1/4"; B = 1.5"; C = Pad.

The true shear stress as reported in Table 2 was 6.9 Mpa, which just confirms that Eq (1), based solely on classical isotropic beam theory, is not very useful as a calculation of the shear stress. Also, the values for the long beam are completely misleading since it failed by buckling.

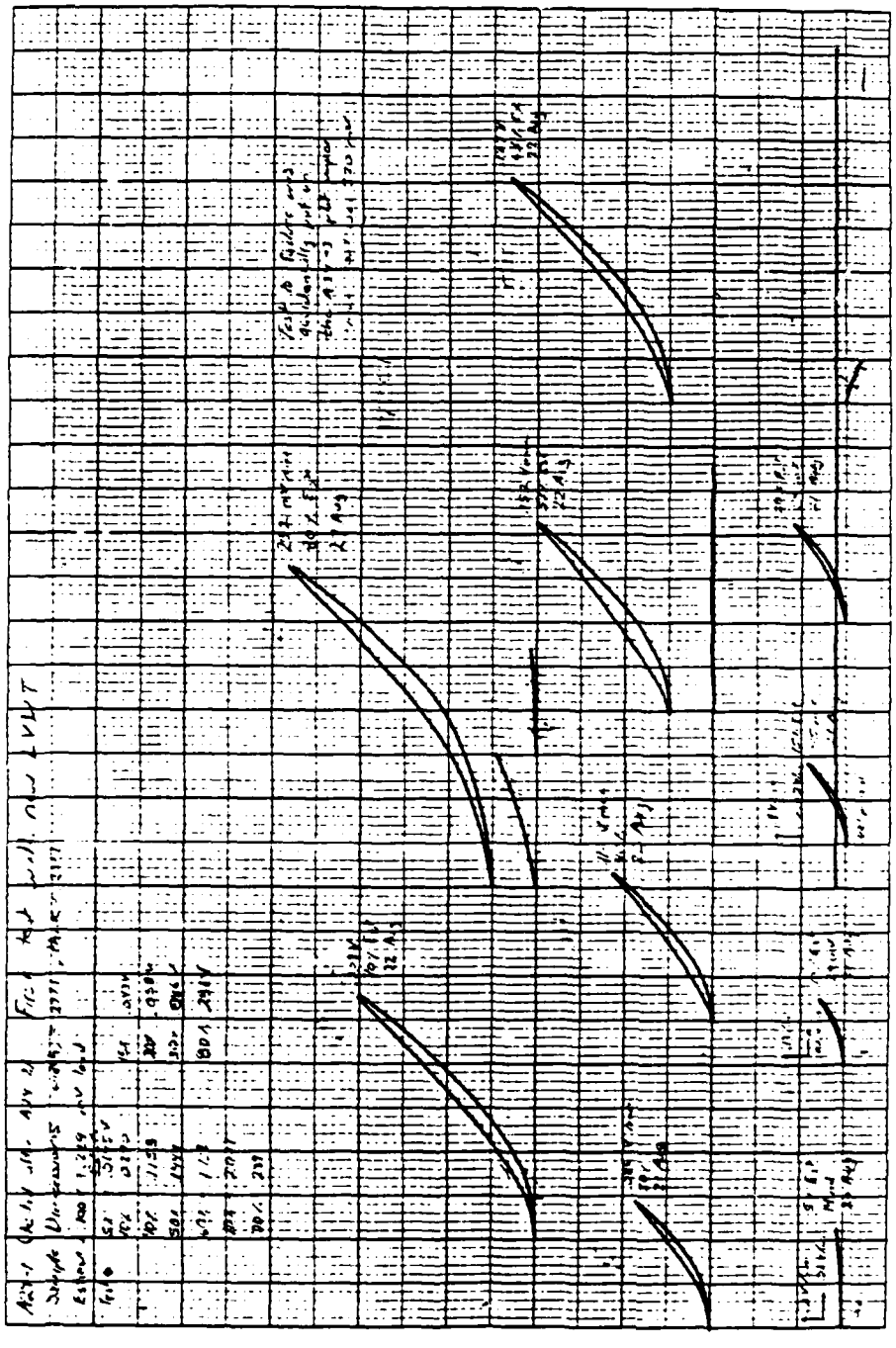

Figure 49. Specimen A24-1

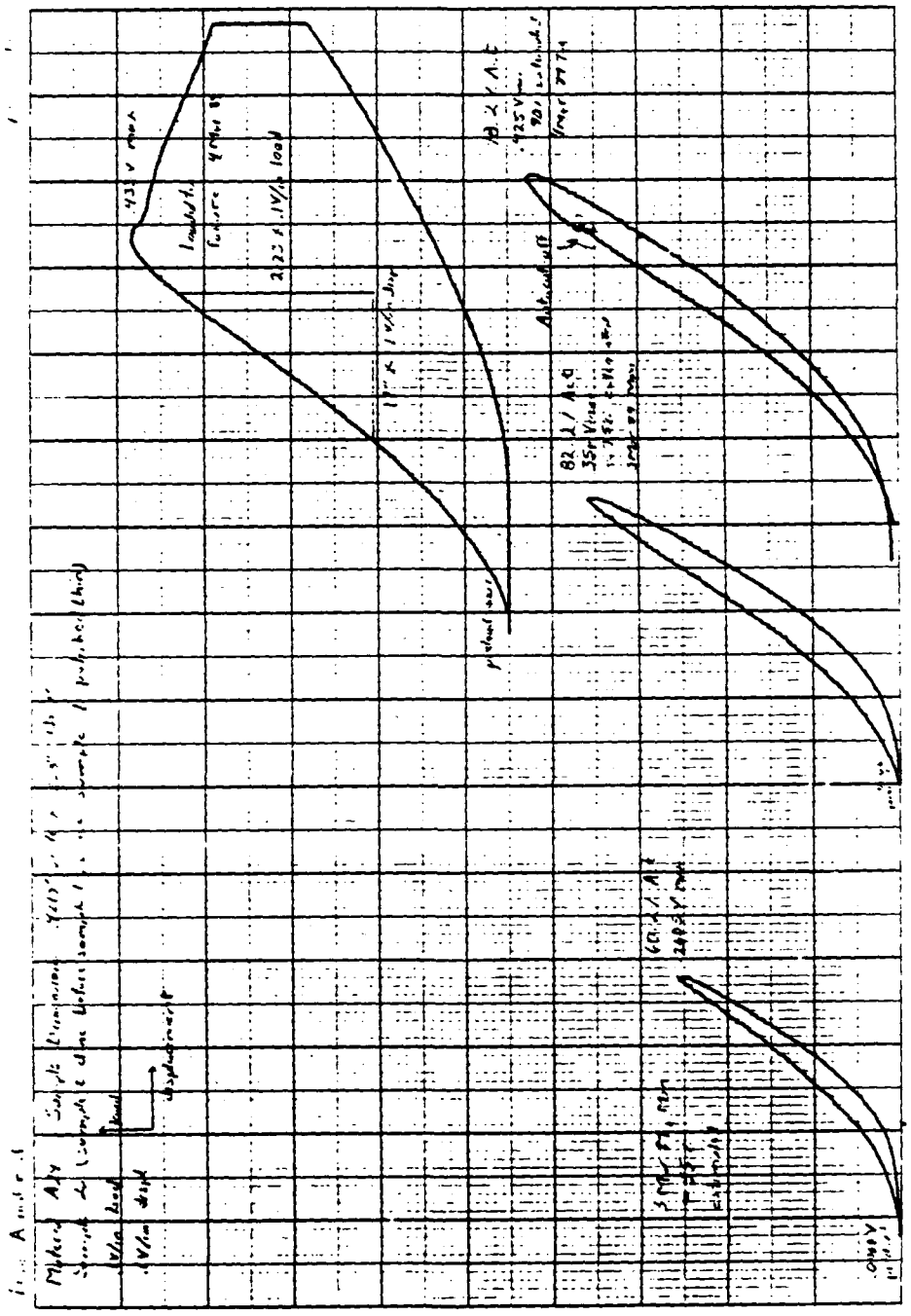

Figure 50. Specimen A24-2

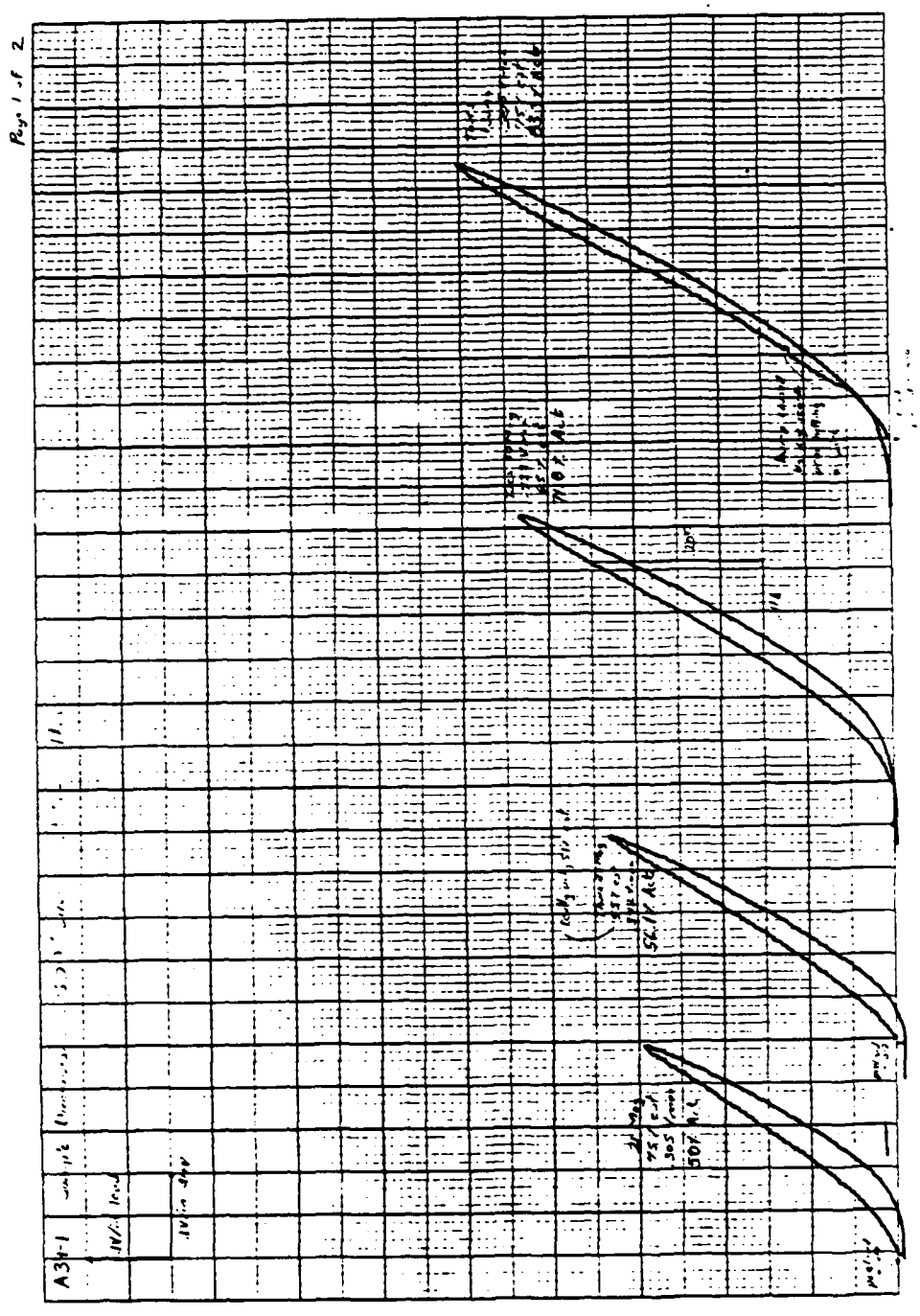

Figure 51. Specimen A34-1, Page 1 of 2

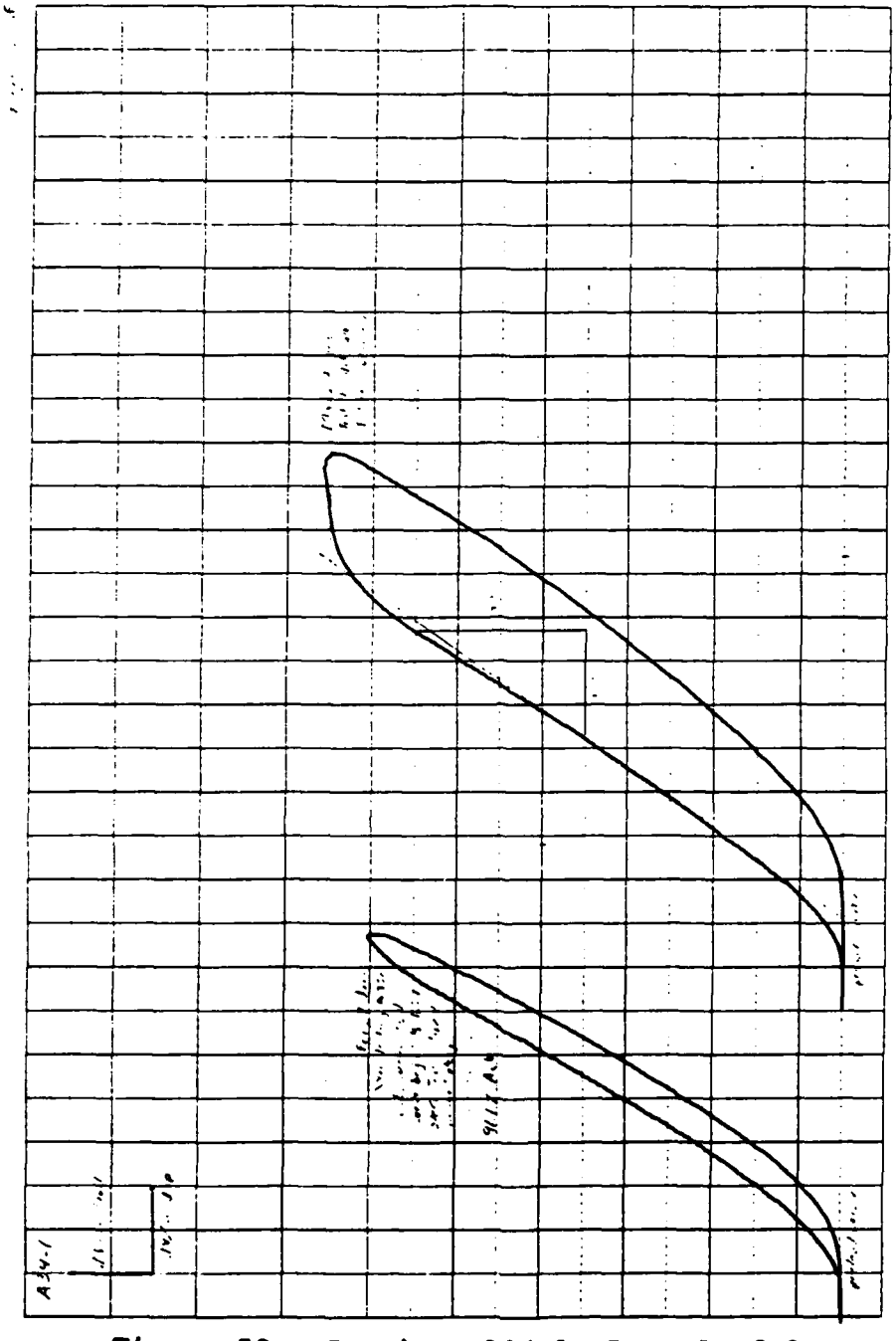

Figure 52. Specimen A34-1, Page 2 of 2

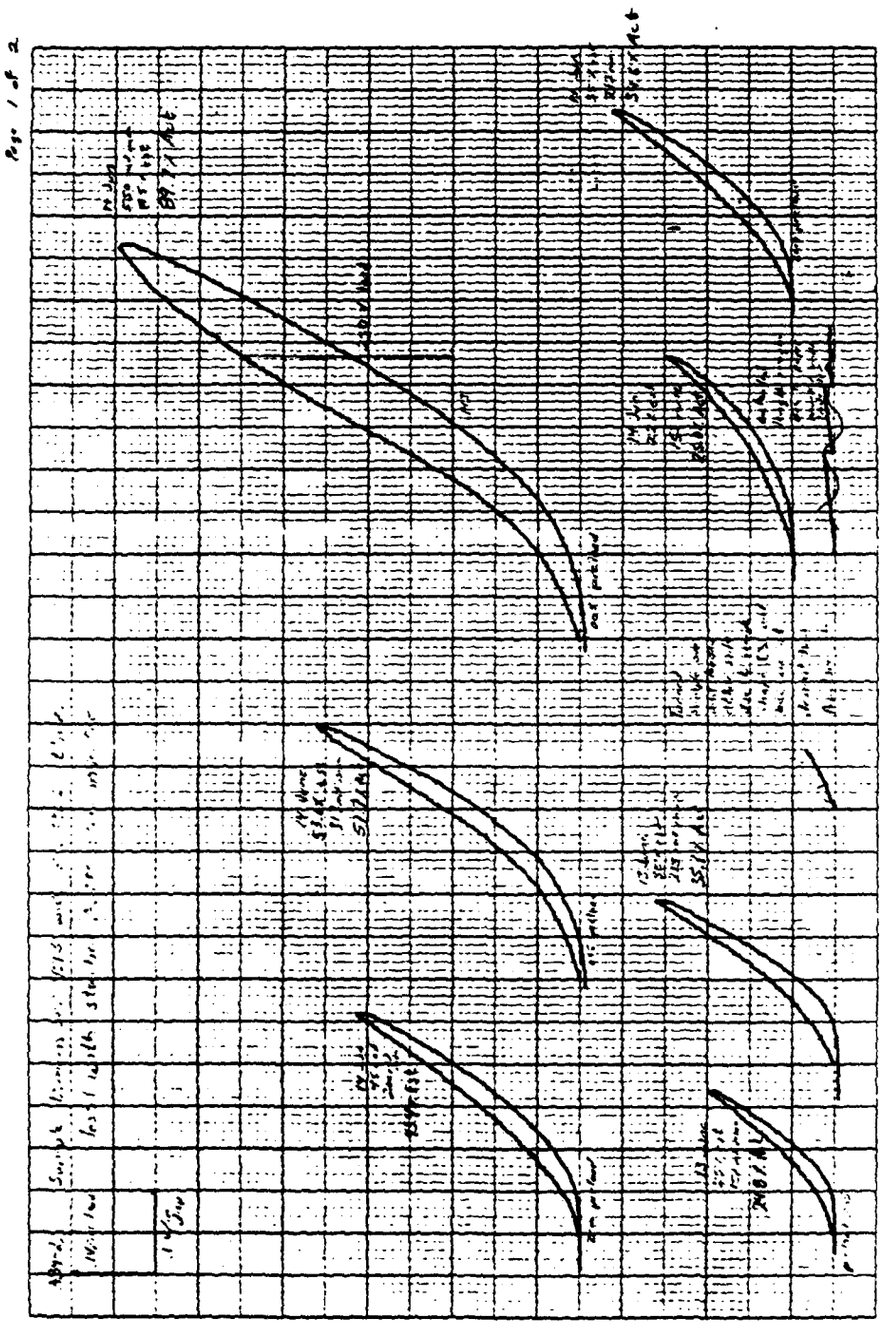

Figure 53. Specimen A34-2, Page 1 of 2

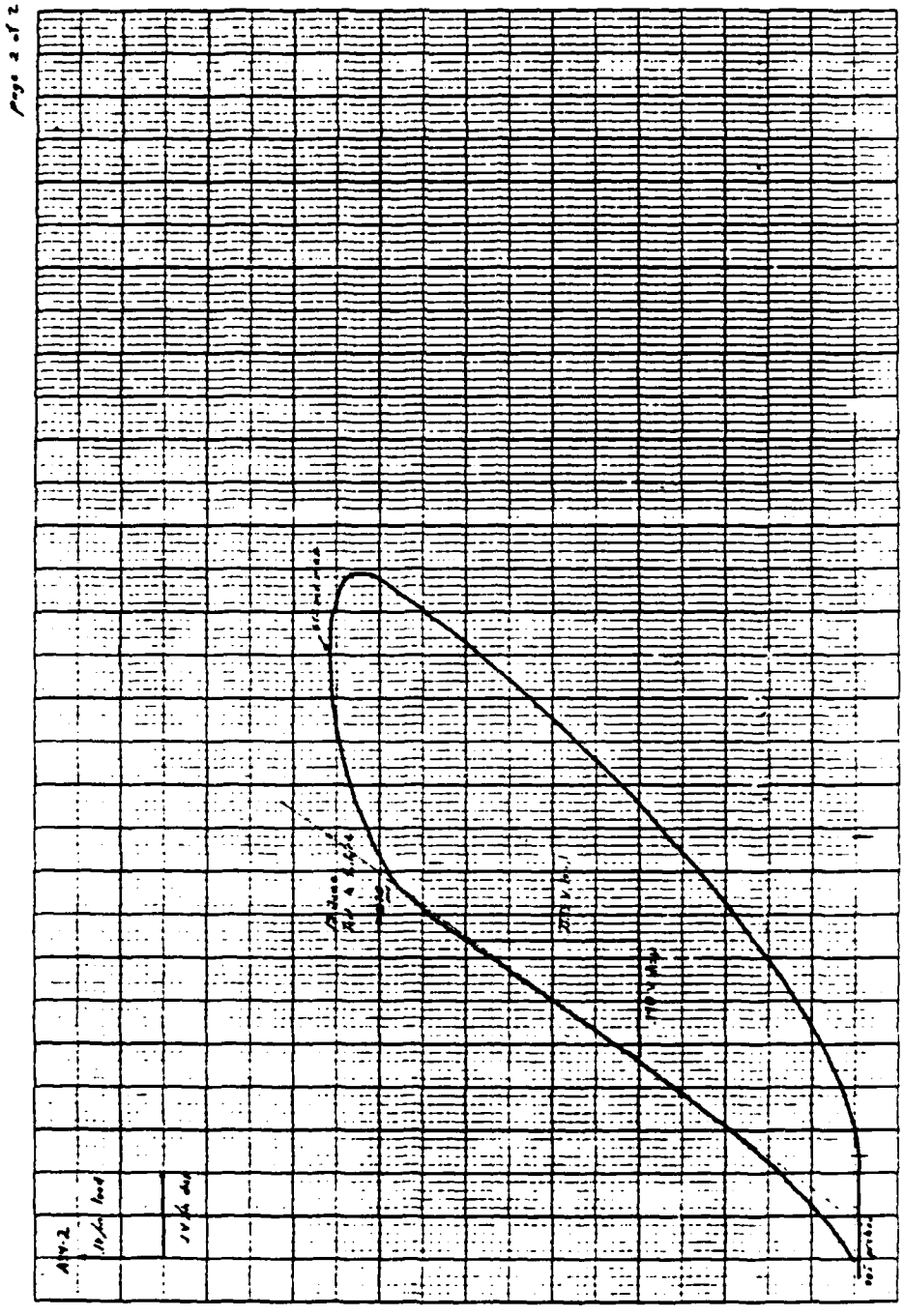

Figure 54. Specimen A34-2, Page 2 of 2

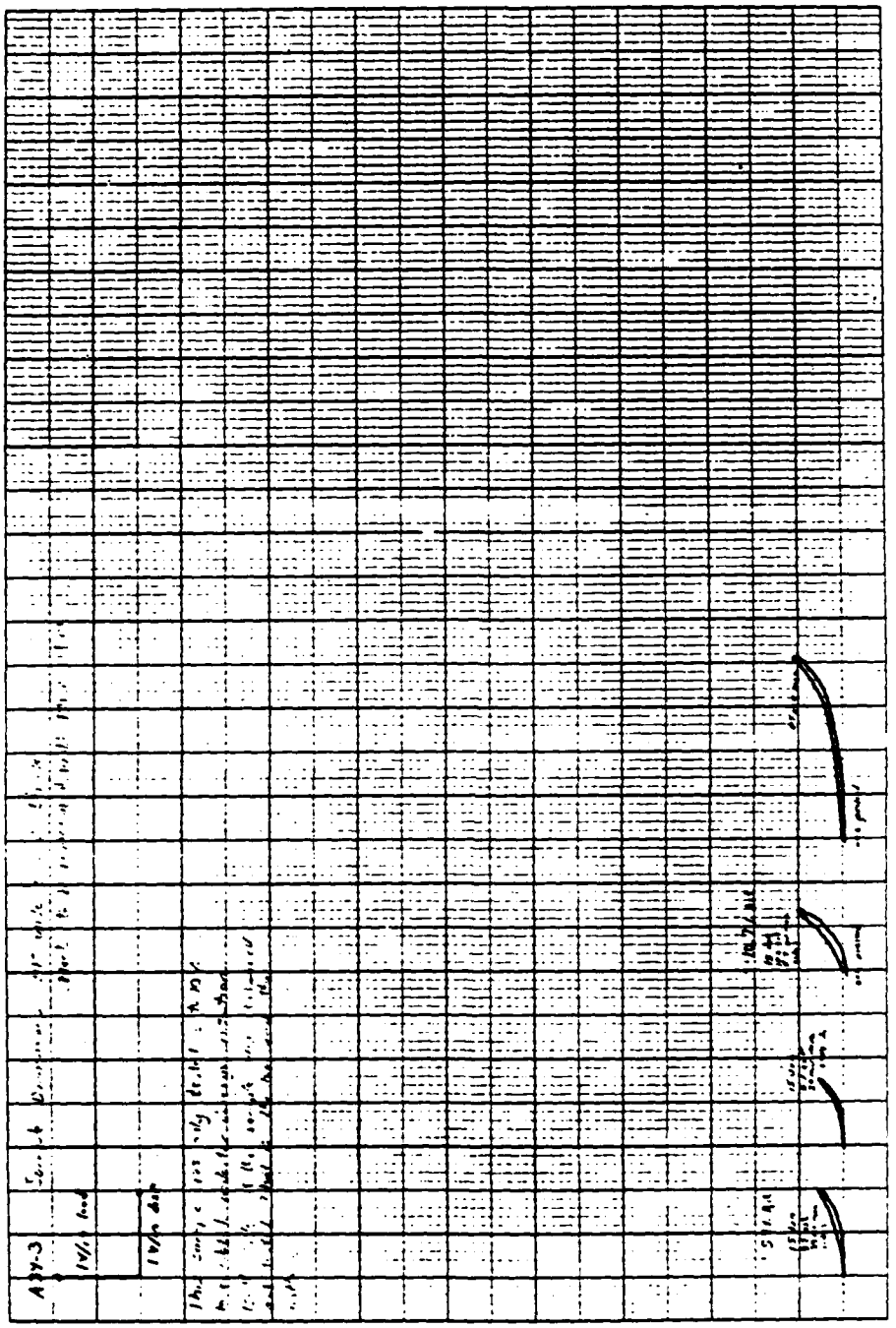

Figure 55. Specimen A34-3, Page 1 of 2

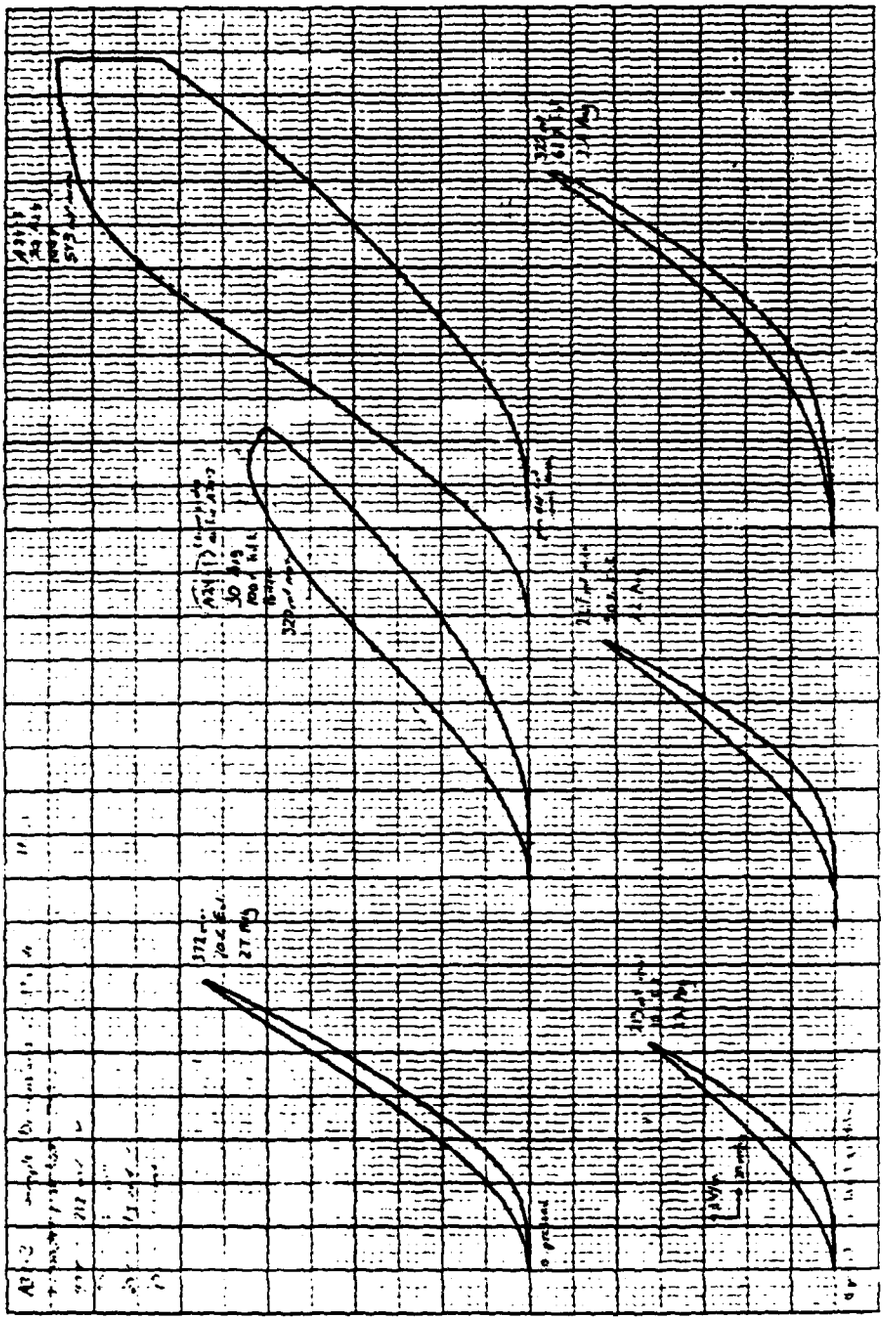

Figure 56. Specimen A34-3, Page 2 of 2

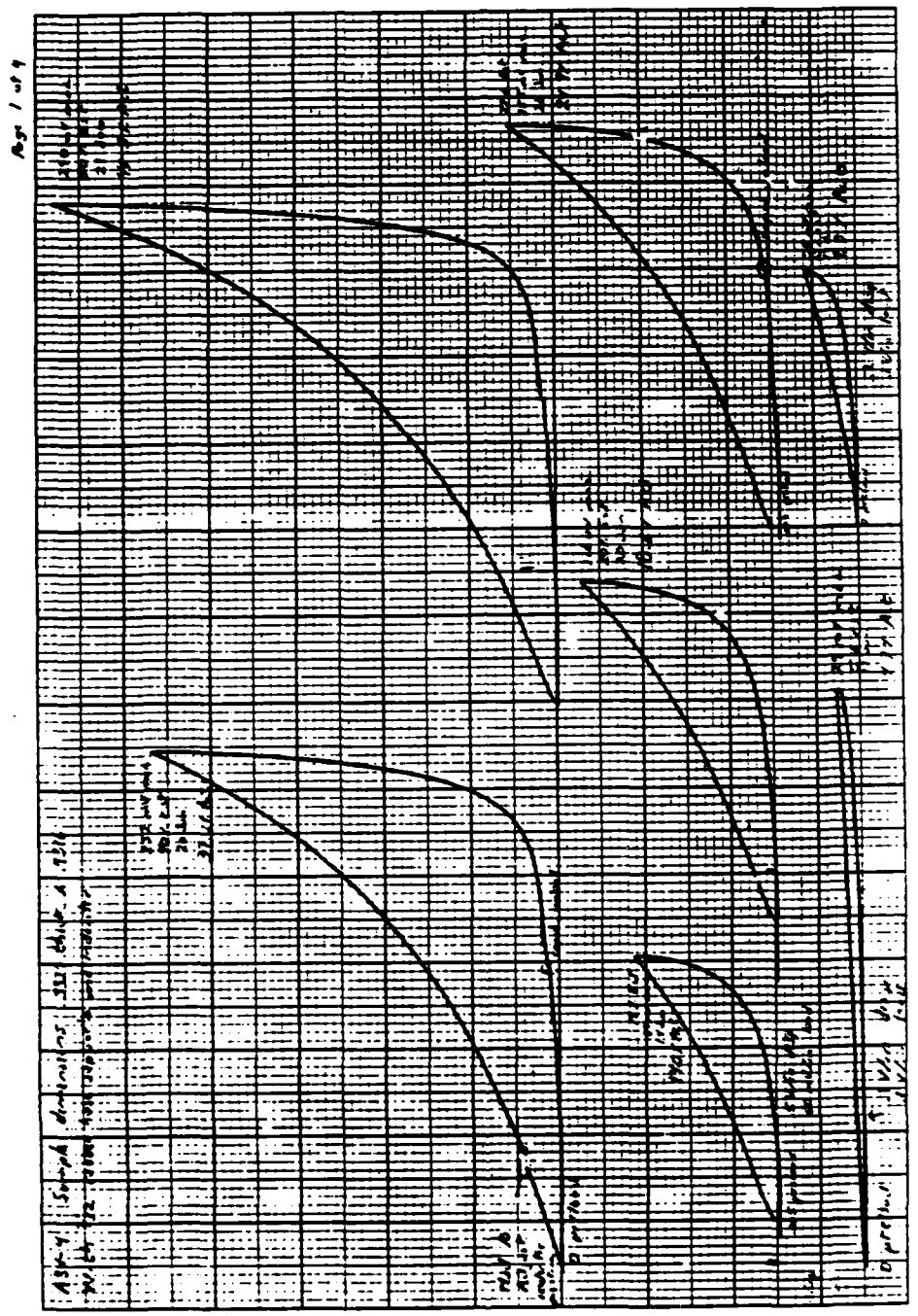

Figure 57. Specimen A34-4, Page 1 of 4

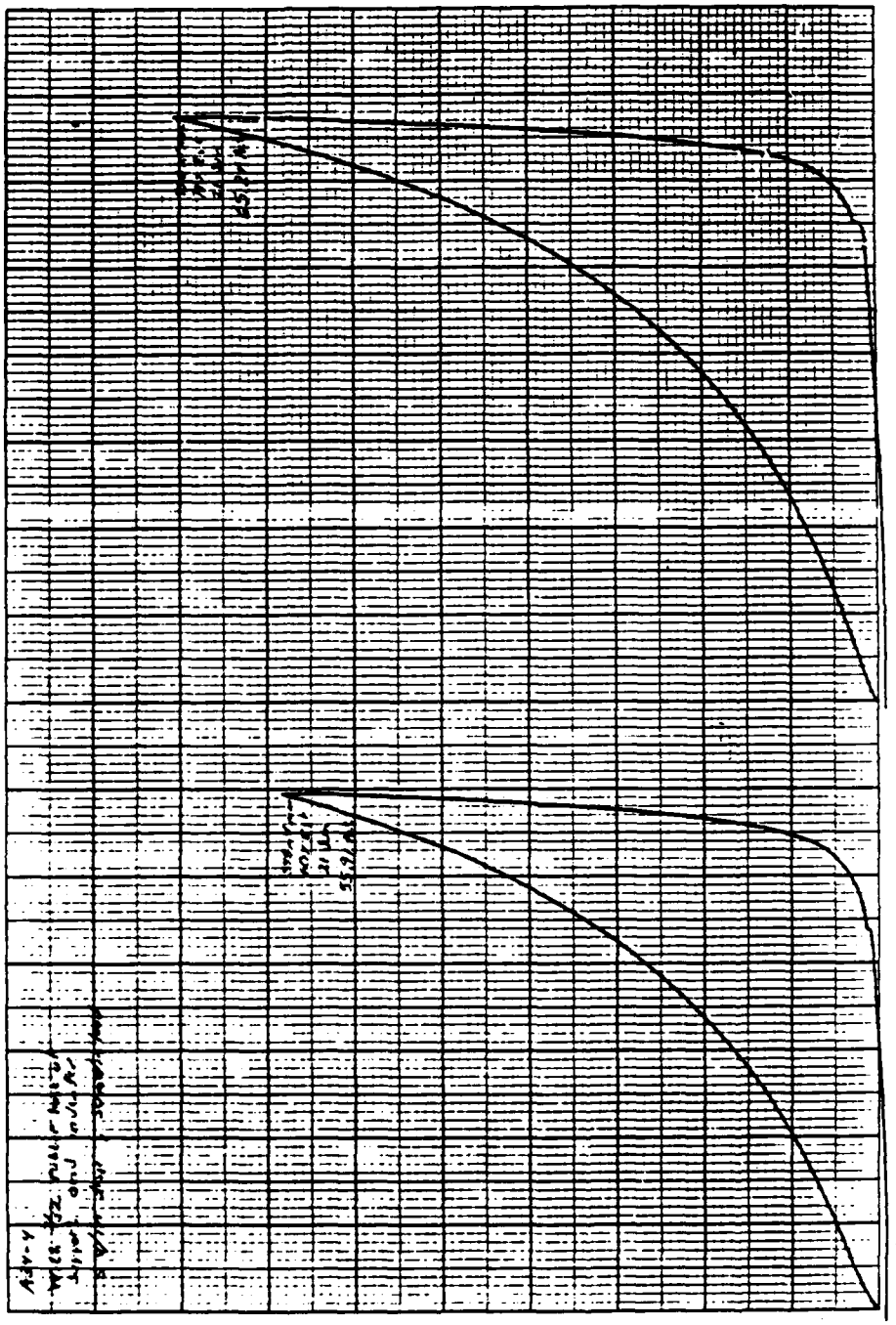

Figure 58. Specimen A34-4, Page 2 of 4

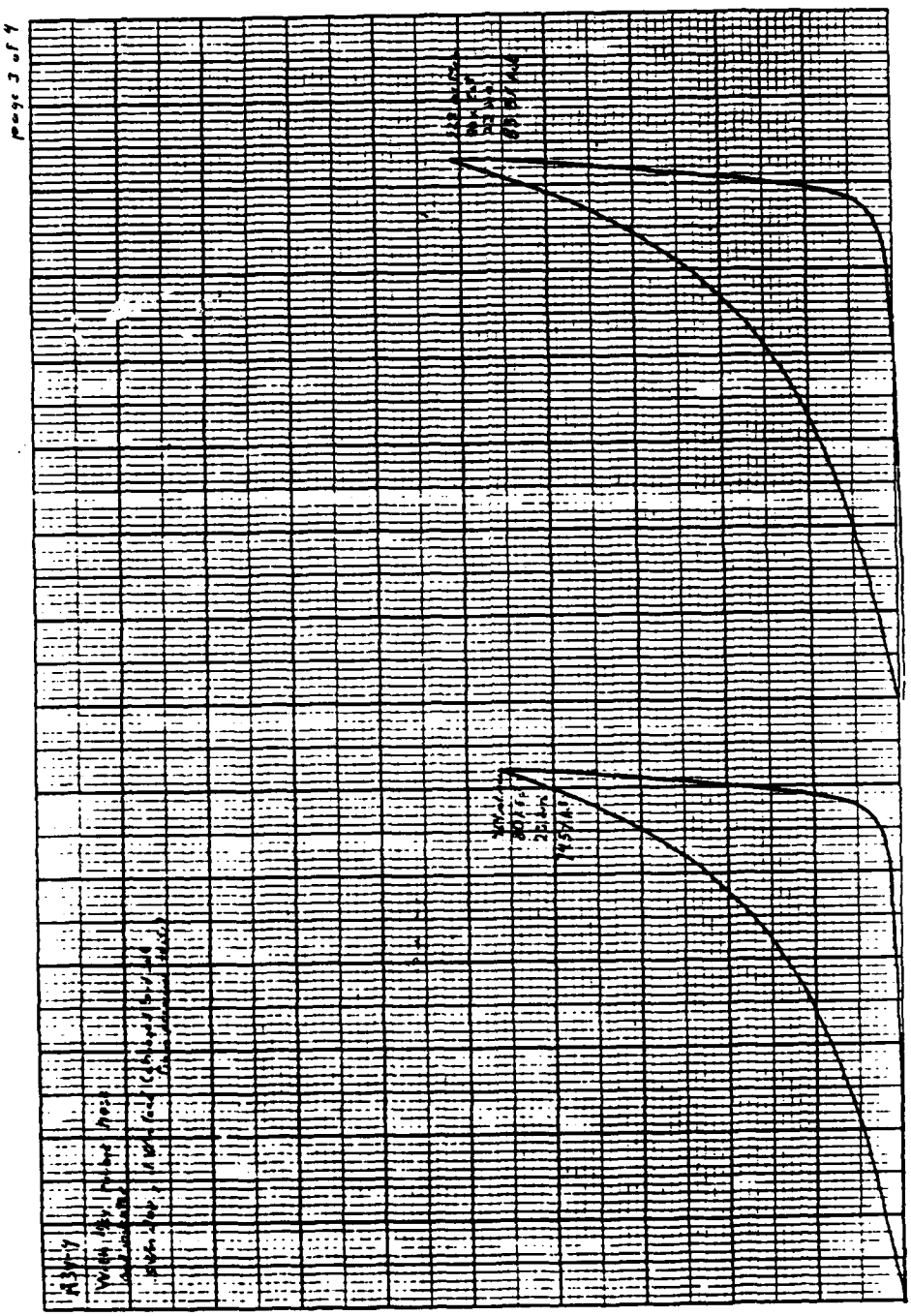

Figure 59. Specimen A34-4, Page 3 of 4

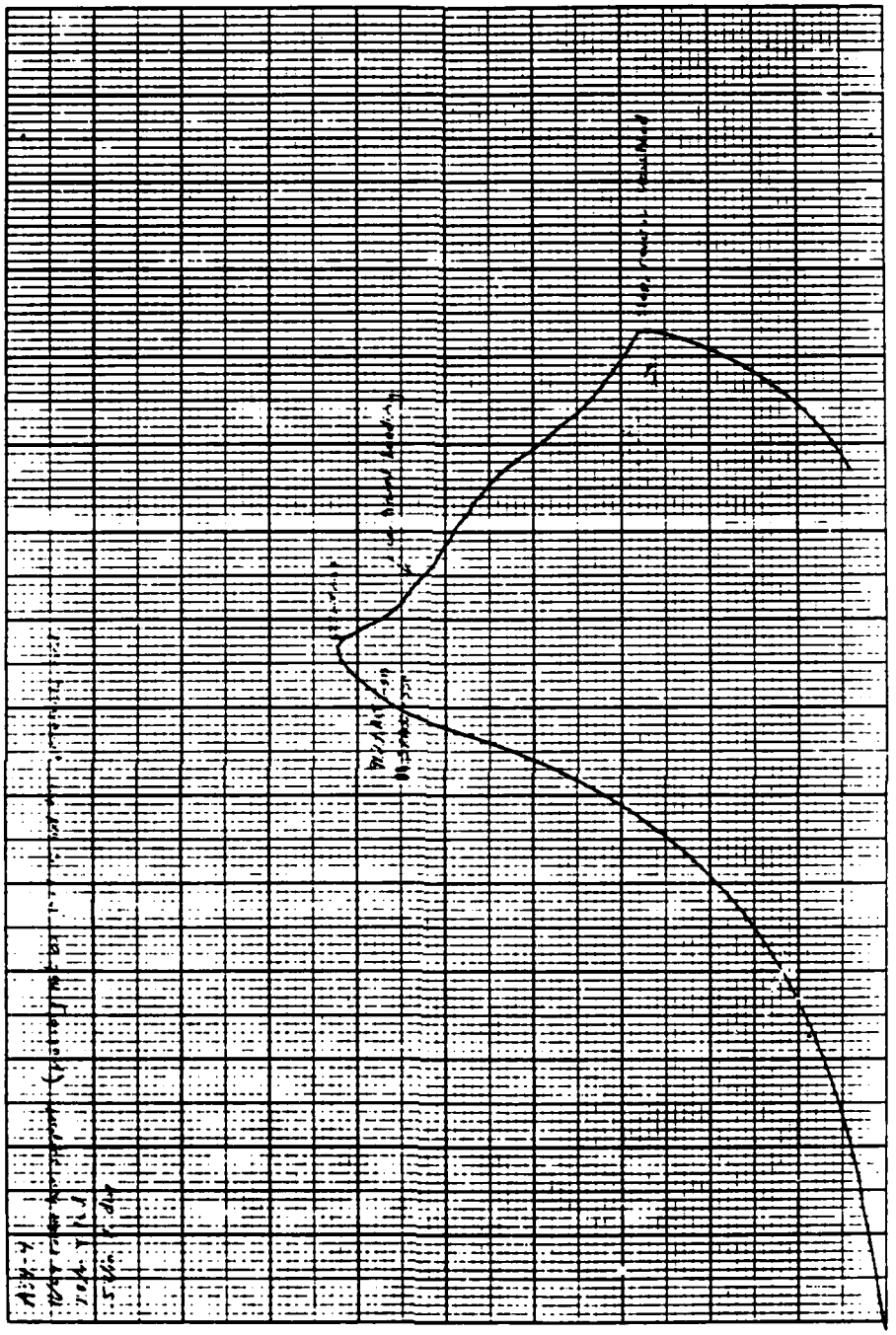

Figure 60. Specimen A34-4, Page 4 of 4

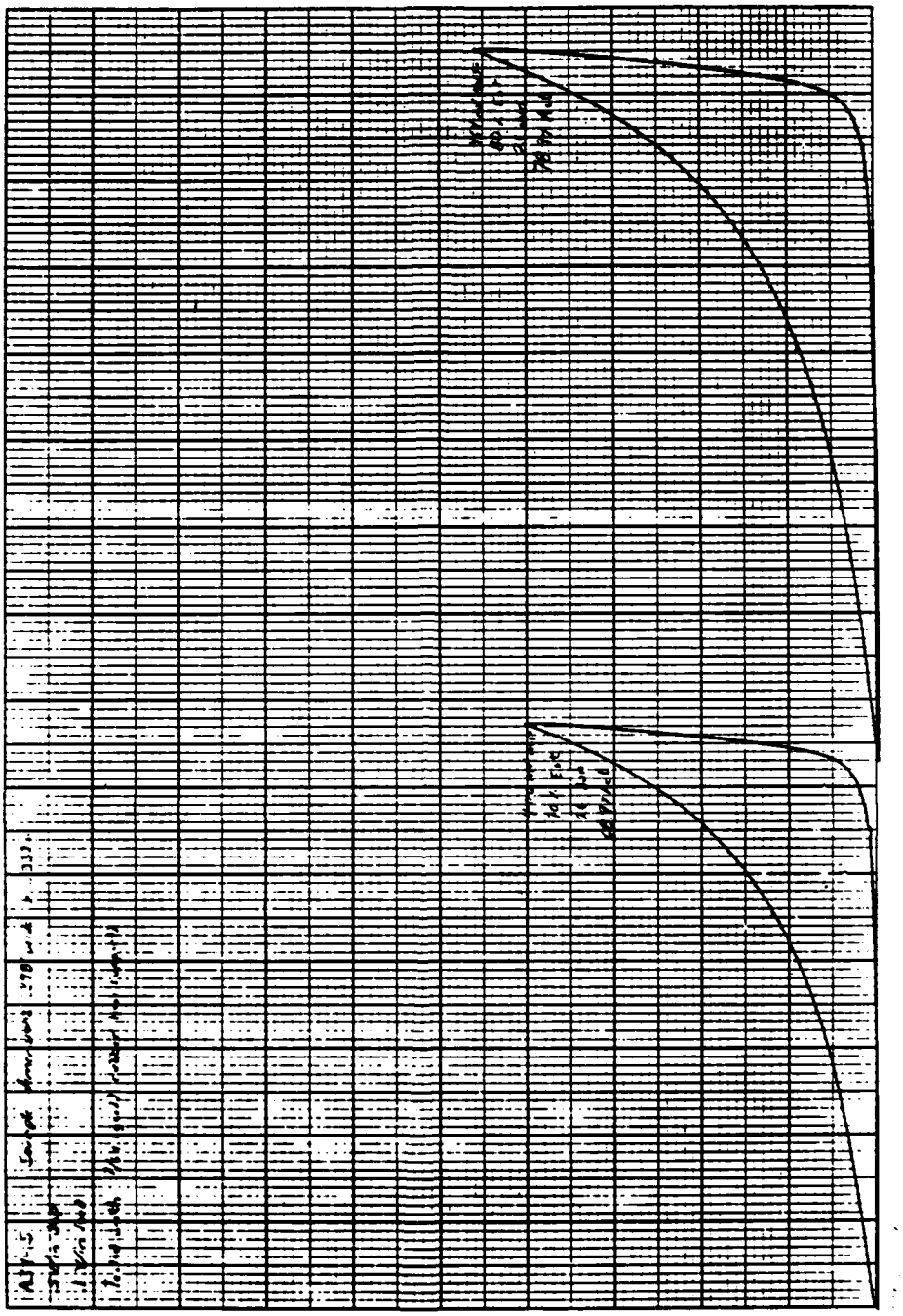

Figure 61. Specimen A34-5, Page 1 of 2

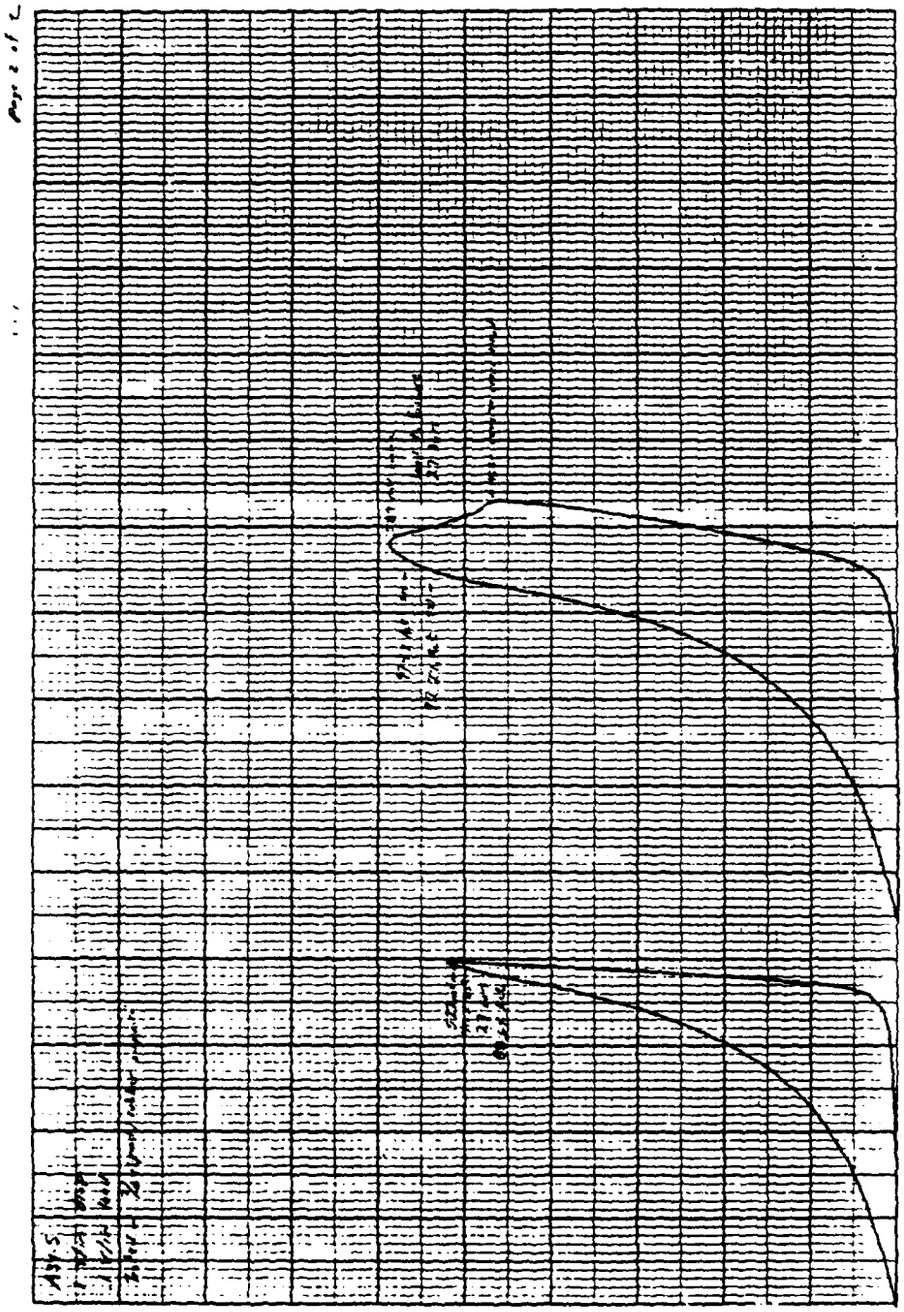

Figure 62. Specimen A34-5, Page 2 of 2

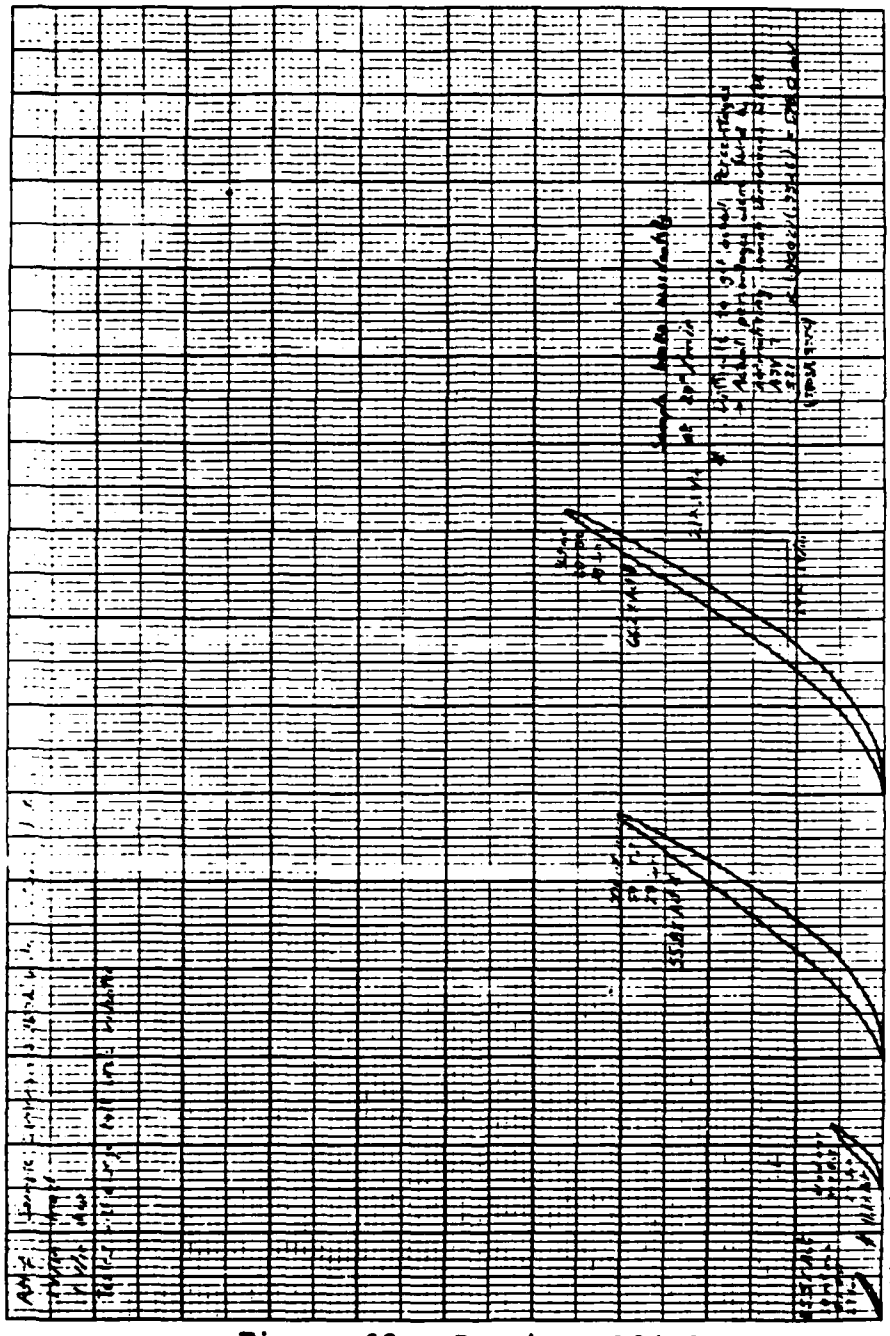

Figure 63. Specimen A34-6

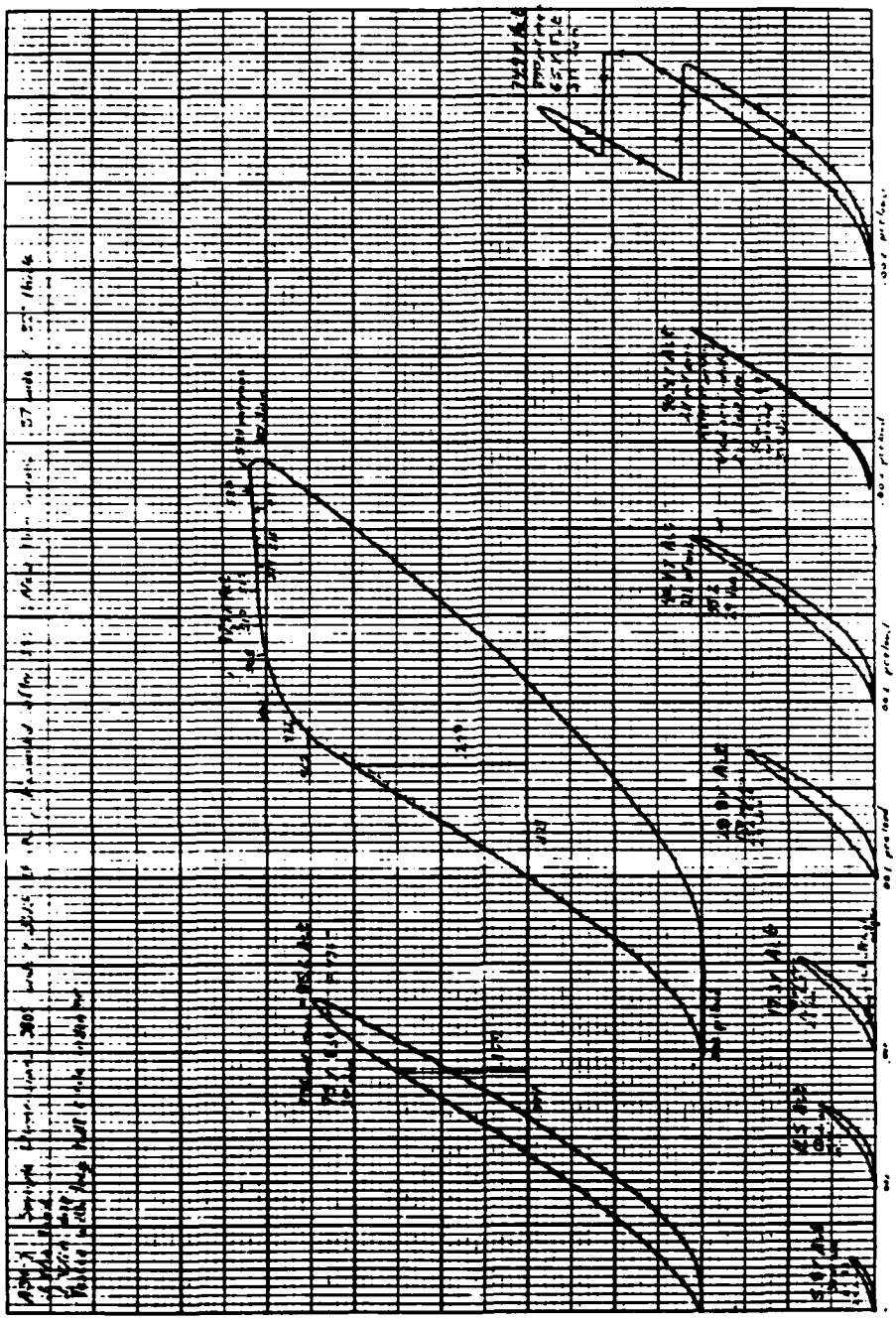

Figure 64. Specimen A34-7, Page 1 of 2

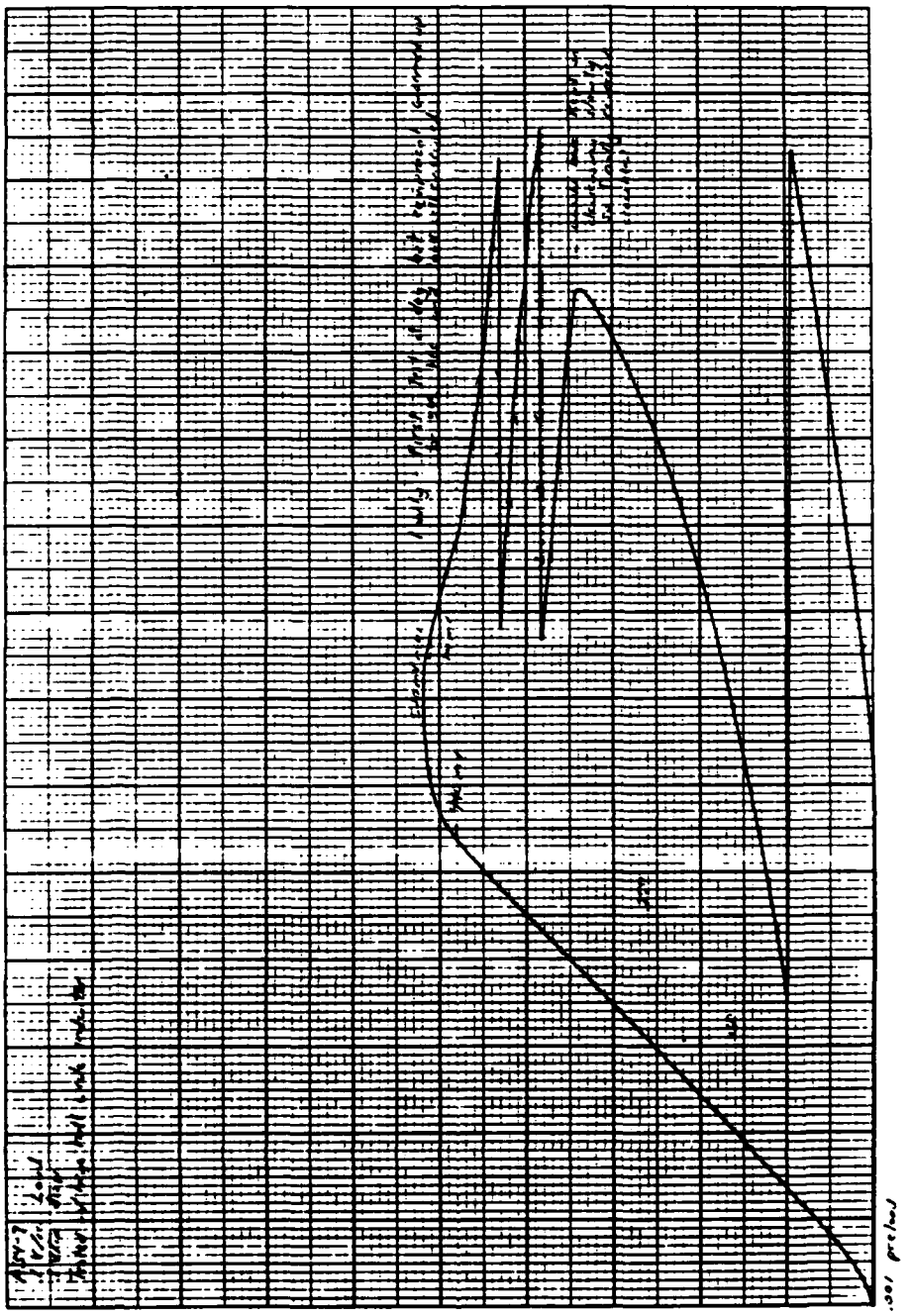

Figure 65. Specimen A34-7, Page 2 of 2

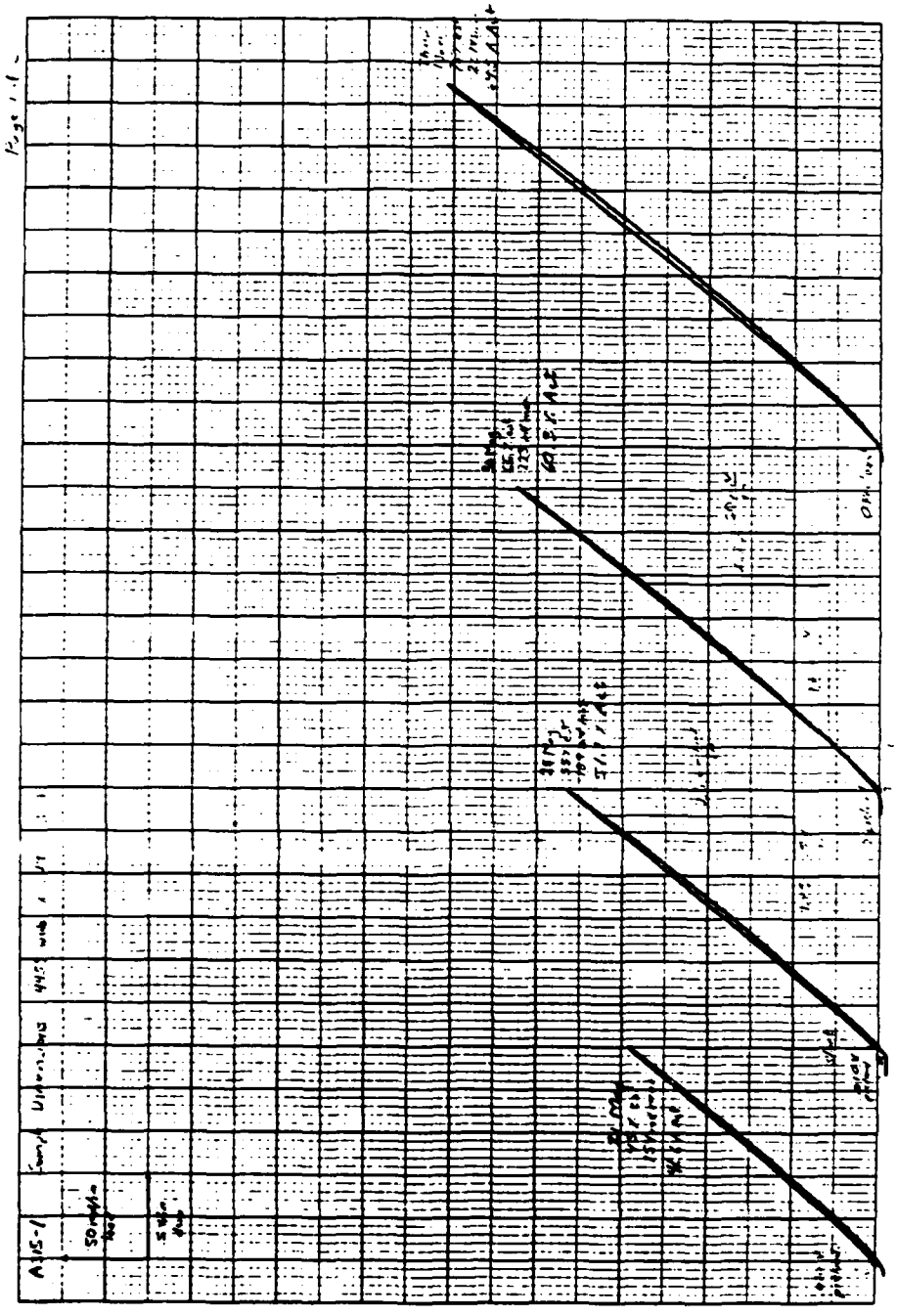

Figure 66. Specimen A315-1, Page 1 of 3

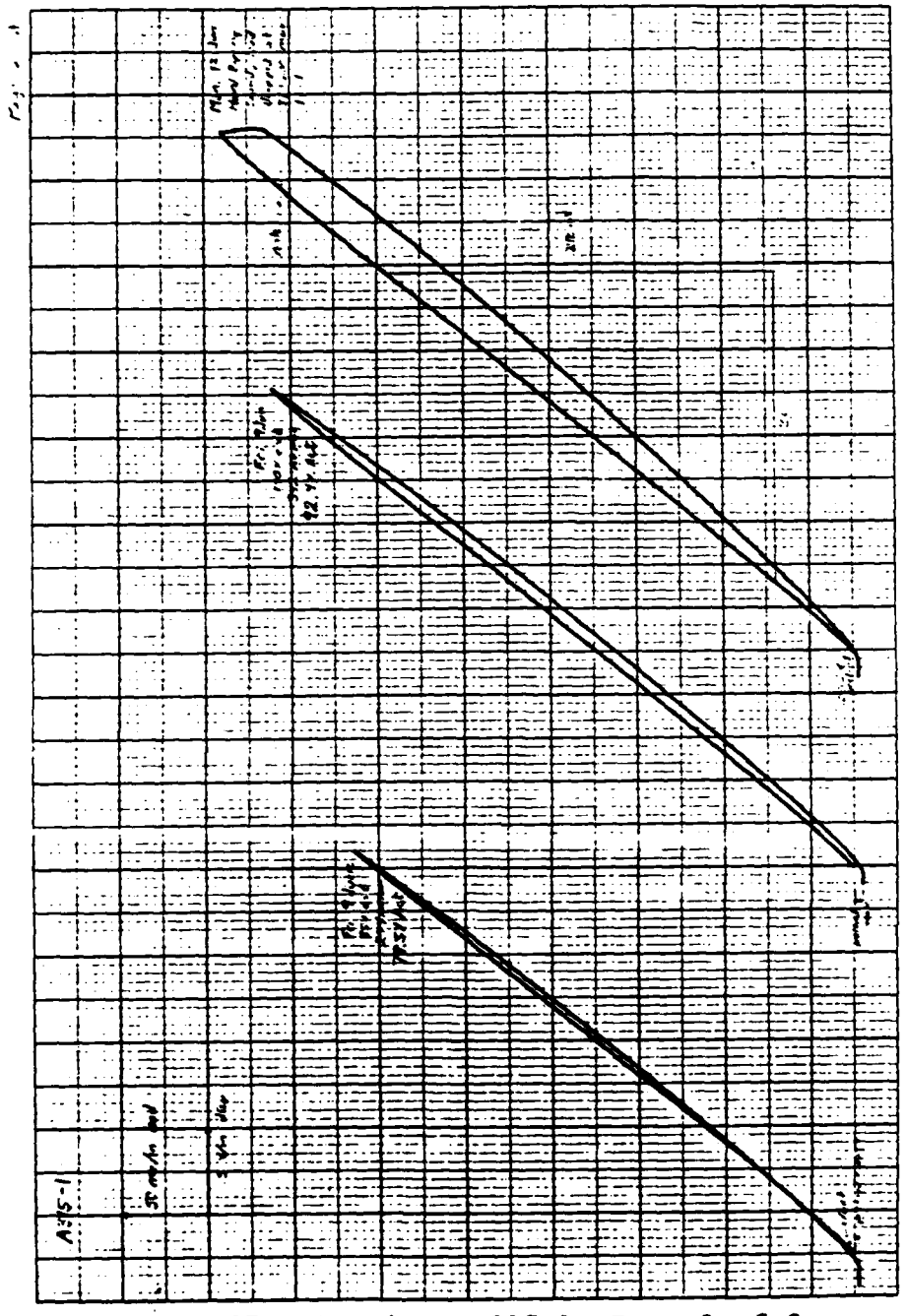

Figure 67. Specimen A315-1, Page 2 of 3

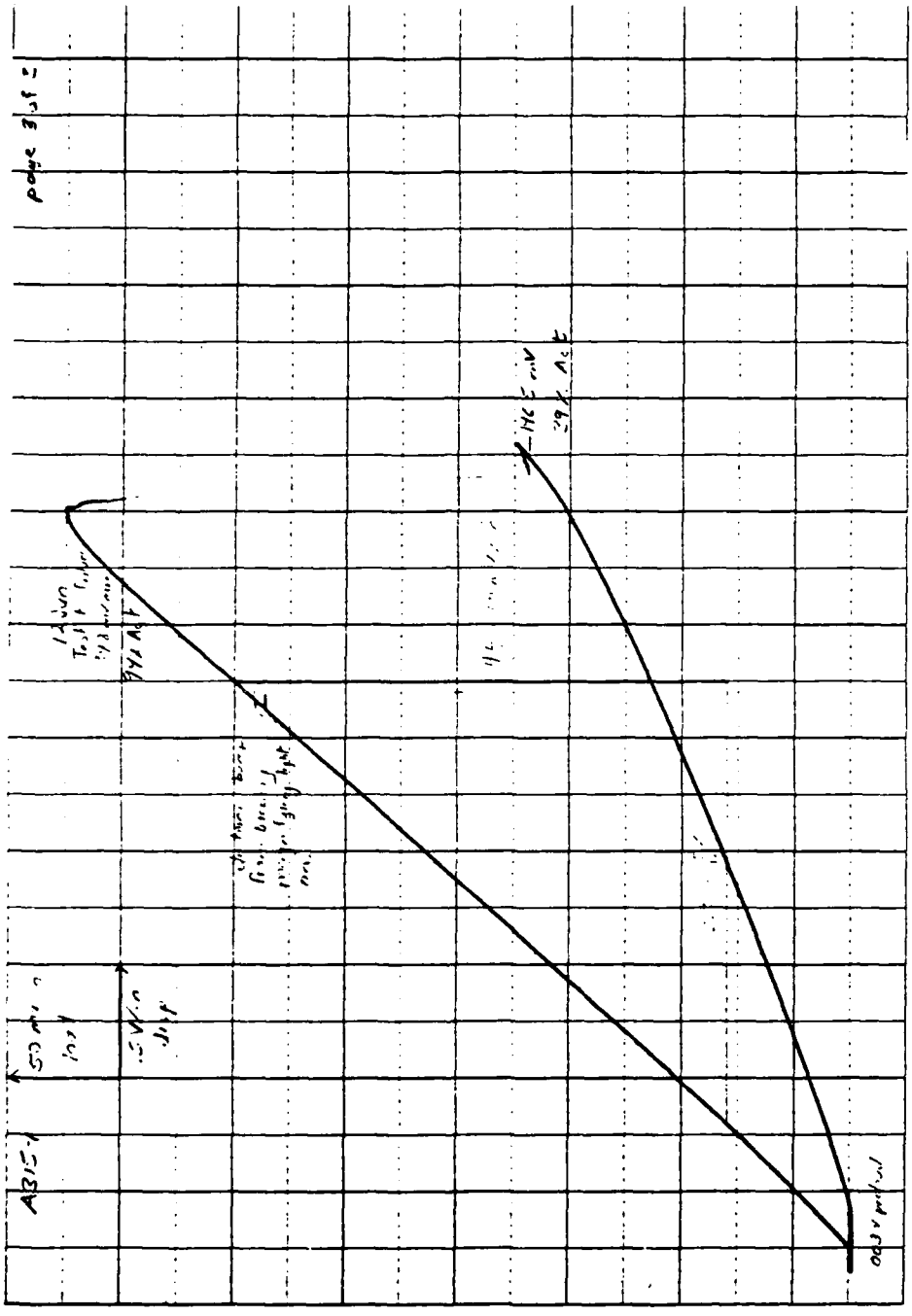

Figure 68. Specimen A315-1, Page 3 of 3

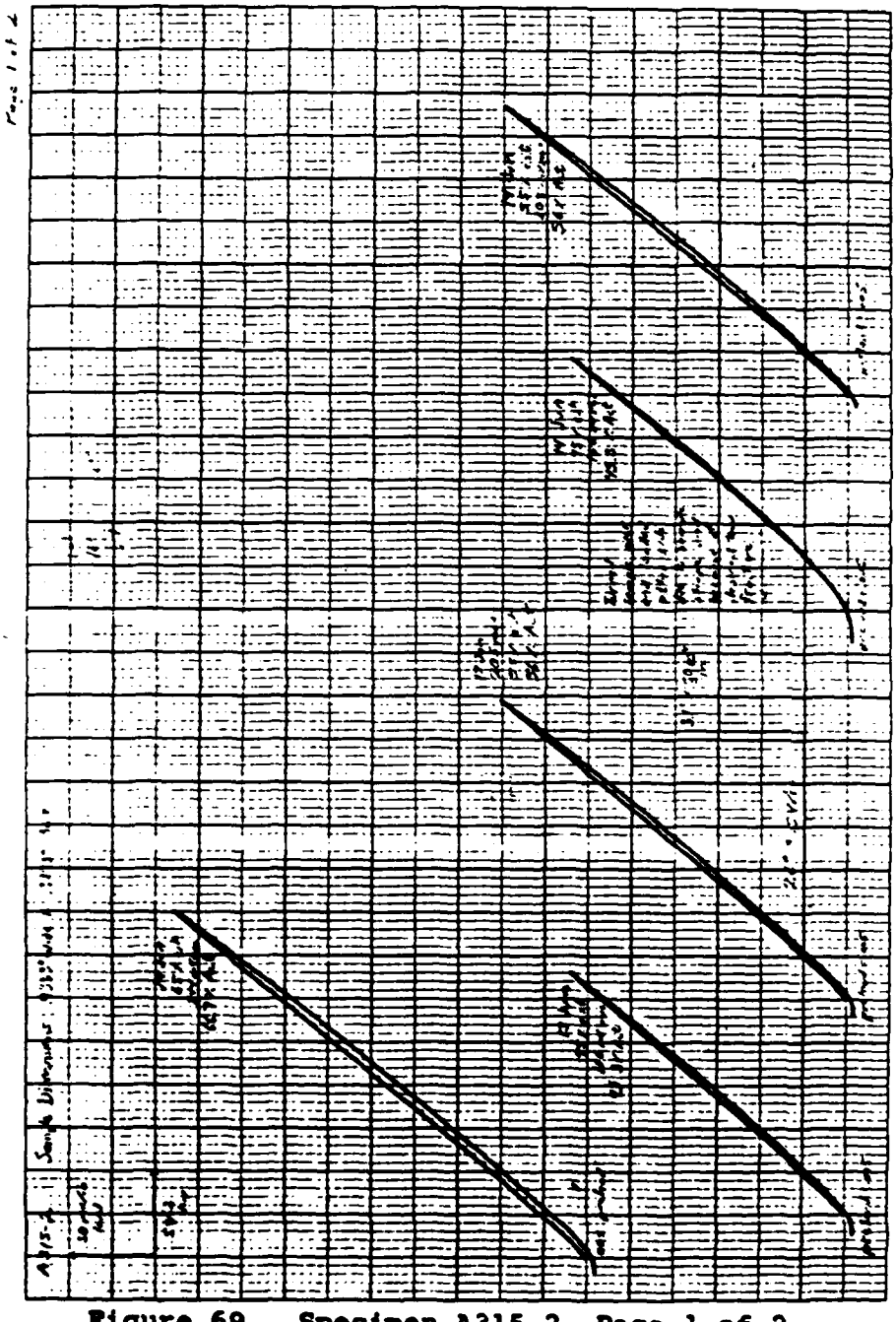

Figure 69. Specimen A315-2, Page 1 of 2

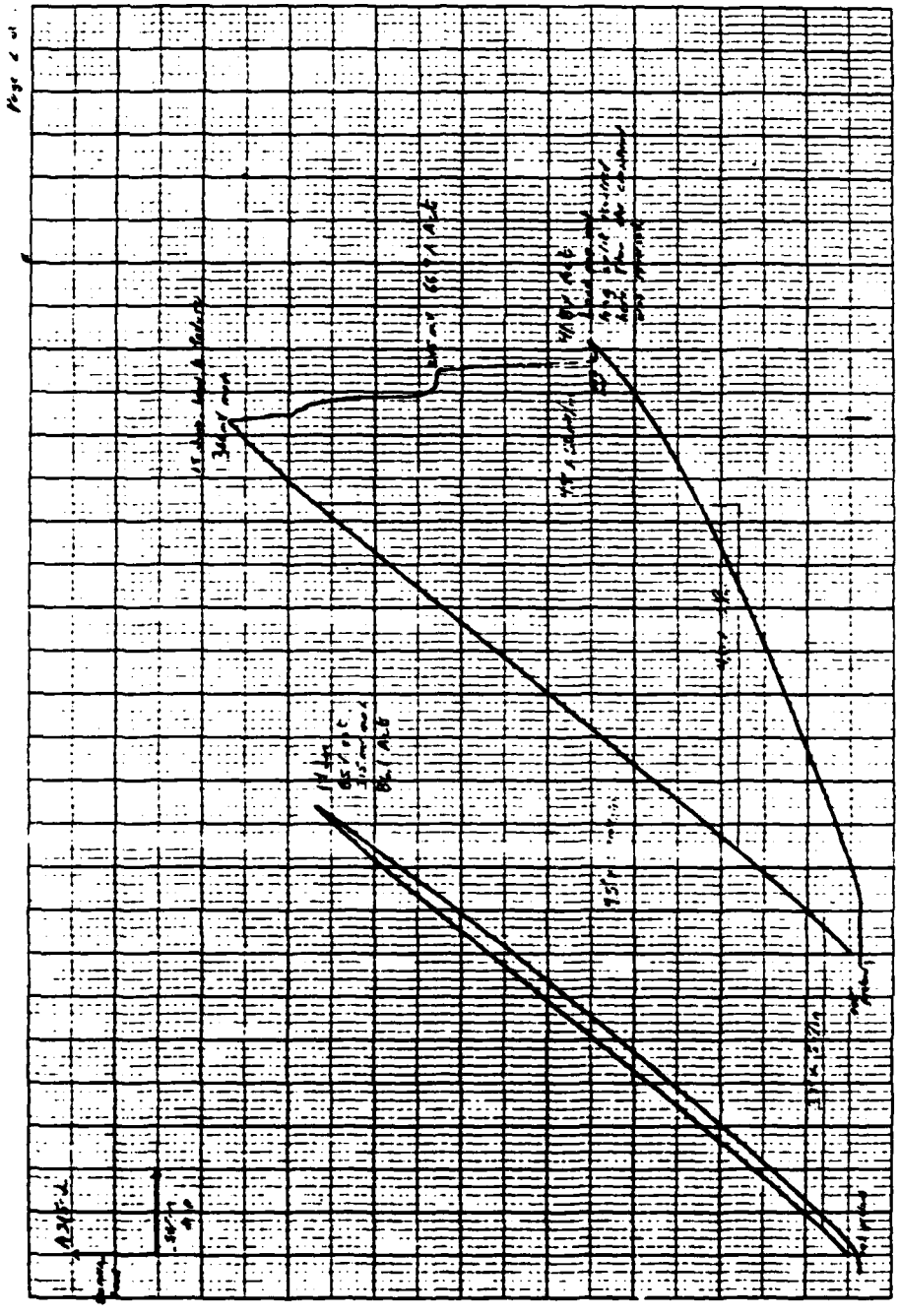

Figure 70. Specimen A315-2, Page 2 of 2

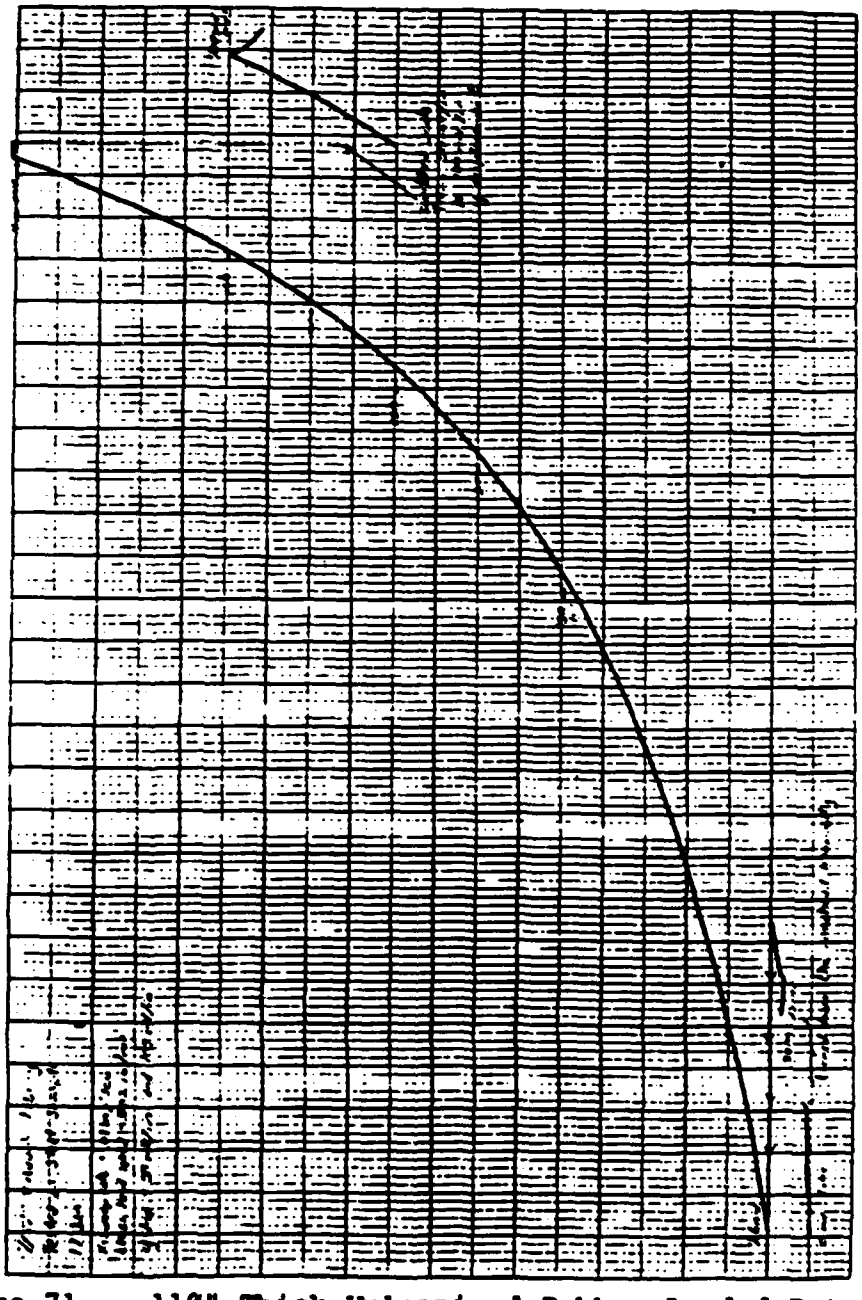

Figure 71. .110" Thick Vulcanized Rubber Loaded Between .25" Indenter and Steel Beam

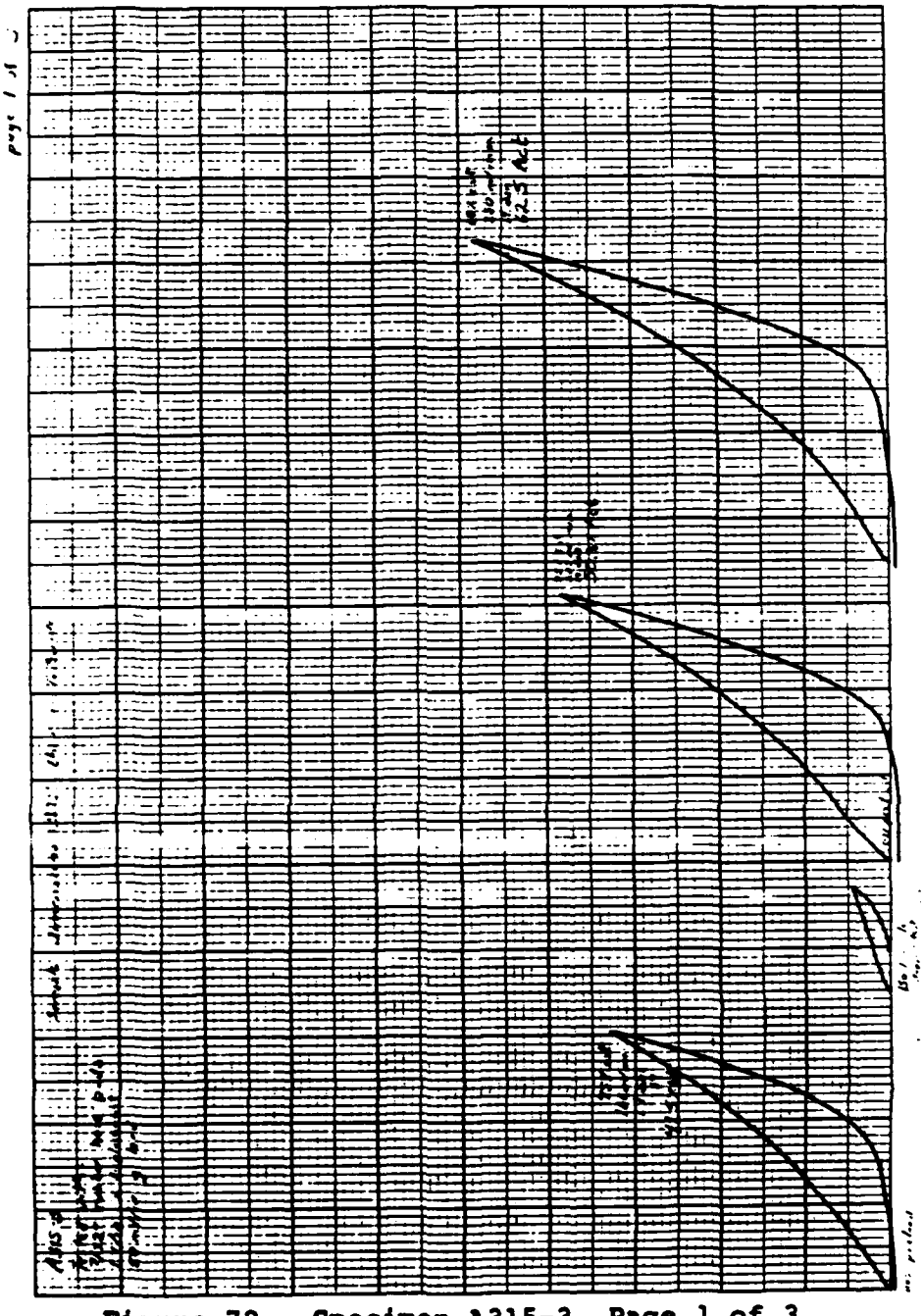

Figure 72. Specimen A315-3, Page 1 of 3

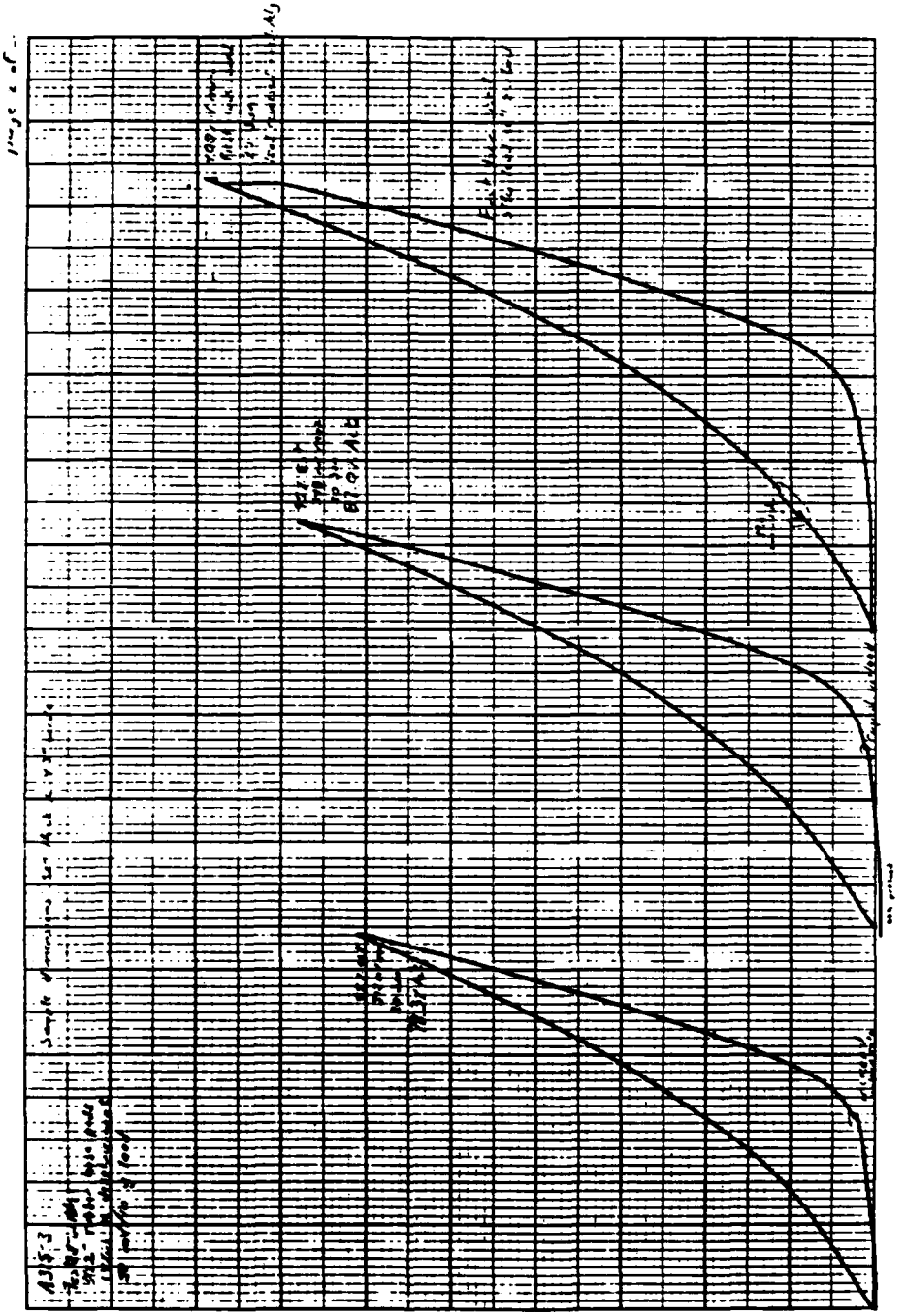

Figure 73. Specimen A315-3, Page 2 of 3

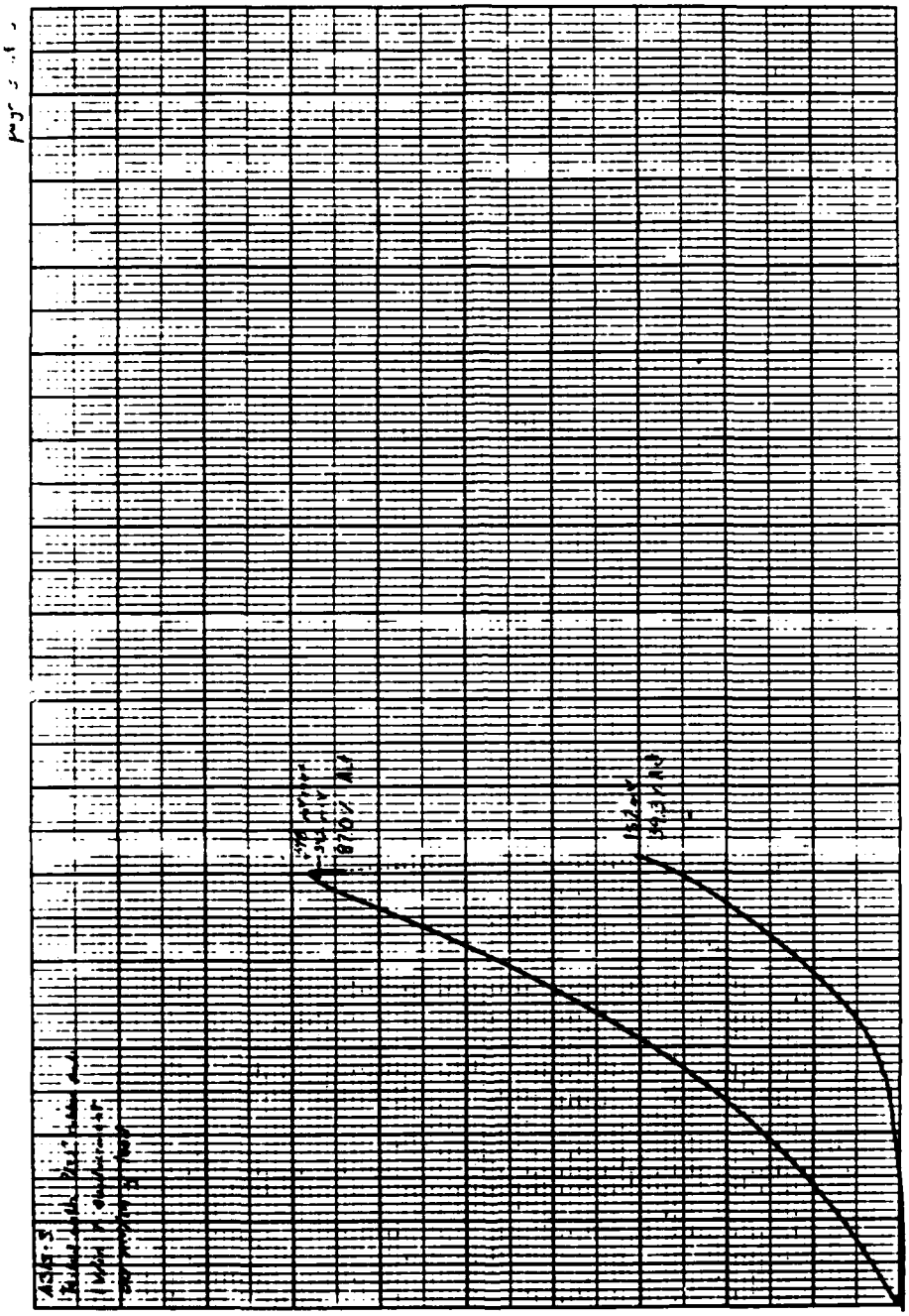

Figure 74. Specimen A315-3, Page 3 of 3

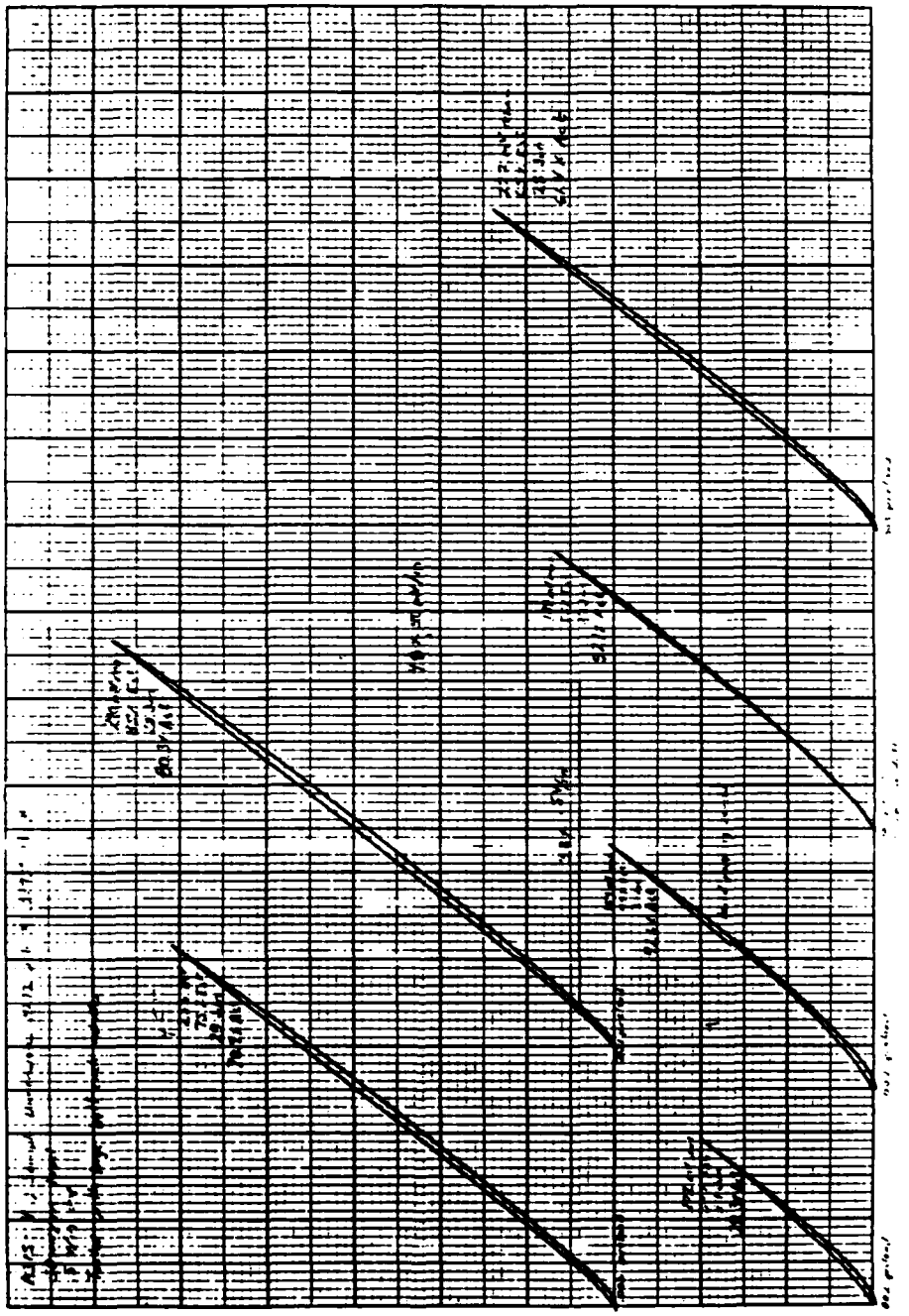

Figure 75. Specimen A315-4, Page 1 of 2

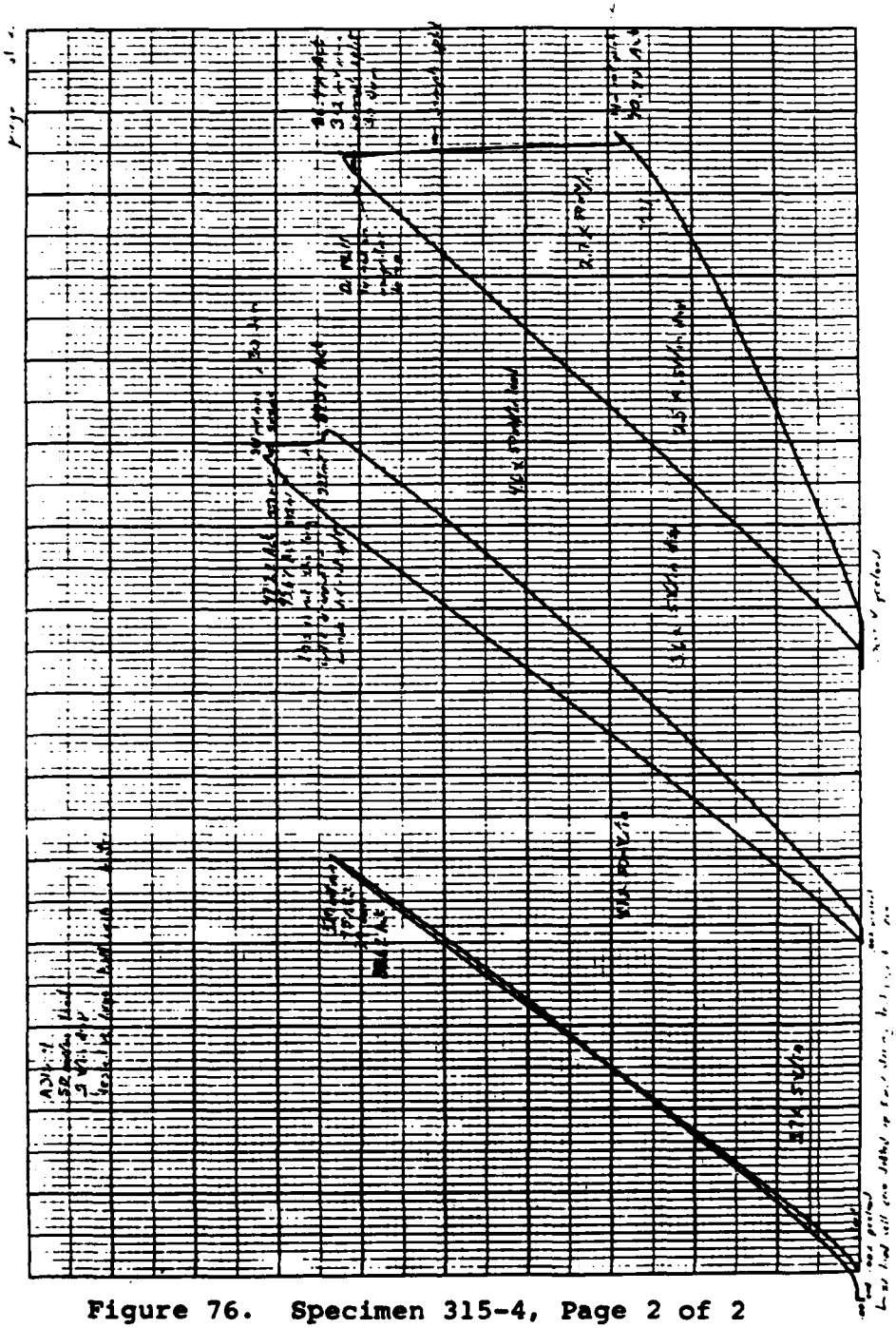

Figure 76. Specimen 315-4, Page 2 of 2

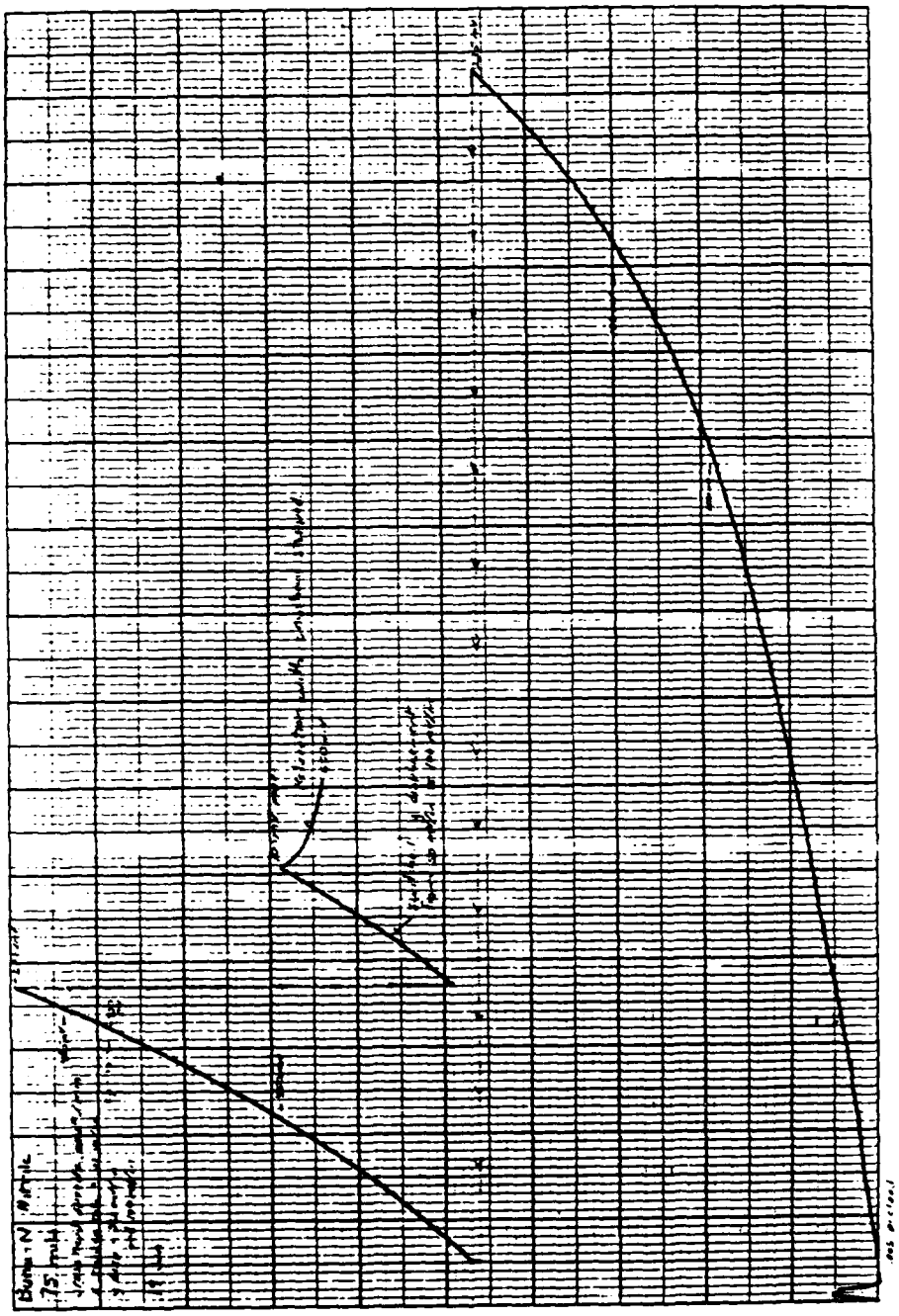

Figure 77. .075" Thick Buna-N Rubber Loaded Between .25" Indenter and Steel Beam

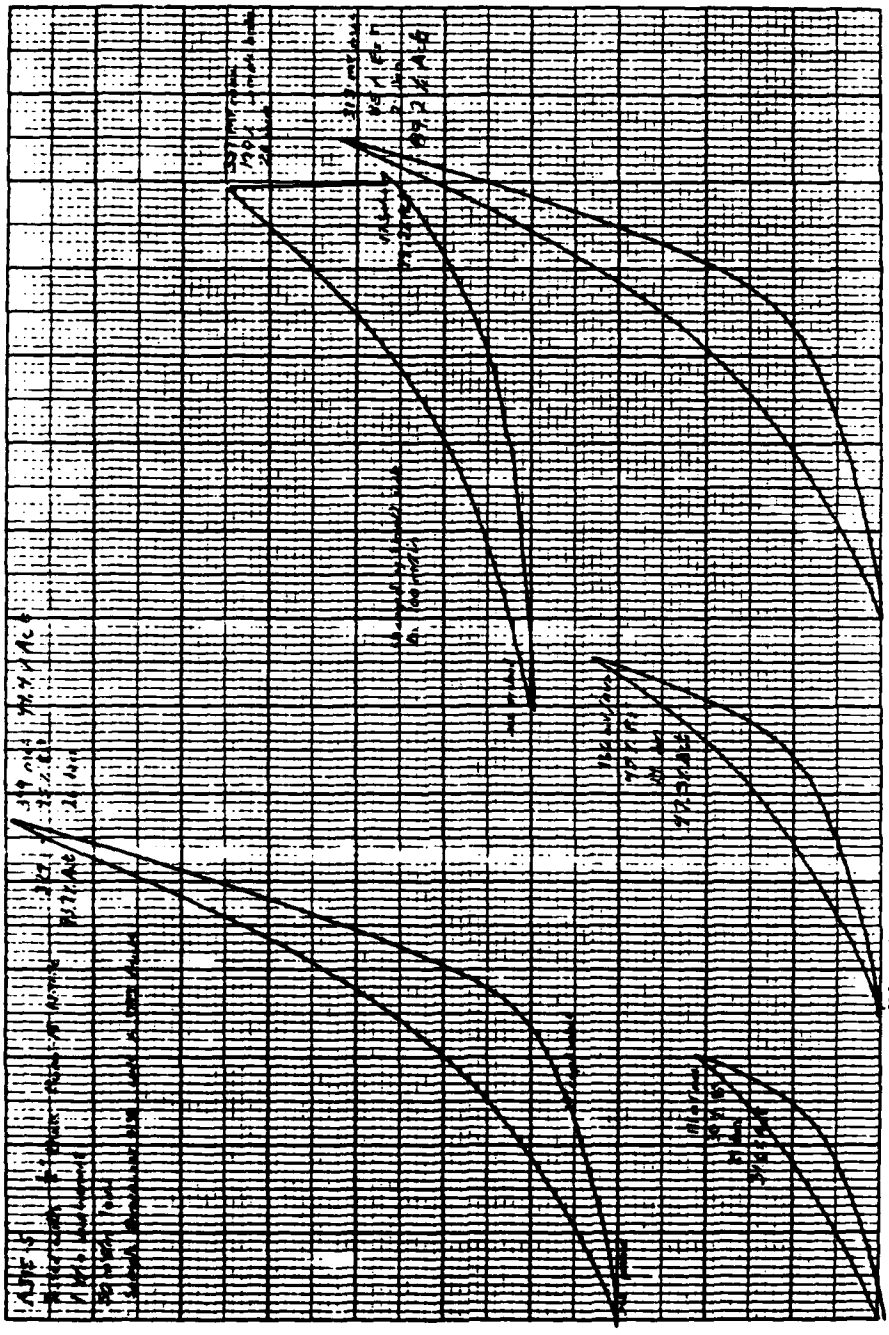

Figure 78. Specimen A315-5

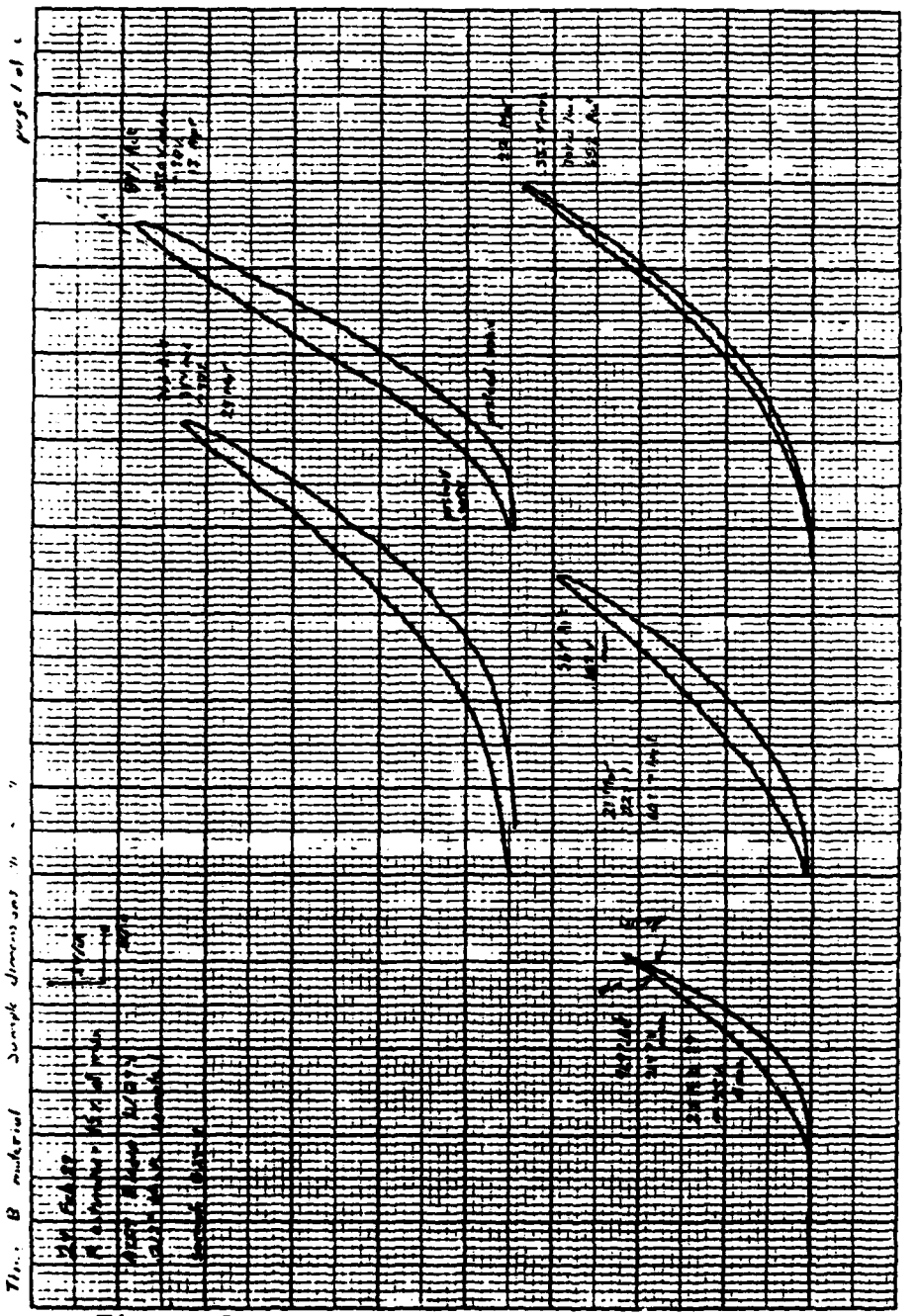

Figure 79. Specimen B24-1, Page 1 of 2

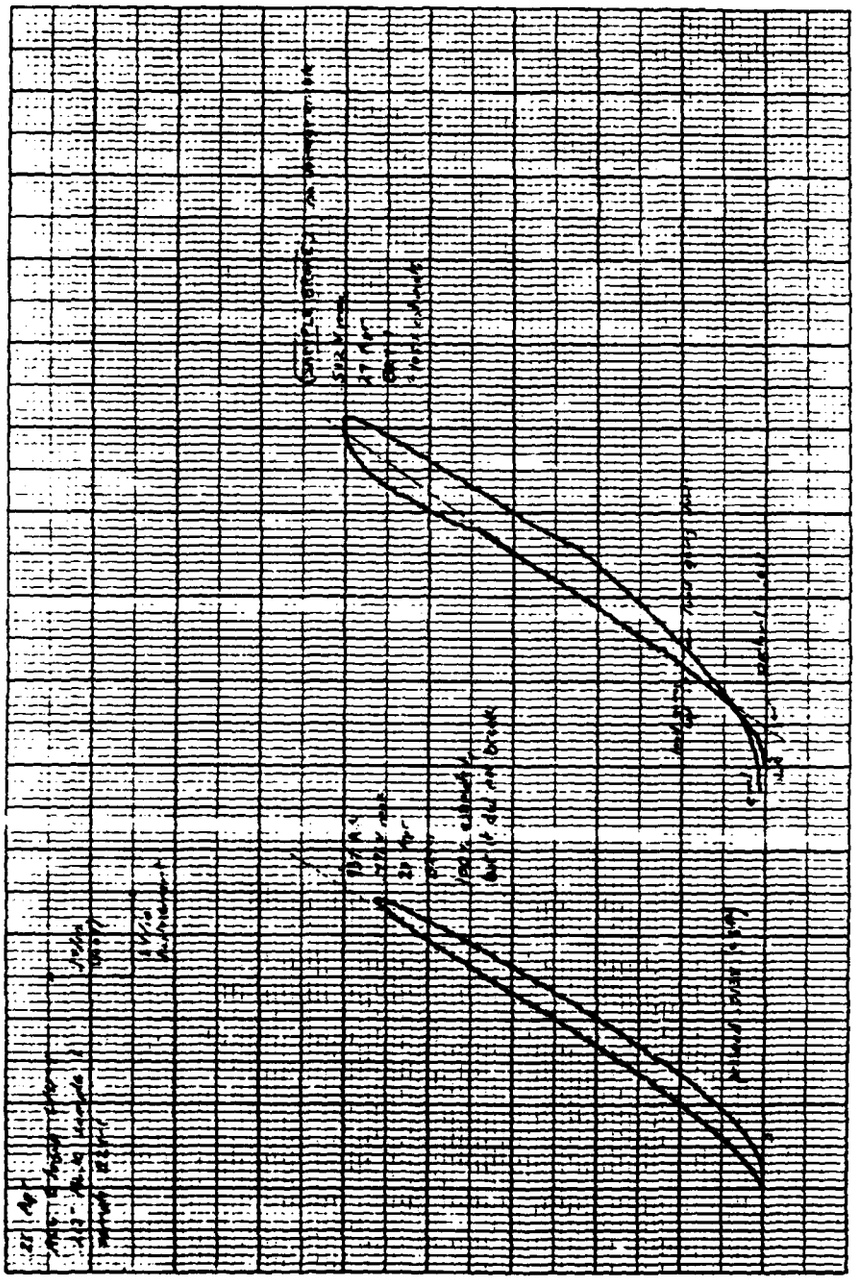

Figure 80. Specimen B24-1, Page 2 of 2

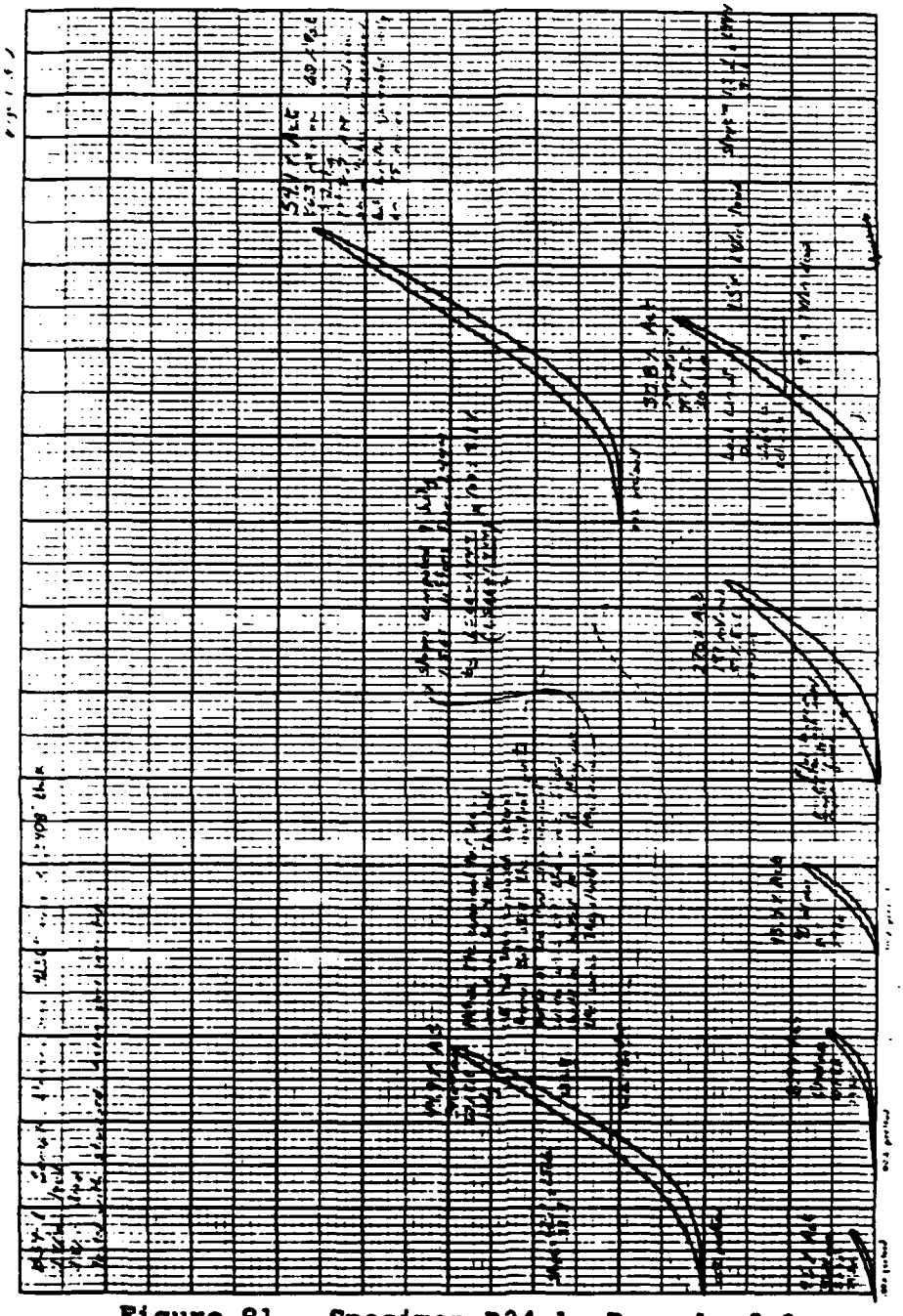

Figure 81. Specimen B34-1, Page 1 of 2

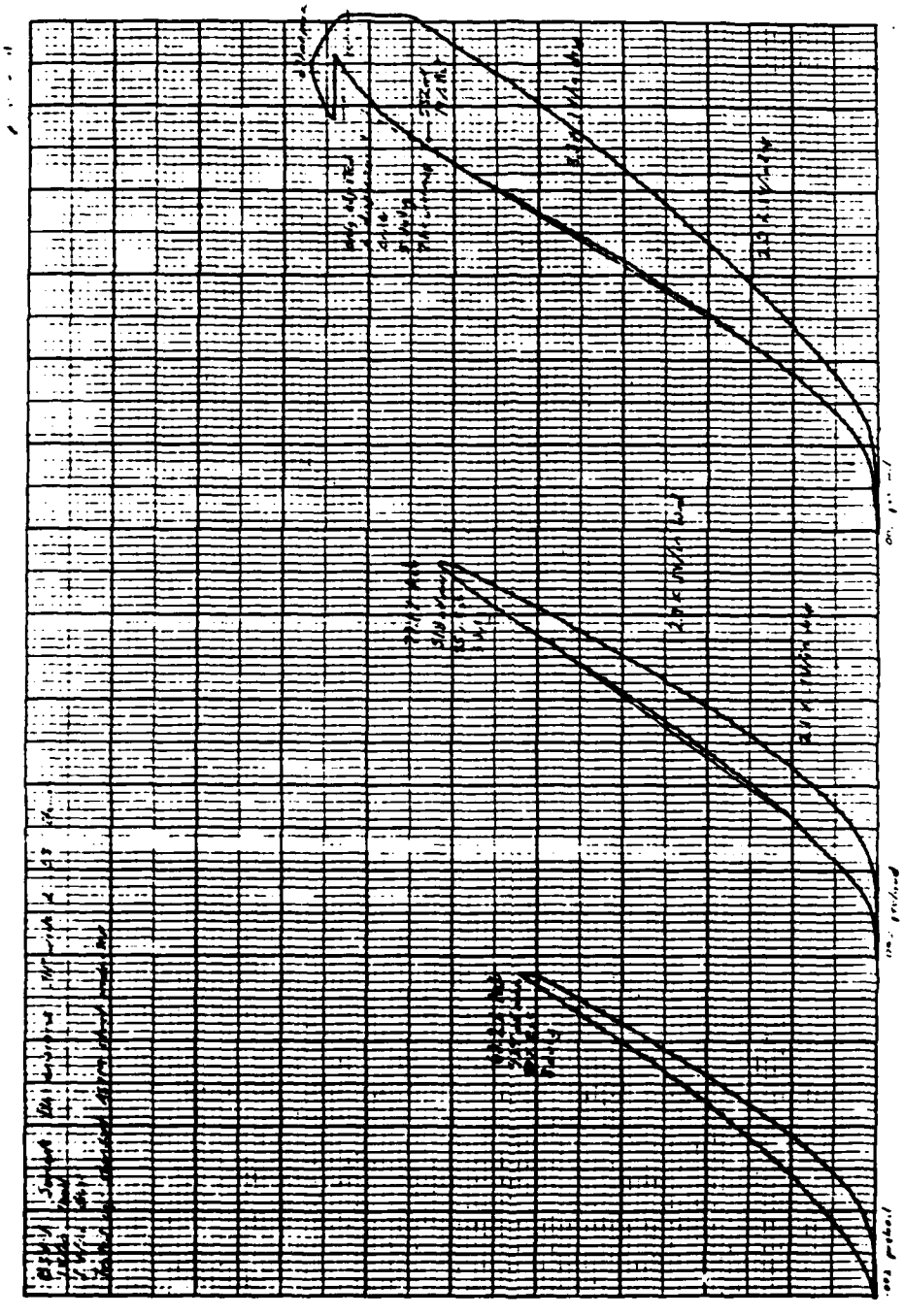

Figure B2. Specimen B34-1, Page 2 of 2

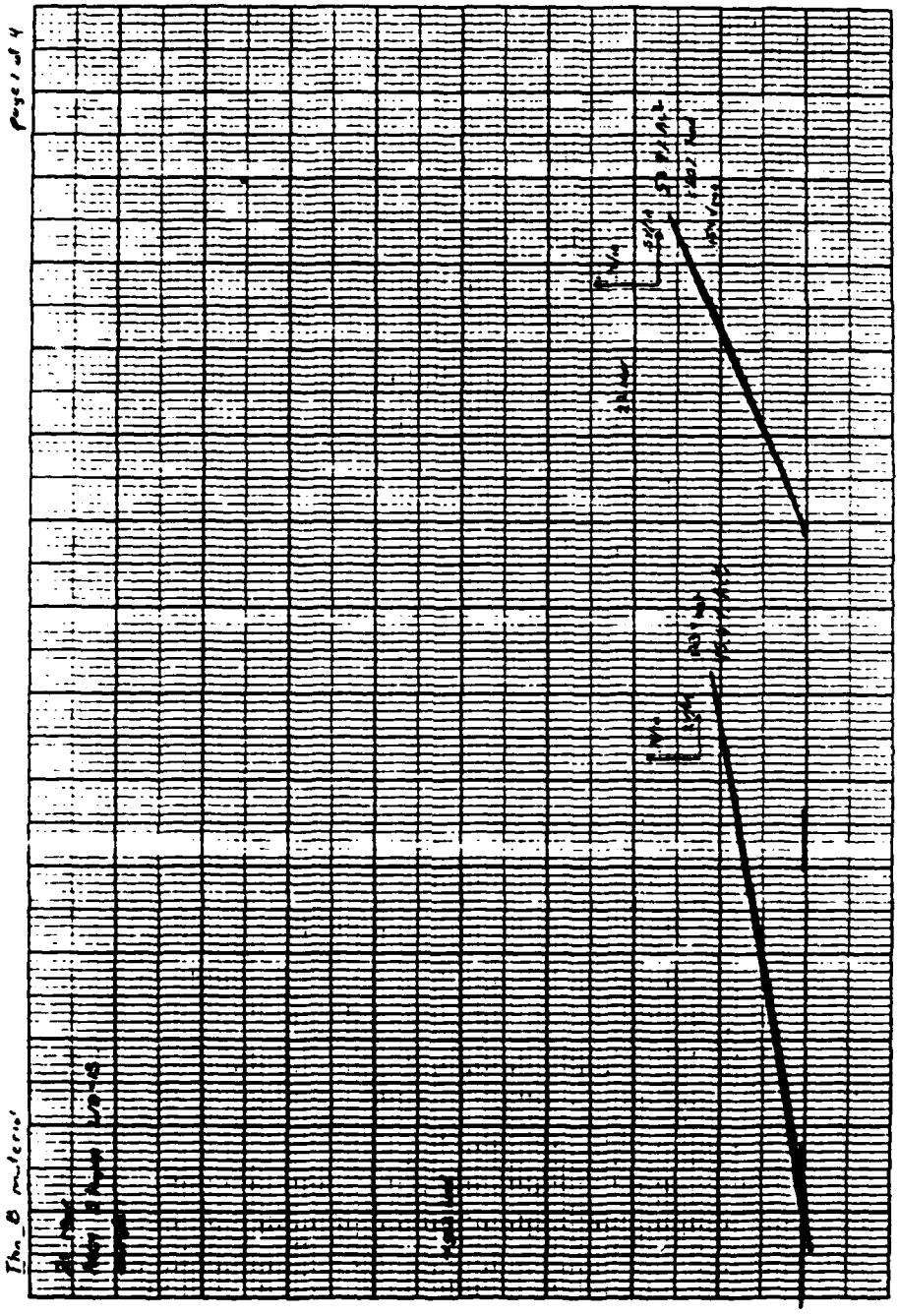

Figure 83. Specimen B215-1, Page 1 of 4

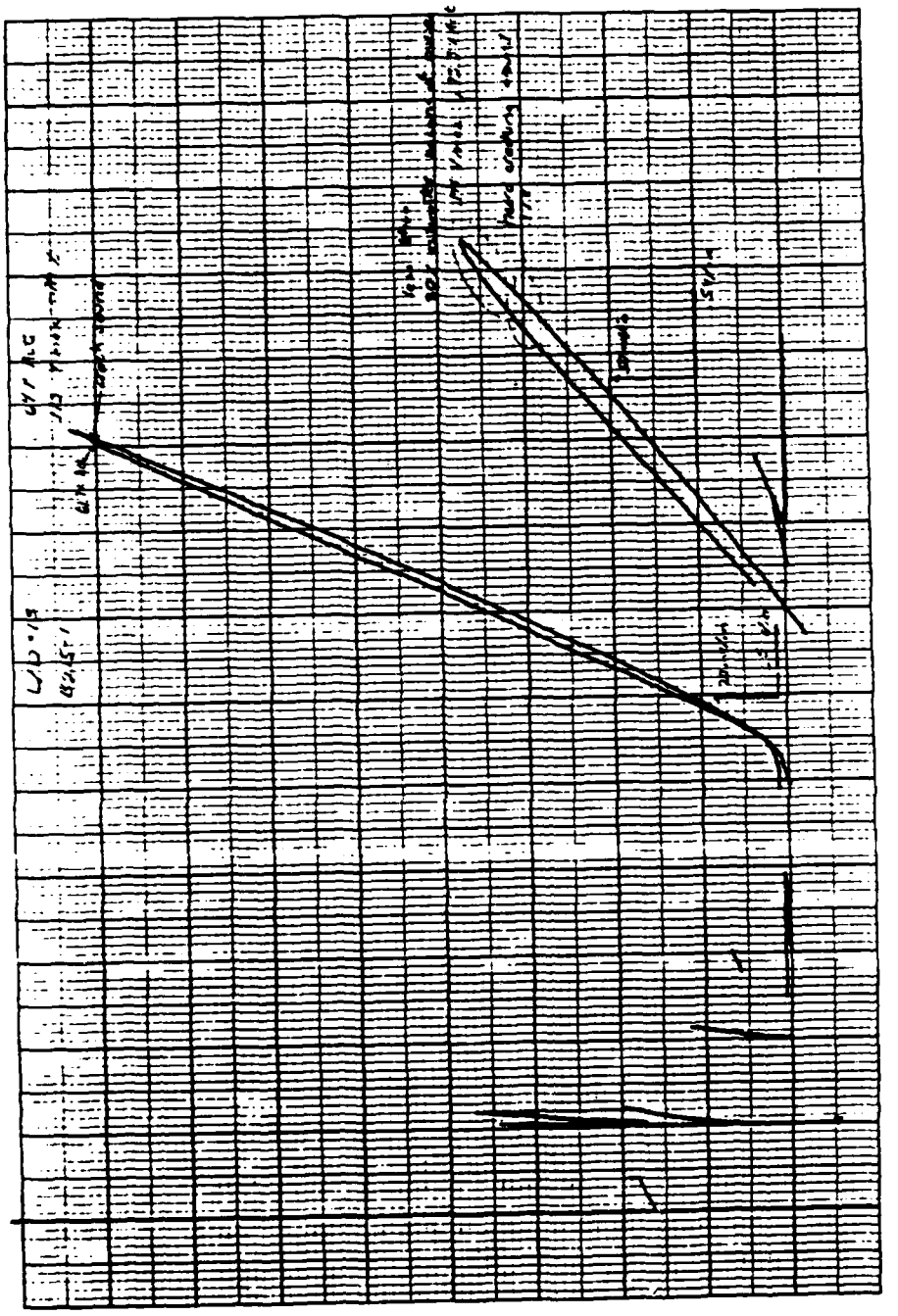

Figure 84. Specimen B215-1, Page 2 of 4

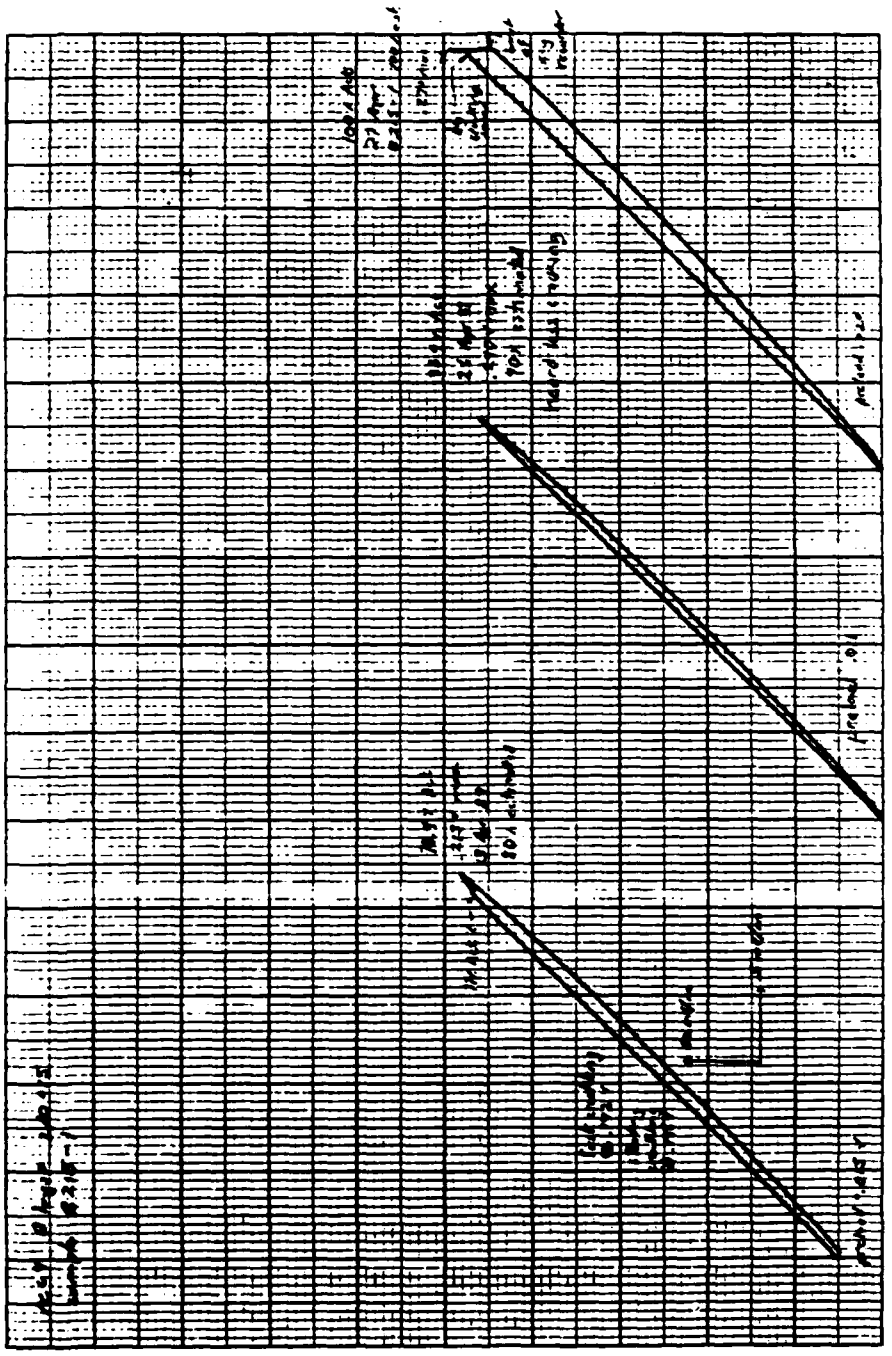

Figure 85. Specimen B215-1, Page 3 of 4

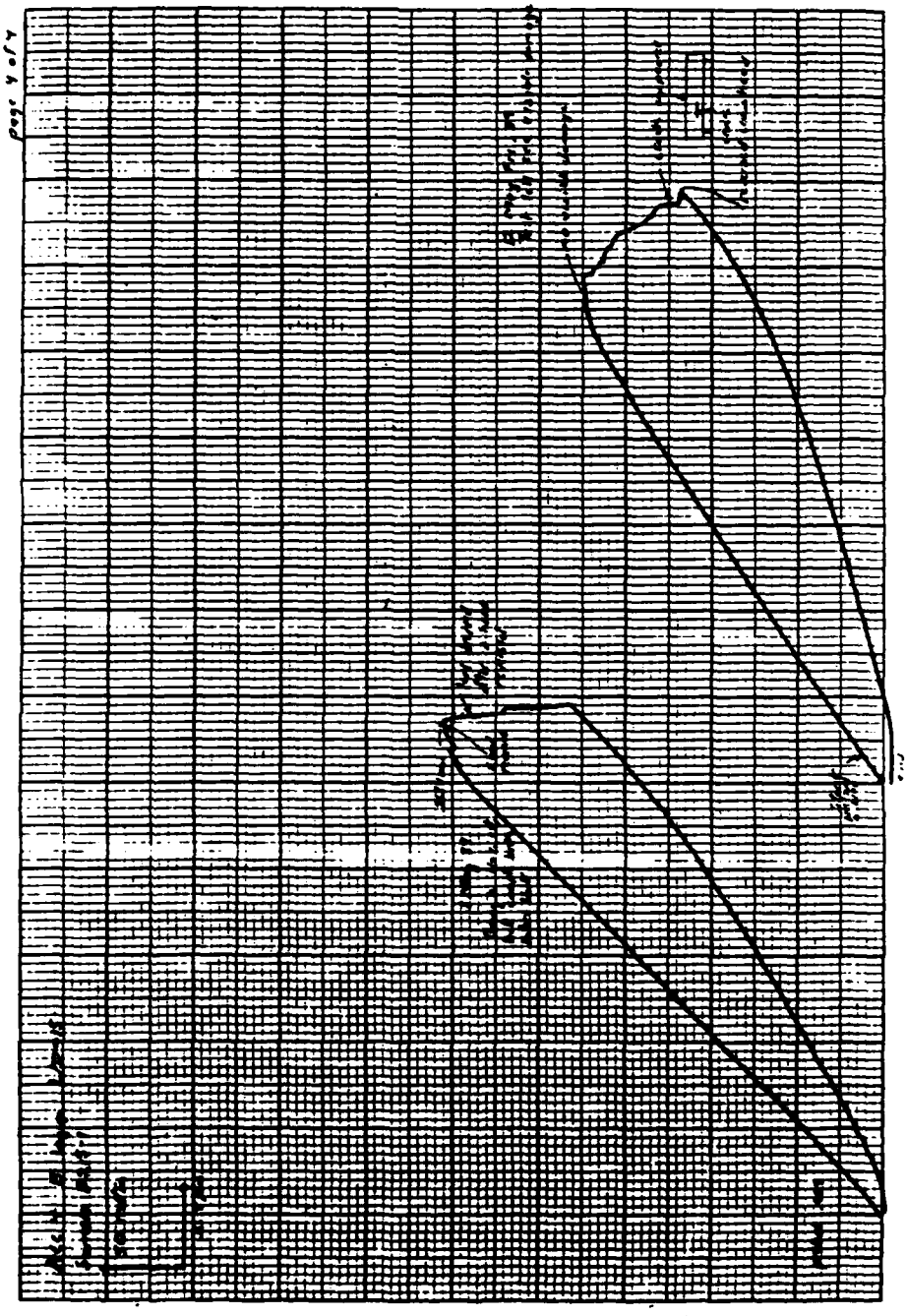

Figure 86. Specimen B215-1, Page 4 of 4

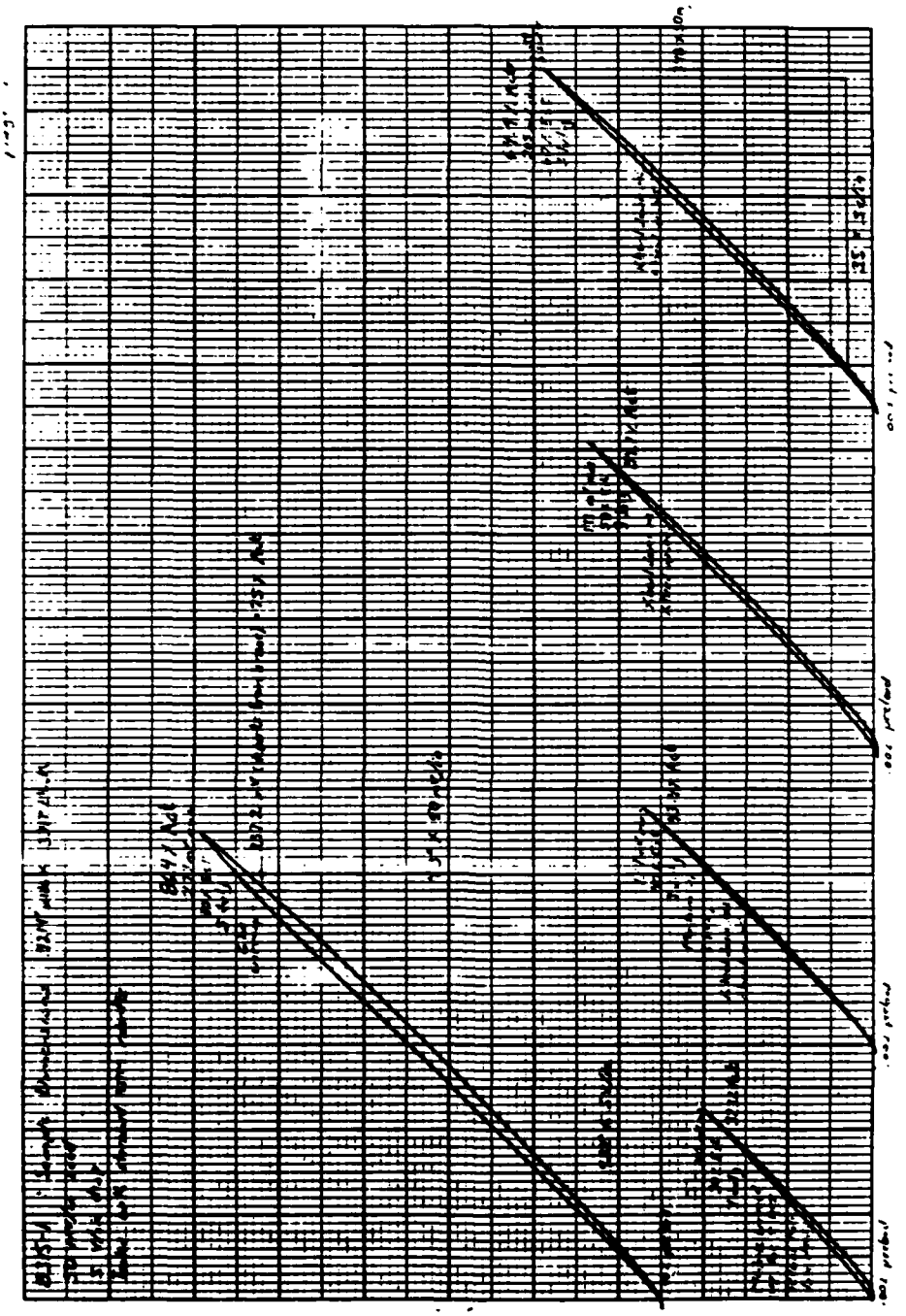

Figure 87. Specimen B315-1, Page 1 of 3

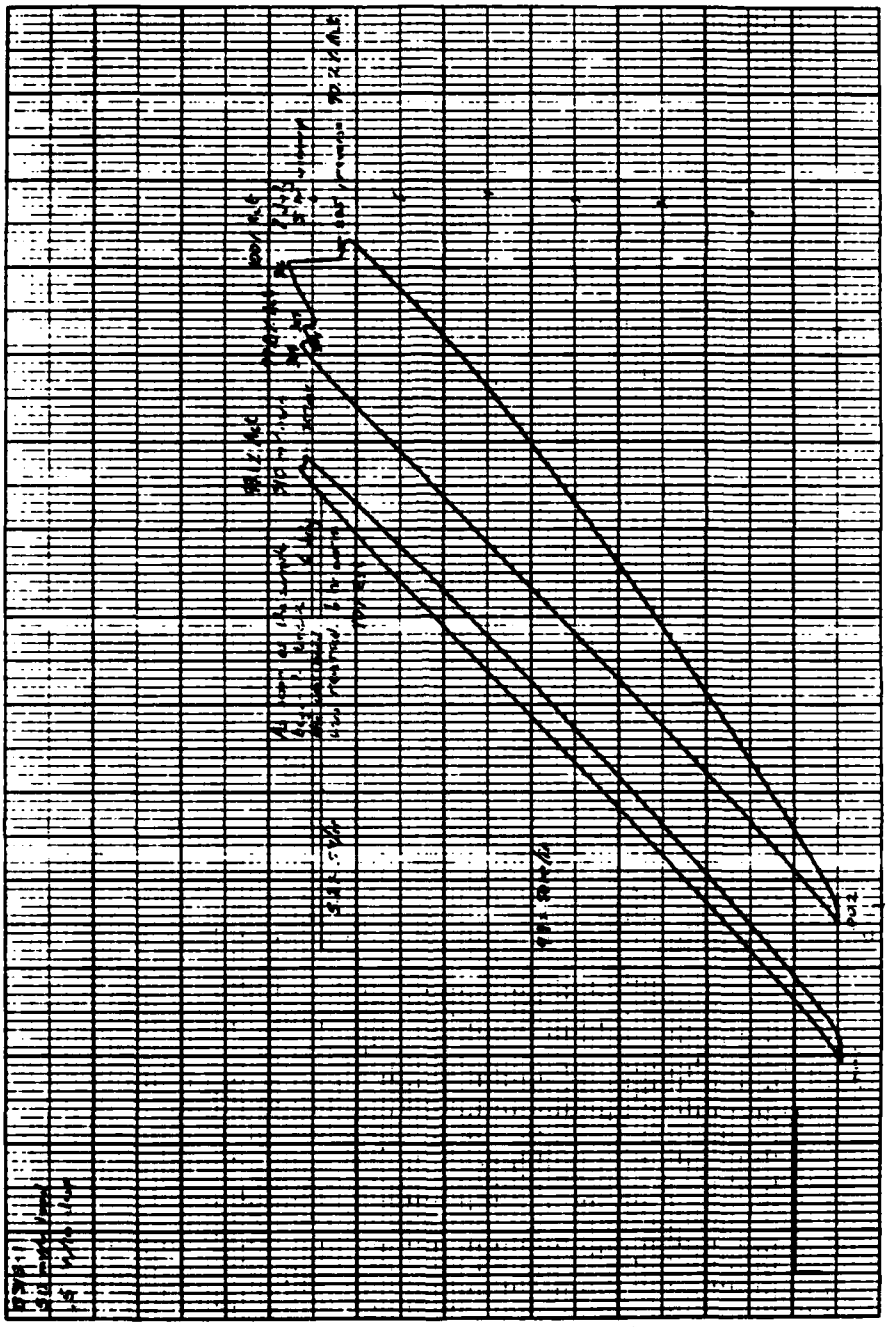

Figure 88. Specimen B315-1, Page 2 of 3

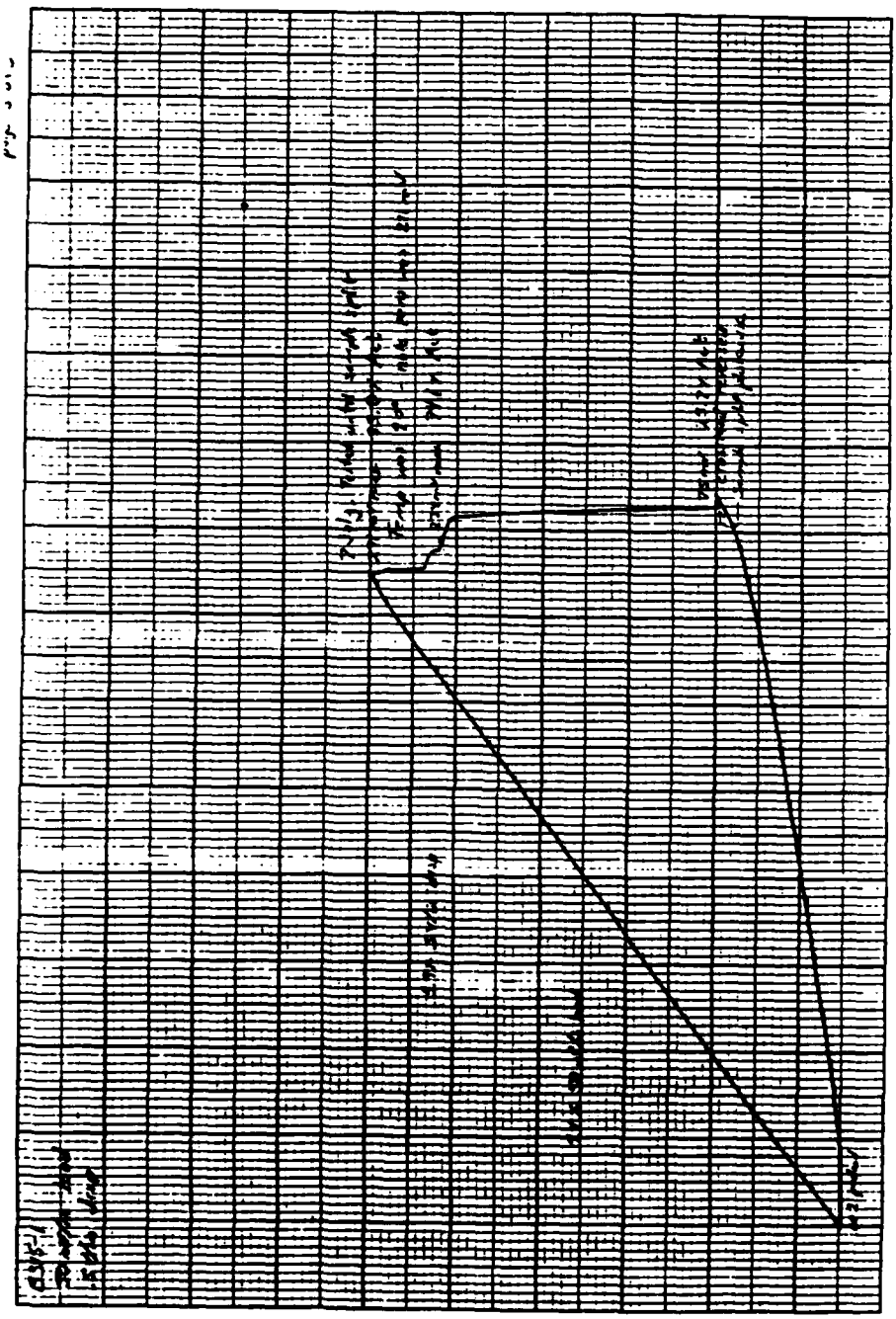

Figure 89. Specimen B315-1, Page 3 of 3

Vita

Captain Andrew Kenny was raised in Grove City in rural Western Pennsylvania where he graduated from high school in 1980. He attended Michigan Technological University from which he received the degree of Bachelor of Science in Metallurgical Engineering in May, 1984. Upon graduation he received a commission in the USAF through the ROTC program. He was employed as a research assistant at the Argonne National Laboratory, Chicago, Illinois, until called to active duty in August, 1984. His first assignment was as a Materials and Processes Engineer in the Metallurgical and NDI Laboratory in the Directorate of Maintenance at Ogden ALC, Utah. He was transferred to Wright-Patterson AFB and entered the School of Engineering, Air Force Institute of Technology, in June, 1988.

Permanent Address: 501 Woodland Ave.
Grove City, PA 16127

UNCLASSIFIED
SECURITY CLASSIFICATION OF THIS PAGE

REPORT DOCUMENTATION PAGE

Form Approved OMB No. 0704-0188

1a. REPORT SECURITY CLASSIFICATION UNCLASSIFIED	1b. RESTRICTIVE MARKINGS
2a. SECURITY CLASSIFICATION AUTHORITY	3. DISTRIBUTION/AVAILABILITY OF REPORT Approved for public release; Distribution Unlimited
2b. DECLASSIFICATION/DOWNGRADING SCHEDULE	
4. PERFORMING ORGANIZATION REPORT NUMBER(S) AFIT/GAE/ENY/89D-18	5. MONITORING ORGANIZATION REPORT NUMBER(S)
6a. NAME OF PERFORMING ORGANIZATION School of Engineering 6b. OFFICE SYMBOL (If applicable) AFIT/ENY	7a. NAME OF MONITORING ORGANIZATION Aero Propulsion Laboratory Wright Research and Development Center
6c. ADDRESS (City, State, and ZIP Code) Air Force Institute of Technology (AU) Wright-Patterson AFB, OH 45433-6583	7b. ADDRESS (City, State, and ZIP Code) WRDC/POTC Wright-Patterson AFB, OH 45433-6563
8a. NAME OF FUNDING/SPONSORING ORGANIZATION WRDC Aero Propulsion Lab 8b. OFFICE SYMBOL (If applicable) WRDC/POTC	9. PROCUREMENT INSTRUMENT IDENTIFICATION NUMBER Advice No. 88H5174
8c. ADDRESS (City, State, and ZIP Code) WRDC POTC Wright-Patterson AFB, OH 45433-6583	10. SOURCE OF FUNDING NUMBERS PROGRAM ELEMENT NO. 62203F; PROJECT NO. 3066; TASK NO 12; WORK UNIT ACCESSION NO. 28
11. TITLE (Include Security Classification) Damage Mechanisms and Indenter Size Effects in Cross Plied Carbon-Carbon Composites(Unclassified)	
12. PERSONAL AUTHOR(S) Andrew Kenny, Captain, USAF	
13a. TYPE OF REPORT MS Thesis 13b. TIME COVERED FROM _____ TO _____ 14. DATE OF REPORT (Year, Month, Day) 1989, December 15. PAGE COUNT 149	
16. SUPPLEMENTARY NOTATION	
17. COSATI CODES FIELD: 11; GROUP: 04; SUB-GROUP: 18. SUBJECT TERMS (Continue on reverse if necessary and identify by block number) Carbon-Carbon Composites, Materials (Composite Materials), Failure (Mechanics), Mechanical Properties (Flexural Properties)	

19. ABSTRACT (Continue on reverse if necessary and identify by block number)

Thesis Advisor: Paul D. Copp, Major, USAF
Associate Professor of Aeronautical Engineering
Department of Aeronautical Engineering

20. DISTRIBUTION/AVAILABILITY OF ABSTRACT ☒ UNCLASSIFIED/UNLIMITED ☐ SAME AS RPT. ☐ DTIC USERS	21. ABSTRACT SECURITY CLASSIFICATION Unclassified
22a. NAME OF RESPONSIBLE INDIVIDUAL Paul D. Copp, Major, USAF	22b. TELEPHONE (Include Area Code) 513-255-2362 22c. OFFICE SYMBOL AFIT/ENY

DD Form 1473, JUN 86 Previous editions are obsolete. SECURITY CLASSIFICATION OF THIS PAGE

UNCLASSIFIED

UNCLASSIFIED

19. The microscopic damage mechanisms which cause failure in 2-D carbon-carbon composite beams tested in three point bend were studied, and the effect of the beam thickness and cross plies in the laminate were examined. Local failure modes caused by loading were catagorized. A linear two-dimensional finite element method was used to model beams of two thicknesses. Failure contours computed with Dendis' Tsai-Wu post processor were in good agreement with the experimentally determined microscopic shear crack initiation sites and load levels in the matrix. The loading indenter's diameter and rigidity were found to be effective in controlling certain types of localized cracking.

UNCLASSIFIED